Crystallization and Microcharacterization of

Yttrium Aluminosilicate Glass-Ceramics

Dissertation

zur Erlangung des akademischen Grades doctor rerum naturalium

(Dr. rer. nat.)

vorgelegt dem Rat der Chemisch-Geowissenschaftlichen Fakultät der

Friedrich-Schiller-Universität Jena

von M.Sc. Ashkan Keshavarzi

geboren am 22.09.1976 in Shiraz, Iran

Gutachter:
1. Prof. Dr. Dr. Christian Rüssel
2. Prof. Dr. Delia S. Brauer

(Otto-Schott-Institut, FSU Jena)
Tag der öffentlichen Verteidigung: 23. September 2014

Zusammenfassung

In dieser Arbeit wurden alkalihaltige und alkalifreie Gläser im System $Y_2O_3/Al_2O_3/SiO_2/AlF_3/CeF_3$ untersucht. Die Analyse diese Gläser erfolgte hinsichtlich der Kristallisationseigenschaften, der ausgebildeten Mikrostrukturen, sowie der Fluoreszenzeigenschaften und des Einflusses von Keimbildner wie ZrO_2 und TiO_2. In den alkalifreien Proben ist die durch eine Wärmebehandlung bei $\geq$ 1300°C, hauptsächlich ausgebildete Phase Yttriumaluminiumgranat (YAG). Die Fluoreszenzspektren zeigen ein Maximum bei 532 nm. Da nur die YAG Kristalle zur Emission beitragen, beweist dies, dass die Ce^{3+} Ionen in den Kristall eingebaut werden. Bedingt durch die sehr viel höhere thermische Leitfähigkeit und chemische Beständigkeit im Vergleich zu kommerziellen Lichtkonvertern bestehend aus YAG-Leuchtstoffen eingebettet in Polysiloxane, sollte die hergestellt Glaskeramik für Hochleitungslichtkonverter geeignet sein. In einem zweiten Versuch enthielt die hergestellte Glaszusammensetzung zusätzlich noch entweder Alkalien oder CaO. Aus diesen Gläsern konnte die YAG Phase schon bei Temperaturen von 1000°C (oder niedriger wenn für 20 h getempert) erhalten werden. Lumineszenzspektren, welche von diesen Gläsern aufgenommen wurden, zeigen eine maximale Effizienz vergleichbar zu denen kommerzieller weißer LEDs. Weiterhin konnte durch Alkalien als Netzwerkwandler (Na_2O) und Fluoridionen die Konnektivität des Si-O-Si Netzwerkes gesenkt werden. Dies wurde Anhand des Glassystems $Y_2O_3/Al_2O_3/SiO_2/AlF_3/Na_2O/CeF_3/B_2O_3$ veranschaulicht. In diesem Glas konnte YAG bei 1000°C bereits nach 3h auskristallisiert werden. Die benötigte Temperatur und Zeit der YAG Kristallisation konnte folglich von 1400°C für 20h auf 1000°C und 3h reduziert werden. Die Kristallisationsmechanismen von Oberflächenkristallisation und Volumenkristallisation wurden durch Röntgenbeugung, optischer sowie Elektronenmikroskopie und Fluoreszenzspektroskopie aufgeklärt werden. Die Anwendung rasterelektronenmikroskopischer Techniken wie Kikuchi-Beugung transmittierter Elektronen und EBSD ermöglichten die Identifizierung der auftretenden Kristallphasen.

Abstract

In the present work, alkaline and alkali free glasses in the system Y_2O_3/Al_2O_3/SiO_2/AlF_3/CeF_3 with were investigated. Their crystallization behavior, the formed microstructure and the fluorescence properties of these glasses as well as the effect of the nucleating agents ZrO_2 and TiO_2 were studied. In alkali free samples, the main formed phase after annealing at temperatures ≥1300 ∘C was YAG. The fluorescence spectra show a maximum at 532 nm. Only the YAG crystals contribute to the light emission which proves that Ce^{3+} is incorporated into the YAG crystals. Due to their much higher thermal conductivity and chemical durability, in comparison to commercial light converters composed of YAG phosphors embedded in polysiloxane, the prepared glass–ceramics should be suitable for high power light converters. In the second attempt, the glass compositions containing either alkalis or CaO were prepared. From these glasses, the YAG phase could already be precipitated at a temperature of 1000 °C and lower if crystallized for 20 h. Luminescence spectra recorded from these glasses showed a maximum efficiency approximately as high as that of commercial white LEDs. Furthermore, a mixture of the alkaline modifier (Na_2O) and fluorine could reduce the connectivity of the Si-O-Si in the network of the glass matrix. This was illustrated with a glass composition in the system Y_2O_3/Al_2O_3/SiO_2/AlF_3/Na_2O/CeF_3/B_2O_3. In this glass, YAG could be crystallized at 1000 °C within 3 h. Hence, it enabled to reduce the temperature and time of YAG crystallization from 1400 °C and 20 h to 1000 °C and 3 h. The crystallization kinetics as well as the mechanism of surface and bulk crystallization was clarified using X-ray diffraction, optical and electron microscopy as well as fluorescence spectroscopy. The application of techniques in the scanning electron microscope (SEM) using Kikuchi diffraction of transmitted electrons, electron backscattered diffraction enabled to identity occurring crystal phases.

Table of Contents

1. Introduction

Yttrium aluminum garnet (YAG, $Y_3Al_5O_{12}$) based materials are used for many different applications such as in cathode-ray tube (CRTs), field emission displays (FED), scintillation, phosphorus and electroluminescent applications as well [1-3]. For application in a solid-state laser or in the other optical devices the transition metals and/or the rare earth (lanthanide) and/or actinide ions (e.g. Ce^{3+}, Nd^{3+}, Dy^{2+}, Ho^{3+}, Tm^{3+}, etc.) are added into YAG ceramics in order to produce the fluorescent transition of interest [4], [5]. For example Nd-doped YAG laser was first demonstrated by Geusic *et al* at Bell Laboratories in 1964 is one of the most important materials wieldy used for welding and cutting applications or Nd:Cr: YAG that suggested for solar pump laser in the solar power satellite [6], [7]. Laser properties of YAG are associated with the materials characteristics of rare earth aluminates, which favor applications as composite laser hosts, and glass fibers that are important for optical applications, but also can be used in composite materials. In recent years, the Ce:YAG is used as a phosphor for a white light emitting diodes (LED) [8]. Phosphor of Ce^{3+}:YAG first mentioned in 1967 as a cathodoluminescent phosphor, although in the same paper its photoluminescent properties are described [1].

Yttrium aluminum garnet is cubic with the space group O_h^{10} (*Ia3d*) and lattice constants $a=b=c \approx 12$ Å. The garnet structure contains eight formula units per unit cell. The garnet phase possesses 160 atoms per unit cell. The crystal can be described by the formula $C_3A_2D_3O_{12}$ where the Y ions sit in dodecahedral (C sites) and the Al ions occupy both tetrahedral (D sites) and the trigonal distorted octahedral (A sites). The YAG lattice is relatively stable and has high thermal conductivity (11.2 W $m^{-1}K^{-1}$) which makes it desirable as a host lattice for a number of phosphor systems. The garnet phase (YAG composition) has a complicated crystal structure (Figure 1). There are two types of aluminum ions in YAG: one coordinated by four oxygen atoms (Al^{4+}) and one coordinated by six oxygen atoms (Al^{6+}). There is a unique yttrium site in YAG (YO_8) and a single distinctive oxygen environment (OY_2Al_2) [9].
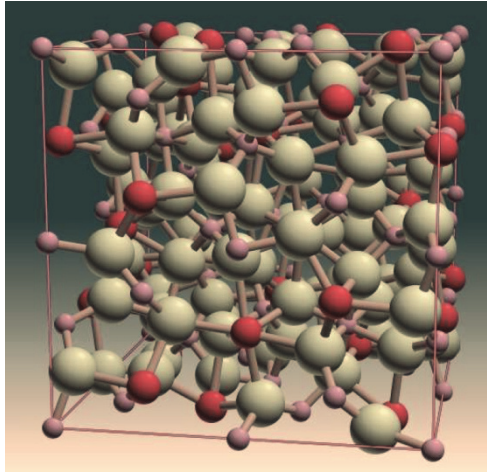
Figure 1. Structure of YAG unit cell, Ref.[55].

The application of this phosphor and many others of fluorescent lighting are widely described in the recent literatures. The YAG: Ce^{3+} phosphor is widely applied as a color converter, using blue LED excitation and re-emitting yellow light, which when combined with blue light from the LED gives a acceptable white light. White light emission can be obtained by mixing the blue light of the LEDs and the yellow light generated by fluorescence emission of YAG doped Ce^{3+}. In the YAG lattice, Ce^{3+} is incorporated at the yttrium sites. In the excitation-emission spectrum of Ce^{3+}: YAG, a peak at 460 nm is observed which is typically related to the blue excitation by LEDs. In Figure 2 the photoluminescence spectra of Ce^{3+}: YAG is presented. Where a broad emission band with a peak at around 550nm is observed as a result of exciting with a wavelength at 460 nm. Similarly, two excitation bands with peaks at about 338 and 460 nm are observed upon Ce^{3+} emission at 540 nm.

Luminescence emission of the Ce^{3+} is dependent of the 5d → 4f electronic transition which is strongly correlated in the YAG lattice structure. Changes in the optical properties of the Ce^{3+} is caused only by transferring an electron which is located at the 4f state and the 5d orbital. The next higher energy level of the trivalent cerium is 5d (free electron orbital). In order to understand this level of the energy, it should be mentioned that Ce^{3+} is coordinated with eight oxygen atoms in the D_2 symmetry site of yttrium in (see page 1, garnet structure $C_3A_2D_3O_{12}$). Due to the spin-orbit interaction cerium trivalent has two ground state of $^2F_{5/2}$ and $^2F_{7/2}$. In figure 3 the emission spectra show two transition 5d → $^2F_{5/2}$ and later to the 5d → $^2F_{7/2}$. Both asymmetric and position of this band are varies and depended on concentration of Ce^{3+} substitution on sites of yttriums, hence the center of the broad peak is around 550 nm. Meanwile, electron excited from 4f to 5d configured as a ^2D that is split to $^2D_{3/2}$ and $^2D_{5/2}$ that

is known as higher states of energy levels. When electrons in $^2D_{5/2}$ are on the higher energy level are unstable, and would relax and subsequently transfer to $^2D_{3/2}$ state with electron–phonon interaction. Hence, we have the emission band is attrebuted to the $^2D_{3/2} \rightarrow ^2F_{7/2}$ or the $^2D_{3/2} \rightarrow ^2F_{5/2}$ transition, respectively.
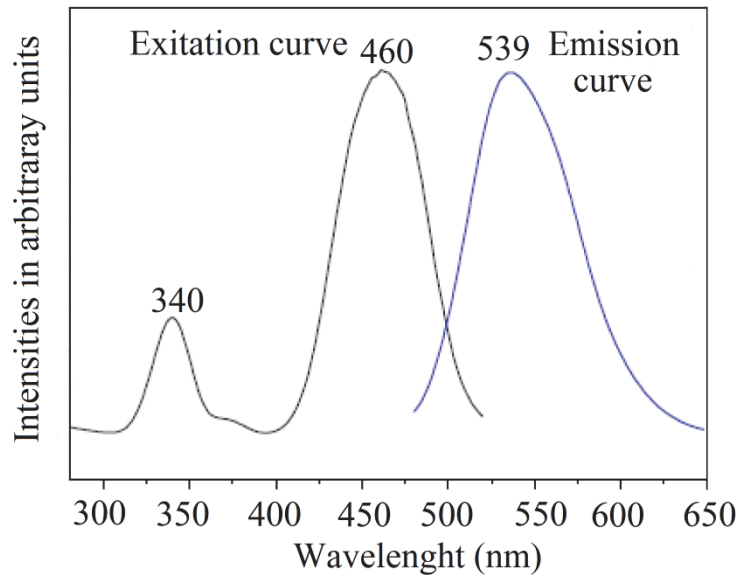
Figure 2. Excitation and emission spectra of the Ce^{3+}: YAG, Ref.[10].
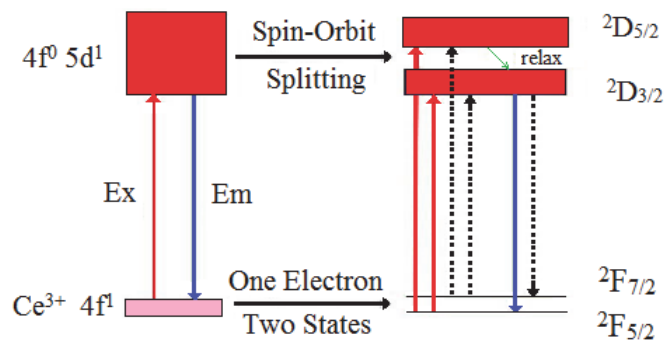

Figure 3. Excitation-emission and energy level diagram of Ce^{3+}: YAG, Ref.[10].

2. Technological limitation of LEDs

High power LEDs is a key component today because of they provides a sufficiently long life time and only less energy than required for traditional lighting technology. In order to widespread applications of LED lighting and for further commerciallization, some

requirements are still to be fulfilled. Presently, LEDs are still optimized with respect to their efficiency and life time. Otherwise, for high power LEDs, heat removal is still a serious problem which limits the maximum light intensity of LED devices. Higher light intensities are usually achieved by bigger chips and higher current, however, high power LEDs convert only 15% of the electrical power into light and hence, the remaining energy is transferred into heat. This heat generated by the LED should be managed and effectively be remove from the LEDs chip in order to avoid critical damage in electronic junction and the encapsolated light converter. Hence, heat managment became a crucial subject for packaging of LEDs chip in order to minimizing of thermal stress and made safe junction temperature operation. These desired behavior is the main reason why high power LEDs have comparably short lifetimes.

For a light converter, materials such as polysiloxane polymers and epoxy resin are used as matrix in which the phosphores are dispersed. Since the thermal conductivity of organic polymers is fairly poor, degradation occurs and increases with the energy density and operating time. This can only be overcome by using converter materials with higher thermal conductivity, eventually combined with a complete redesign of the LED chip. The converter required might be composed by transparent or translucent ceramics or glass-ceramics that contains components acting as phosphors. Higher thermal conductivity of the converter material might also result in higher output efficiency. The long term stability of such systems might be increased by such ceramics or glass-ceramics materials.

Generally, single crystalline YAG can be formed by conventional crystal growth techniques. Single crystal YAG preparation using crystal growth technique is, however, expensive and requires very sophisticated equipment, and it is technically difficult to produce the desired shape, size and optical quality.

YAG containing glass-ceramics are considered as another suitable choice for converting light of high power LEDs also for outdoor applications because of the good thermal and UV resistance. These glass-ceramics need not to be protected for example by further encapsulation. The aim of this thesis is to improve the understanding of the phase formation during heat-treatment of the yttrium aluminosilicate glasses. For this purpose, the phase formed during heat-treatment have to be characterized. In a further step, the formation of the YAG crystals has to be optimized. In order to achieve small crystals, temperature necessary for the formation of YAG crystals has to be minimized. For optical applications, where superior optical properties are required, the fabrication process of YAG glass-ceramics must

be controlled and for this purpose the desirable microstructures (single phase YAG) can be achieved. Up to now, YAG ceramics for optical applications have been processed either with stoichiometric YAG powders or by reactive sintering a process which starts with a mixture of Y_2O_3, Al_2O_3 and CeO_2 powders in rotary mill and finally mixed batch sintered up to 1850 °C. The preparation of rare-earth glass-ceramics has some challenges due to the temperature of melting and the, high value of T_g. Due to the necessary addition of a network former, it is often difficult to perform the crystallization in such a manner, desired crystalline phase is formed. Furthermore the transparency or translucency, moisture resistance and also the quantum efficiency of output light of such glass-ceramics are other important points to be mentioned [14].

3. Yttrium aluminosilicate glass

Over the past 20 years yttria-alumina-silica glass systems have motivated numerous investigations due to their potential through forming glass-ceramic materials. The system $Y_2O_3–Al_2O_3–SiO_2$ is of importance as a system involving the most widely used additives for technical use due to their extraordinary physico-chemical and mechanical properties. A series of overview on available data of the $Y_2O_3–Al_2O_3–SiO_2$ systems are given by numerous authors . The first major study of the $Y_2O_3-Al_2O_3-SiO_2$ system was reported by Bondar and Galakov who developed a phase diagram in 1964 [15]. Several investigations have been carried out also on other properties of yttria-alumina-silica glasses [15-23]. However, most of the studies were focused on oxynitride (Y–Si–Al–O–N) glass compositions and the effect of starting composition and crystallization temperature on the microstructure of such glass-ceramics were examined and detailed analytically by electron microscopy in order to determine the chemical compositions of the crystals phases and the residual glassy phase. Incorporation of nitrogen into oxide glasses increases their softening temperature, their glass transition temperature, their viscosity, their hardness and allows to obtained glass-ceramic suitable for applications at higher temperatures. Crystallization of such nitrogen glasses occurs at higher than in the corresponding oxide glasses. The preparation of such glasses is carried out by conventional melting and cooling procedures using different type of electric furnace with various heating elements and crucible materials. However, some melting processes were also performed by laser irradiation. Many experimental studies were performed in order to with the aim to optimize the mechanical properties of yttria doped SiAlON (silicon aluminum oxynitride). Here, oxynitride glasses are used as a model for the

amorphous grain-boundary phase composition in Y-SiAlON materials in which nitrogen is substitutes for oxygen in the Y_2O_3–Al_2O_3–SiO_2 system to produce a more tightly linked glass network achieved by a considering to increase a higher coordination number of nitrogen. It has been shown that the glassy phase in β-sialon material, with additions of Y_2O_3, can be crystallized to YAG using a thermal treatment at temperatures higher than 1100 °C. The crystallization behavior of such oxynitride glasses has been investigated by several research groups. Leng-Ward *et al* studied glasses having compositions with a constant Y: Si: Al ratio of 1.04 : 1.27 : 1.27 ($45Y_2O_3$ /25 Al_2O_3 /30 SiO_2 (wt%) and nitrogen concentrations ranging from 0 to 30 eq.% that means 30 % of the oxygen of oxide glasses is replaced by nitrogen) [24]. They reported on the thermal treatment of such glass composition at 1250°C for 40 h. This results in an increased in nitrogen concentration which is a result of crystallization of yttrium aluminum garnet crystallization instead of yttrium disilicate ($Y_2Si_2O_7$); the nitrogen is then mainly incorporated into Si_2N_2O. Thermal treatment of the nitrogen containing glasses at 1100°C produced partially crystallization involving an intermediate phase related to nitrogen-wollastonite ($Y_2Si_2O_4N_2$). Loehman investigated glasses in the systems Y_2O_3-SiO_2-AlN and Y-Si-Al-O-N system. Thermal treatment of these glasses at temperatures of 1000, 1100, 1200 and 1250 °C for longer times resulted in the formation of $Y_2Si_2O_7$ as the predominant crystalline phase [20, 21]. Five intermediate phases such as two modification of yttrium silicates, yttrium aluminum silicates, nitrogen apatite and $Y_4Si_4O_{11}N_2$ were also observed as a results of thermal treatment of these compositions. O'Meara *et al* prepared a series of glasses with different additions of Si_3N_4 in the concentration range from 8 to 15 wt% (initial composition in wt%: 53 Y_2O_3, 17 Al_2O_3, 30 SiO_2)[25, 26] . These glasses were crystallized by thermal treatment at 1250°C and different periods of the time. In glass-ceramics with yttria concentrations between 52-67.5 wt% , the main phases were Y_2O_3, $Y_2Si_2O_7$ and $Y_3Al_5O_{12}$, while in glass-ceramics with yttria concentrations between 7 and 45 wt% the main phases were $Y_2Si_2O_7$, SiO_2, Al_2O_3 and $Al_6Si_2O_{13}$. Arita *et al* studied a series of glass-ceramics containing yttria with concentrations between 33 and 44 wt% and more than 30 wt % silica [27]. They also gave a review on crystallization mechanisms in yttria-alumina-silica glasses. The prepared glass samples were crystallized at 1250 °C for different periods of the time. They observed different polymorphs phases of $Y_2Si_2O_7$ polymorphs and did not obtain any hint of the occurrence of the YAG phase. They concluded that crystallization of YAG in high silica concentrations is much more difficult in comparison to the crystallization of the other components. Chadwick and Wilkinson performed a comprehensive study on the crystallization of glasses with the compositions $43Y_2O_3$ /21Al_2O_3 /36 SiO_2 and 27 Y_2O_3 /24

Al$_2$O$_3$ /49 SiO$_2$. They observed only Y$_2$Si$_2$O$_7$ and Al$_6$Si$_2$O$_{13}$ as crystalline phases after thermal treatment at 1200 and 1250 °C [28]. In their studies, YAG crystallized, however, in samples with SiO$_2$ concentrations smaller than 5 wt% and an yttria/alumina ratio of around 3±0.5 wt%. Dinger *et al* also studied the crystallization of a glass with the composition Y$_{0.26}$Si$_{0.30}$Al$_{0.11}$ON$_{0.11}$. They concluded a heterogeneous nucleation mechanism, caused by inter-metallic iron silicides, acting as nucleating agents which resulted in the crystallization of dendritic y-Y$_2$Si$_2$O$_7$ crystals [29]. After secondary crystallization of YSi$_2$AlO$_4$N$_2$ in dendritic regions at 1200°C, the high-temperature polymorph of Y$_2$Si$_2$O$_7$, (δ-Y$_2$Si$_2$O$_7$) formed and became the predominant crystalline phase in glass-ceramics if the sample was crystallized at 1300 or 1400 °C. Besson *et al* studied a glass with a composition similar to that of Dinger [30]. In a glass containing 17 wt% nitrogen, α-Y$_2$Si$_2$O$_7$ is formed below 1200°C and β-Y$_2$Si$_2$O$_7$ is formed above this temperature. Besides, crystallization of the YAG phase occurred at 1100 °C and phases of AlYO$_3$ and Si$_2$N$_2$O were additionally obtained during crystallization at 1250 or 1300 °C. A review given by Arita *et al* compared and showed the results from a series of studies by previous researchers could be unrepeatable because of inhomogeneity or thermal gradient. Jin and Chen as well as Gröbner *et al* presented thermodynamic calculations of the system using the available phase diagram and thermodynamic data [31], [32].

3.1 Crystallization of yttrium aluminosilicate glasses

In the past, research on SiAlON glass-ceramics have been focused mainly on two areas: the identification of glass-forming regions for various O/N ratios when additional cations or anions are present in the system and the crystalline products present after appropriate nucleation and crystallization procedures. In the last decades, these classes of glass-ceramics were used as refractory materials, due to their corrosion resistance and classified as high strength materials which normally are used in mechanical engineering in terms of machinable capability [33], [34]. Recently, SiAlON ceramics were also proposed as photonic material due to their unique optical properties [19] [27] [35]. Nucleation in glass-forming melts may occur by different mechanisms that are commonly distinguished as homogeneous and heterogeneous nucleation. It has been known for decades that the addition of specific components .e.g. titania or zirconia to a glass may switch the mechanism from surface to bulk nucleation. These components are known as "nucleating agents", and lead to the precipitation of one crystalline phase in the bulk, which subsequently triggers the crystallization of another, the desired crystalline phase. However, zirconia and titania are common nucleation agents

which influences the devitrification reactions and often trigger volume crystallization in glasses. Although, oxide and oxynitride glasses in this system are generally considered to show homogeneous self-nucleating, it has been confirmed in recent studies that ZrO_2, TiO_2 or a mixture act as nucleating agents in such glasses [36], [37].

Usually crystalline phases possess a higher density than an amorphous phase of the same chemical composition. In analogy, also the thermal expansion coefficients (CTEs) of the crystal and the amorphous phase are different. When the crystallization takes place, stresses are formed in the sample. If more than one phase is formed, they usually have different thermal expansion coefficients. Due to this mismatch, during cooling mechanical stresses are formed. Furthermore, phase transitions, which run parallel to volume expansions or contractions, contribute to stress formation. For instance, in glass-ceramics in the system $MgO/Al_2O_3/SiO_2/TiO_2$ quartz is formed which during cooling shows a phase transition from the high temperature to the lower temperature phase at temperatures in the range from 570 to 500 °C [38-40].

Control of the nucleation process is extremely important for the preparation of glass-ceramics. The crystalline phases formed upon heat treatment and final phase formations will determine the properties of the particular material when they use in desired components. The phases formed depend on both the composition of the parent glass and the heat treatment process. Some glasses require the addition of a nucleating agent to promote crystallization. Howerver, the YSiAlON glasses, in general, appear to be self-nucleating. Although, Thomas *et al* observed improved crystallization behavior for an oxynitride glass containing a small addition of ZrO_2 [18],[22]. Furthermore, Braue *et al.* found a significant improvement of high-temperature strength of (Y_2O_3 + Al_2O_3) fluxed sintered Si_3N_4 ceramics when the initial batch was partially doped with a small amount of ZrO_2 concentration [41]. In contrast, the work of Cheng and Thompson on zirconia additions to nitrogen ceramics did not show no appreciable improvements in mechanical properties and this has been attributed to the difficulty of retaining commutable of ZrO_2 in this system [42].

Bonell *et al* studied YAG crystallization during annealing of a SiAlON/YAG ceramic at 1250 and 1350 °C for 40 h [43]. At complete crystallization a very fine film (of the order of 1 to 2 nm) of amorphous phase was found at two-grain junctions and supposed to be a stable configuration. Hohnke and Tien studied YAG crystallization during annealing of SiAlON/YAG ceramics at 1200, 1300 and 1400°C for 50 h and found a catalytic effect of Pt

when added as a nucleating agent to the glass composition [44]. Small amounts of glass retained in grain boundaries and triple points were identified in the microstructure. Bentsen *et al* investigated the effect of annealing of a SiAlON/YAG ceramic on the thermal diffusivity of the material and found a significant increase after an annealing treatment at 1350 °C for 20 h [45].

Zhao *et al* found that the addition of ZrO_2 to yttrium aluminosilicate glasses as a nucleating agent could enable to shorten the necessary period of nucleation and increase the rate of nucleation [46]. Crystallization studies reported by Drummond on three different systems showed that the addition of nucleating agents may result in the crystallization of the intergranular phases [47]. Vomacka *et al* studied the crystallization behavior of a ZrO_2-containing glass and a ZrO_2-free glass in the $Y_2O_3–Al_2O_3–SiO_2$ system. The glasses were prepared at 1700°C in order to study the effect of ZrO_2 on the nucleation and growth processes. In another investigation, the kinetics of crystallization were studied by this group. The YAG was obtained by surface crystallization from the similar glass composition [48-51].

Despite of numerous experimental studies performed on the $Y_2O_3–Al_2O_3–SiO_2$ system, there are still some differences concerning the melting and crystallization behavior of such glasses. Conflicting data are reported in the literature on the system $Y_2O_3–Al_2O_3–SiO_2$ and the results show a rather complex behavior in this system. More than a dozen different versions of the phase diagram from this system have been published. In the phase diagrams, the following phases are observed: yttrium aluminum monoclinic (YAM), yttrium aluminum perovskite YAP, yttrium aluminum garnet (YAG) as well as yttrium disilicate ($Y_2Si_2O_7$) in various different modifications. The data on the liquidus temperature in the Y_2O_3-rich area, and the thermodynamic stability of YAP are still ambiguous. Some studies revealed that YAP decomposes at temperatures in the range from 1400–1800 °C to form of YAM and YAG, whereas the majority of researchers suggests YAP to be stable from its melting point down to room temperature [52,53].

3.2 Yttrium aluminum system

The phase diagram of the Y_2O_3-Al_2O_3 system shows three ternary compounds, the monoclinic $Y_4Al_2O_9$ (YAM), the $YAlO_3$ perovskite-type (YAP) and the $Y_3Al_5O_{12}$ garnet-type (YAG), with molar ratios Y_2O_3:Al_2O_3 of 2: 1, 1: 1, and 3: 5, respectively (Figure 4). For obtaining the pure YAG, accordingly to the process parameters, especially stoichiometry and homogeneity

of the starting composition must carefully be controlled. In fact, the formation of YAM and/or YAP as intermediate phases (or even second phases in the final products) plays an important role in the YAG fabrication processes. Yttrium orthoaluminate, YAP, may generally, occur as two different phases: orthorhombic (perovskite structure) and hexagonal. The hexagonal YAP form is usually observed as an intermediate phase in wet chemical synthesis of YAG, while in solid-state reactions, only the perovskite form was found. Keith and Roy also reported the formation of $YAlO_3$ (perovskite) with a garnet (cubic) structure at high temperatures using a solid-state reaction.

YAG powders are traditionally prepared by a solid-state reaction using Y_2O_3 and Al_2O_3 powders as the starting precursor materials. This process demands a high temperature of more than 1600ºC in order to obtain YAG and inevitably leads to coarse particles and agglomerations which consequently leads to poor physical properties of the final YAG ceramics. The following reactions revealed the solid-state process occurs by sintering of YAG powder in diffrent steps:

1. $2Y_2O_3$ + Al_2O_3 → YAM
2. YAM + Al_2O_3 → 4YAP
3. 3YAP + Al_2O_3 → YAG

With using the aluminum-rich compositions, first the yttrium-rich YAM phase is formed indicating that the reaction occurs by the diffusion of Al^{3+} into Y_2O_3 grains and thus it seems that the diffusivity of Al^{3+} in Y_2O_3 is higher than that of Y^{3+} in Al_2O_3. It should further be noted that in some compositions, liquid/liquid phase separation occurs. In the literature, it has been reported that the crystallization of $YAlO_3$ and/or $Y_4Al_2O_9$ might be favorable under some circumstances and YAG may crystallize as a second phase. The appearance of these phases shows that the cation distribution in such synthesized YAG precursor might be results of inhomogeneity at the molecular scale [54,55]. It should be mentioned that in the compositions studied in this thesis, the crystallization of $YAlO_3$ and/or $Y_4Al_2O_9$ was not observed. The long diffusion distance caused by coarse powders might induce the crystallization of aluminum-rich phases even though the overall composition is stoichiometric YAG (Y:Al mol ratio = 3:5).
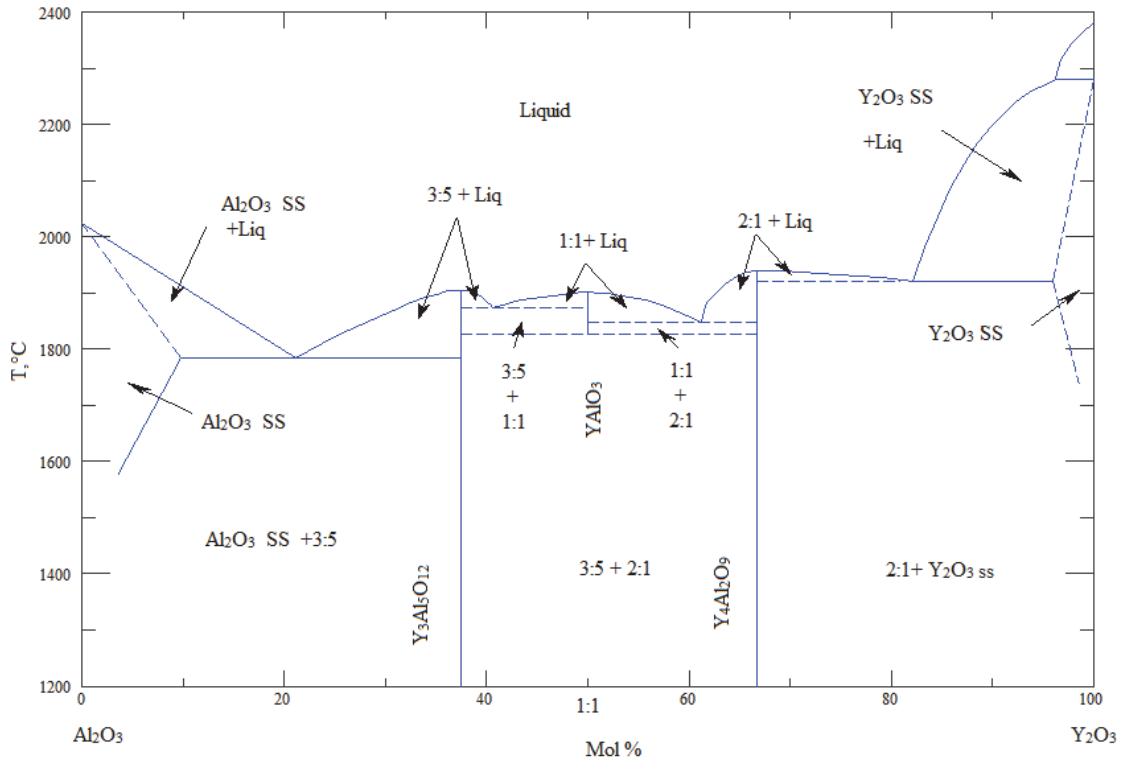
Figure 4. Phase diagram of Y_2O_3-Al_2O_3 system, Ref. [56].

3.3 Yttrium silicate system

In the Y_2O_3–SiO_2 system, two yttrium silicate compounds Y_2SiO_5 and $Y_2Si_2O_7$ are known (Figure 5). Y_2SiO_5 occurs in two different modifications and $Y_2Si_2O_7$ in up to seven polymorphs. Temperatures of transformation between the different $Y_2Si_2O_7$ polymorphs, as described by different researchers, show a broad diversity [57], [58]. The results obtained by Ito *et al* are widely cited in the literature [59]. Later, Becerro *et al* reported a phase-transformation temperature from they to β-$Y_2Si_2O_7$ of 1050 °C [60]. These polymorphs have different unit cell densities: 4.30, 4.03, 4.04, and 4.11 g/cm^3 for the α, β, γ, and δ, polymorph, respectively. Therefore, the polymorphic transformations are accompanied by volume effects, which may induce serious internal stress that might lead to fracture of the materials.

As mentioned above, it is known that the reaction of mixed powders is the most commonly used method for the preparation of ceramic powders. Usually, high temperature (up to 2100 °C for 5–15 h) or a long calcining time (longer than 100 h between 900 and 1800 °C) is needed if Y_2O_3 and amorphous SiO_2 powders were directly used as starting materials for

synthesis of $Y_2Si_2O_7$ and the polymorphs. In addition, high purity and single-phase $Y_2Si_2O_7$ was still not available and never reported in the phase diagram shown in (Figure 5). Even if high purity raw material was used and the high temperature phase was formed at high temperatures, it might have transferred to the low-temperature polymorphs during cooling Kumar et al has drawn hypothetical time-temperature-transformation curves for the eutectic melts of Y_2O_3-SiO_2 [61]. They showed that the synthesis of the high-temperature phases δ and γ $Y_2Si_2O_7$, require a very high quenching rate, e.g. 520 °C/min. The quenching rate has a crucial effect on the formation of the high-temperature polymorphs. Otherwise, α and β $Y_2Si_2O_7$ polymorphs may appear as second phases at lower temperature. They also found γ-$Y_2Si_2O_7$ is a high-temperature phase among the seven polymorphs of $Y_2Si_2O_7$ and it remains stable over a wide temperature range from room temperature to 1500 °C.

As mentioned above, in the literature, seven polymorphs of $Y_2Si_2O_7$ have been described, four of them are frequently characterized and reported in the literature. The crystallographic parameters are briefly summarized in Table 2. The structural parameters are taken from MacLaren, Richter Liddell and Thompson. Meanwhile the data from γ-$Y_2Si_2O_7$ are taken from a study of Leonyuk et al [62-65]. The information of bonding was taken from the complete review article by Felsche [65].

Table 2, Ref. [62].

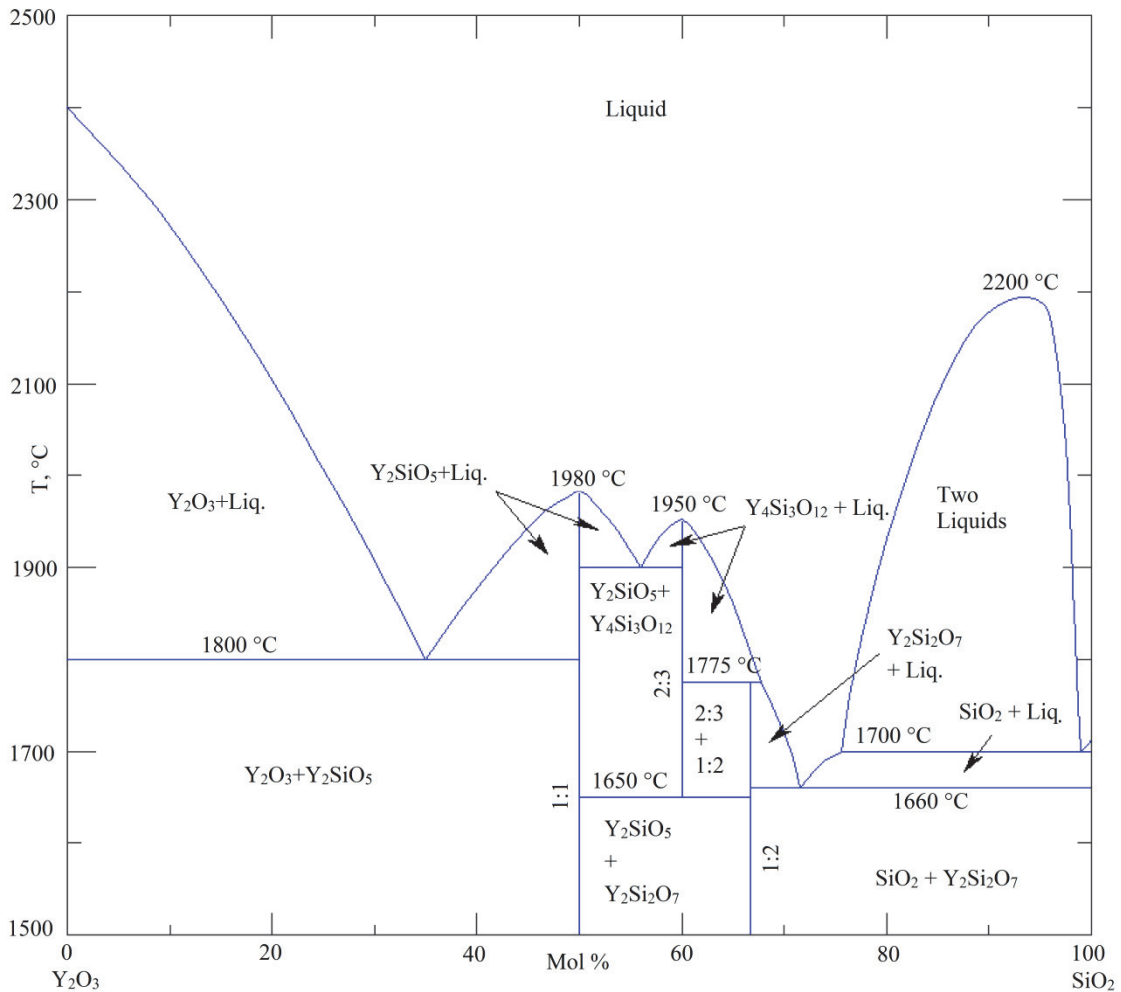| Structure	α-$Y_2Si_2O_7$	β- $Y_2Si_2O_7$	γ- $Y_2Si_2O_7$	δ- $Y_2Si_2O_7$
Symmetry	Triclinic	Monoclinic	Monoclinic	Orthorhombic
Space group	P$\bar{1}$	C2/m	P2$_1$/c	Pna2$_1$
a	6.59 Å	6.875 Å	4.694 Å	13.66 Å
b	6.64 Å	8.97 Å	10.856 Å	5.020 Å
c	12.25 Å	4.721 Å	5.588 Å	8.152 Å
α	94°	90°	90°	90°
β	89.2°	101.74°	96°	90°
γ	93.1°	90°	90°	90°

Figure 5. Phase diagram of Y_2O_3-SiO_2 system, Ref. [66].

In summary, in all studies mentioned above, the crystallization of the YAG requires high temperatures (more than 1200 °C) and relatively long time of thermal treatment. The occurrence of undesired phases was one of the main motivations to reinvestigate this system in order to find new glass compositions suitable to prepare glass ceramics for optical applications. Furthermore, in order to obtain high transparency, the glass-ceramic compositions and crystallization conditions have to be chosen carefully in order to obtain high translucency and hence low light scattering.

4. Characterization techniques

In material sciences it is important to characterize the microstructure and texture of the material under investigation. Grain size, grain shape, grain boundaries, grain orientation,

misorientation and texture distribution may have significant influence on mechanical, optical and electrical properties of the material. In order to study the microstructure and texture of a material, optical microscopy, Scanning Electron Microscopy (SEM) equipped with Energy-Dispersive X-ray spectroscopy (EDX) and Electron Backscattered Diffraction (EBSD), Transmission Electron Microscopy (TEM) and X-ray Diffraction can be used to obtain local information on the microstructure. The main advantage of the EBSD technique lies in the direct access to the local orientation of the material in a measurement point or in the relation between the microstructure and crystallography and for the identification of certain crystalline phases in the microstructure. EBSD became a more frequently used method in metallographic, mineralogy, geology and ceramic materials over the past decade [67], [68]. However, in the last four years, Rüssel and Wisniewski qualified EBSD as a method to characterize glass-ceramics [69-74].

The SEM equipped with EBSD camera is a powerful instrument for acquiring microtexture data and characterizing the local crystallography of materials [75]. EBSD is a technique performed in the SEM. Electrons striking a prepared sample inclined at 70° (to maximum contrast and intensity) may be diffracted according to Bragg diffraction ($n\lambda = 2d_{hkl} \sin \theta$). EBSD in an SEM has become a widely used technique for the determination of microtextures [76]. For this purpose, an SEM was used to provide the electron source, and the diffraction patterns from the tilted specimen were captured using a fluorescent screen interfaced to a closed-circuit monitor camera. The patterns are denoted "electron backscatter patterns" since they comprised the angular distribution of the backscattered electrons after diffraction. Several advantages of the technique over selected area channel (SAC) for obtaining crystallographic information in the SEM were cited: the smaller sampled volume and the much larger angular view of the diffraction pattern. The main effect of tilting the specimen is to reduce the path length of electrons that have been backscattered by lattice planes as they enter the specimen, thus allowing a far greater proportion of these electrons to undergo diffraction and escape from the specimen before being absorbed.

A highly recommended method for preparing a variety of specimens for EBSD is polishing the samples in colloidal silica, since this does not introduce the harsh mechanical damage associated with diamond-like polishing.

The prepared glasses were further characterized with a dilatometer using a heating rate of 5 K/min to discern the T_g samples. The glasses and annealed samples were characterized by X-ray diffraction (Siemens D5000) using $Cu_{K\alpha}$ radiation. Differential Thermal Analyses

(Shimadzu DTA50) were carried out in air using an Al_2O_3 powder reference standard and a heating rate of 5 K/min (from room temperature to 1400 °C). Fluorescence optical micrographs (FM) were obtained via laser scanning microscopy (LSM) using an Axio Imager Z1M LSM5-Pascal (Carl Zeiss AG, Oberkochen, Germany). The microstructures of several glass-ceramics were studied using a Schottky field-emission scanning electron microscope Jeol-JSM 7001F equipped with EDAX Trident system (EDS, WDS and EBSD detector). Some selected samples were further studied by transmission electron microscope (TEM) using the HITACHI H8100 at 200 kV.

5. Summary of the experimental results

In the present work, a series of alkali free and alkali glasses were prepared based on the system Y_2O_3/Al_2O_3/SiO_2/AlF_3 doped with Ce^{+3}-doped system. In the alkali free glasses the effect of nucleation agents, ZrO_2, TiO_2 and a mixture hereof was studied. The raw materials were chosen and prepared using a conventional melt-quench technique. The as prepared glasses were cut and thermally annealed. Thermal annealing of the glass was carried out at temperatures in the range from 1100 to 1400°C.

The prepared glass-ceramics have been studied using X-ray diffraction (XRD), scanning electron microscopy (SEM), differential thermal analysis (DTA) and fluorescence microscopy as well as fluorescence spectroscopy. In all studied samples, crystallization at temperatures $\geq$1300 ° C led to the formation of YAG as the main crystalline phase. If the glass contained TiO_2, the crystallization of YAG occurred at lower temperatures; here, already at 1150°C, YAG was the main crystalline phase. After annealing at 1300°C, the only crystalline phase formed was YAG. The results from SEM showed the microstructures of the glass-ceramics were considerably different depending on the respective compositions. Fluorescence spectroscopy was used to investigate optical properties of glass-ceramics. The fluorescence spectra revealed a maximum at a wavelength of around 530 nm and was largest in the sample solely doped with 5 mol% TiO_2. This proves that Ce^{3+} was incorporated into the YAG crystals. This was also observed in fluorescence microscopy where only the YAG crystals gave an intense green fluorescence if irradiated with UV light. In samples sintered at intermediate temperatures in the range from 1150 to 1300 °C $Y_2Si_2O_7$ was observed as an additional crystalline phase. The crystallization of this phase has frequently been reported in

the literature as an additional phase during crystallization of YAG, however, different polymorphs were distinguished by XRD.

In order to investigate a possible modification of the crystallization process, with respect to the formed $Y_2Si_2O_7$, a glass with 5 mol% ZrO_2 was prepared and studied by XRD and EBSD. Six crystalline phases are detected in the residual glass including alumina, YAG, Y-stabilized zirconia (YSZ), and three different yttrium silicates all with the composition $Y_2Si_2O_7$. Chemistry-assisted Indexing (ChI) was successfully applied to separate YAG and YSZ in EBSD-scans. The YAG crystals show both polygon morphology as well as dendritic growth. The YAG crystals were randomly distributed also with respect to their orientation. The α-alumina phase (corundum) was also detected in the sample with both XRD and EBSD. The SEM image showed strias containing a high quantity of elongated corundum crystals and dendritic YAG, while outside the stria polygon YAG and a low quantity of corundum crystallized. The crystals consisting of yttria stabilized zirconia all possessed the shape of small spheres and did not show a discernible texture. $Y_2Si_2O_7$ crystals occur as three different phases, i.e. as three crystallographically different species. The following phases: monoclinic ε-$Y_2Si_2O_7$, orthorhombic δ-$Y_2Si_2O_7$ and monoclinic β-$Y_2Si_2O_7$ could clearly be distinguished using EBSD.

In another series of experiments, alkali as well as fluorine containing glasses with different amounts of CaO were prepared to study crystallization of YAG in glasses in presence of network modifier concentrations. The calcium oxide concentration was varied between 10 and 40 mol%, while the CeF_3 and the SiO_2 concentrations were kept constant. The Y_2O_3/Al_2O_3 ratio was kept in a narrow range between 0.20 and 0.22 in all samples the glass transition temperature, T_g of the glasses decreased with increasing CaO concentration from 820 to 720 °C. The as casted glasses were polished and subsequently transferred to a furnace preheated to 770 °C. Then the furnace was heated to 1200 °C using a rate of 10 K min^{-1}, this temperature was kept for 6 h. In all glasses heat-treated at 1200 °C the crystallization of yttrium aluminum garnet as the only crystalline phase was observed. Crystal growth occurred in the form of large dendrites with significant quantities of residual glass between dendritic arms. While samples with 20 and 30 mol% CaO were composed of many dendrites, samples with 10 mol% CaO show a large dendritic single crystal as proved by EBSD and for the sample with 40 mol% CaO only very few cubic dendrites were observed. This indicates a significant effect of CaO on the nucleation rate and crystal growth velocity in the glasses. Fragmentation of dendrites was not observed in all samples.

Another possibility to reduce the temperature of YAG crystallization is the addition of Na_2O as another network modifier. Glasses with high Na_2O concentrations (more than 7 mol%) showed phase separation or crystallization during casting of the glass melt. By contrast, 3 mol% of Na_2O in a glass of the system $Y_2O_3/Al_2O_3/SiO_2/AlF_3/CeF_3/B_2O_3$ resulted in a transparent and X-ray amorphous glass without any hint of crystallization. The addition of 3 mol% B_2O_3 was effective to reduce T_g and enabled the preparation of homogenous glass. Samples from this glass were crystallized at 1000 °C for 3, 6, 12 and 12 h. As prepared glass-ceramics indicate the presence of up to five crystalline phases in the samples; three of them in the context of surface crystallization and two resulting from bulk nucleation. Surface crystallization leads to three distinct layers: the first layer was about 30 μm thick, showed green fluorescence if irradiated with UV-light. This phase was probably Ce^{3+} doped YAG. While the thickness of the first layer is about 30 μm and does not depend on the crystallization time, the second layer varies in thickness and may locally be only few micrometers thick. Layer 2 was not continuous but reaches a thickness of up to 100 μm. The third layer also nucleated adjacent to layer one and grew also in the bulk. The second and third layer did not show any luminescence. In the bulk, nucleation and subsequent growth of an X-ray amorphous star-shaped and alumina enriched phase leads to a depletion of alumina from the glass. An EDX line scan confirmed the lower alumina concentration between the crystals and an enrichment of the glass matrix in yttrium and silicon. SEM-micrographs show that the star-shaped phase covers about 12 % of a cut plane after 3 h and roughly 30 % after 6 and 12 h.

EBSD was applied in order to identify the crystalline phases, to analyze orientation relationships between them and ratify their location because the XRD-results were inconclusive. The EBSD-patterns were recorded from four phases in the microstructure which allow acceptable pattern acquisition. EBSD patterns were obtained from the dendrites in layer 1 and reliably indexed as YAG, while the crystals of layer 2 were reliably indexed as monoclinic $Y_2Si_2O_7$. The third crystallized layer yielded the EBSD-pattern which were reliably indexed as orthorhombic $Y_2Si_2O_7$. The fourth EBSD-pattern was obtained from the bulk and can be reliably indexed as another monoclinic $Y_2Si_2O_7$. The phase identification of these yttrium silicates is purely based on the chemical composition and the crystallography analyzed by EBSD and could not be proved by XRD. EBSD-patterns of the star-shaped crystals were obtained, but could not be indexed due to their low quality, however, illustrated that this phase is crystalline.

In a further series of experiments, the 3 mol% Na_2O were substituted against CaO while keeping the molar concentrations of all other components constant. The glasses were heat-treated at 1000 °C for 24, 48 and 72 h. In analogy to the Na_2O containing glass-ceramics, also the CaO containing glass-ceramics exhibit surface nucleation. However, the CaO glass-ceramics, show fairly different crystallization behavior and hence different microstructures. Several images were recorded by a laser scanning microscope (LSM) from the cross-section of the annealed sample showed at at least three different crystal morphologies are observed at the surface and in the bulk of the sample. Near the surface, a clearly visible crystalline layer occurs, formed by surface crystallization. The elongated shape of the surface crystals suggests that the crystals are nucleated near the surface and are grown subsequently into the bulk. This surface layer consists of a lamellar structure composed by yttrium aluminum garnet and yttrium silicate. The garnet surface layer is doped with Ce^{3+} as seen from the intense broadband fluorescence. The nano lamellae originated from the surface and grew in an interpenetrating cell structure with an interspace of about 50 nm. Simultaneously, the growth of star-shaped, aluminum enriched crystals, took place in the bulk of the sample that was similar to the Na_2O containing glass. Around the star-shaped crystals, a diffusion layer depleted in aluminum was observed. Experimental XRD-patterns obtained directly from the surface of the annealed samples show characteristic peaks which can be attributed to YAG, y-$Y_2Si_2O_7$ and α-$Y_2Si_2O_7$.

The star-shape structures in both sample series also grew in both series with increasing annealing time. If they are near the surface, the surface crystallized layer grows around them until they are fully surrounded by the crystals that have grown from the surface.

EDS-maps recorded in SEM from the cross section near the star-shape structure showed that it predominantly consists of aluminum as shown in the EDS-map. Around the crystal, the residual glassy phase is depleted in aluminum. Studies by point analyses using EBSD proved that the dark appearing star-shape structure is also crystalline (Kikuchi pattern could be obtained but not indexed).

5.1

A. Keshavarzi and C. Rüssel

The Effect of TiO_2 and ZrO_2 Addition on the Crystallization of Ce^{3+} Doped Yttrium Aluminum Garnet from Glasses in the System $Y_2O_3/Al_2O_3/SiO_2/AlF_3$
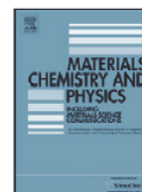
The effect of TiO_2 and ZrO_2 addition on the crystallization of Ce^{3+} doped yttrium aluminum garnet from glasses in the system $Y_2O_3/Al_2O_3/SiO_2/AlF_3$

Ashkan Keshavarzi, Christian Rüssel*

Otto-Schott-Institut, Jena University, Fraunhoferstr. 6, 07743 Jena, Germany

ARTICLE INFO

ABSTRACT

The crystallization of yttrium aluminum garnet (YAG) doped with Ce^{3+} from alkali free glasses in the system $Y_2O_3/Al_2O_3/SiO_2/AlF_3$ has been investigated with and without the addition of ZrO_2 and/or TiO_2 as nucleation agents. X-ray diffraction (XRD), scanning electron microscopy (SEM) and differential thermal analysis (DTA) were used to characterize the crystallization process. Fluorescence microscopy and fluorescence spectroscopy were used to investigate optical properties. Thermal annealing of the glass was carried out at temperatures in the range from 1100 to 1400 °C. In all samples studied, crystallization at temperatures ≥ 1300 °C lead to the formation of YAG as the main crystalline phase. If the glass contained TiO_2, the crystallization of YAG occurred at lower temperatures; here, already at 1150 °C, YAG was the main crystalline phase. After annealing at 1300 °C, the only crystalline phase formed was YAG. The fluorescence intensity showed a maximum at a wavelength of 532 nm and was largest in the sample solely doped with 5 mol% TiO_2. This proves that Ce^{3+} was incorporated into the YAG crystals.

© 2011 Elsevier B.V. All rights reserved.

1. Introduction

Luminescence properties of yttrium aluminum garnet ($Y_3Al_5O_{12}$, YAG) have widely been studied because of its importance for lighting applications [1]. Most commercial white light emitting diodes (LEDs) use a GaInN blue emitter with an emission peak at 460 nm in combination with a YAG:Ce^{3+} yellow phosphor [2,3]. For that purpose, up to now, mostly YAG powder is embedded in a polymer, usually a polysiloxane [4,5]. In this composite, strong absorption in the blue spectral range and a broad re-emission centered at around 530 nm is observed. Since polymers possess a poor thermal conductivity, heat generated in the phosphor cannot effectively be removed. This strongly limits the maximum light intensity of the LEDs. Hence, especially for high power applications, it would be highly advantageous if the YAG crystals were directly incorporated into a glass matrix which is much more thermally conductive. Furthermore, YAG crystals embedded in an inorganic matrix are very stable against any kind of corrosion. The technological path to fabricate a material in which Ce^{3+}-doped YAG is embedded in a glassy and transparent matrix is the glass crystallization process and the materials prepared using this path are usually denoted as glass–ceramics. Routes for the preparation of YAG containing glass–ceramics are scarcely described in the literature. For example, Tarafder et al. recently reported preparation and properties of RE-doped glass–ceramics

in the $K_2O/SiO_2/Y_2O_3/Al_2O_3$-system prepared by a controlled crystallization technique [6,7]. Usually, silicate glasses which contain the two required components, Y_2O_3 and Al_2O_3 do not possess a high tendency towards crystallization, and if they crystallize, fairly high temperatures are required or, however, the crystalline phase is not YAG. In melts, containing K_2O concentrations as high as 28 mol%, YAG crystallization has nevertheless been described during annealing at temperatures ≥ 750 °C. Due to the large alkali concentration, however, chemical durability at elevated temperatures and high humidity, however, should be insufficient for many purposes [6,7]. The aim of this study is to introduce a route which enables the preparation of a translucent glass–ceramics containing cerium doped yttrium aluminum garnet at comparably low temperatures.

In the present work, an alkali free glass was used. For that purpose, a glass based on the system $Y_2O_3/Al_2O_3/SiO_2/AlF_3$ doped with Ce^{3+}-doped was chosen and prepared using a conventional melt-quench technique. Subsequently, the glass is thermally annealed. The as prepared glass–ceramics have been studied using X-ray diffraction (XRD), scanning electron microscopy (SEM), differential thermal analysis (DTA) and fluorescence microscopy as well as fluorescence spectroscopy. The effect of nucleation agents, ZrO_2, TiO_2 and a mixture hereof is studied.

2. Experimental procedure

Glasses in the system $Y_2O_3/Al_2O_3/SiO_2/AlF_3/ZrO_2/TiO_2$ doped with CeF_3 (1 mol%) were prepared from pure reagent grade raw

* Corresponding author. Tel.: +49 3641 9 48501; fax: +49 3641 9 48502.
E-mail address: ccr@rz.uni-jena.de (C. Rüssel).

Table 1
Glass compositions and formed crystalline phases for different annealing temperatures.

#	Chemical composition (mol%)							Annealing temperature (°C) (20 h)						
No.	Y_2O_3	Al_2O_3	SiO_2	AlF_3	ZrO_2	TiO_2	CeF_3	1100	1150	1200	1250	1300	1350	1400
A	20	34.1	40	4.8	–	–	1	Opaq	YAG YS	YAG YS	YAG YS	YAG YS+YO	YAG YO	YAG – YO
B	20	34.1	35	4.8	5		1	YAG – YS	YAG YS	YAG YS	YAG YS	YAG	YAG – ZrO_2	YAG – ZrO_2
C	20	34.1	35	4.8	2.5	2.5	1	Opaq	YAG YS	YAG YS – TO	YAG YS	YAG	YAG	YAG
D	20	34.1	35	4.8	–	5	1	Opaq	YAG TO	YAG TO – YS	YAG TO – YS	YAG YS	YAG	YAG

Opaq: the sample is opaque, but crystalline phases were not detected by XRD; YAG: yttrium aluminum garnet; YS: yttrium disilicate; ZrO_2: non monoclinic zirconia; TO: titanium oxide; YO: yttrium oxide.

materials. The chemical compositions of the samples are summarized in Table 1. Sample A does not contain any nucleating agent. By comparison, in sample B, the molar yttria and alumina concentrations were kept constant, while 5 mol% SiO_2 were replaced by 5 mol% ZrO_2. In sample C, 2.5 mol% ZrO_2 and 2.5 mol% TiO_2 were used as nucleating agents, while sample D was doped with 5 mol% TiO_2, The mixed batch consisting of 100 g raw material was melted in a platinum/rhodium 10 crucible in an electric furnace at 1600 °C kept for 4 h in air with intermittent stirring. The melt was subsequently quenched by casting on a copper mold. The obtained glass was annealed using the temperature profile shown in Table 1.

Glasses and annealed samples were characterized by X-ray diffraction (Siemens D5000) using Cu Kα radiation. Differential Thermal Analyses (Shimadzu DTA50) were carried out in air using Al_2O_3 powder reference standard and a heating rate of 5 K min^{-1} (from room temperature to 1400 °C).

The microstructures of the glass–ceramics were studied using a field-emission scanning electron microscope FE-SEM Jeol-JSM 7001F.

Fluorescence optical microscopy Zeiss LSM5 Pascal Axio Imager (with filter No. 09) was used to study the fluorescence emission of particular crystals from the microstructures of the respective glass–ceramics.

3. Results and discussion

While the casted glasses were optically transparent and amorphous as proved by XRD, samples thermally annealed at temperatures ≥950 °C were opaque. However, these samples were still amorphous. The first XRD-peaks proving the formation of crystalline phases were observed after thermal annealing at a temperature of 1150 °C.

XRD patterns of the prepared glass–ceramics using different nucleation agents are shown in Fig. 1 for different annealing temperatures. The crystallization products detected by X-ray diffraction after annealing the samples for 20 h are summarized in Table 1. To trace crystallization temperature and to compare them with XRD results, the DTA result from glass samples under investigation is profiled in Fig. 2.

The XRD patterns for glasses with the composition A annealed at temperatures ≥1150 °C showed small diffraction peaks and hence an evidence of the formation of crystalline phases based on the DTA plot of glass A, there are three exothermic peak observed that are Corresponding to crystallization processes in the respective glass. The first peak is attributed to the crystallization of $Y_2Si_2O_7$ and second small peak is corresponding to YAG that is consistent with previous studies of Vomacka et al. [8]. The first crystalline phases formed at 1150 °C were $Y_2Si_2O_7$ (JCPDS No. 74-1994) and YAG (JCPDS No. 01-088-2047). The intensities of the XRD-peaks obtained from samples annealed at comparably low temperatures are small and no specified peaks were detected. This is probably due

to small nucleation rates caused by the lack of nucleation agents and to small crystal growth velocities. With increasing temperature, the intensities of the peaks get stronger. When the annealing temperature was increased to 1300 °C, and lines due to Y_2O_3 (JCPDS No. 79-1257) were observed but small amount of the $Y_2Si_2O_7$ phase was still formed in glass–ceramic. Hence, with a glance on DTA curve a small peak is clearly observed and corresponding only to this crystalline phase.

The XRD patterns for glass composition B after annealing at temperatures in the range from 1150 to 1250 °C showed peaks attributable to YAG (JCPDS No. 01-088-2047) and y-$Y_2Si_2O_7$ (JCPDS No. 00-042-0168). At these temperatures only these two crystal phases were formed during annealing. Although, only one broad peak is observed in the corresponding DTA curve between 1100 and 1250 °C it is strongly believed this could be attributed to the YAG and $Y_2Si_2O_7$ crystallization process. When the crystallization of both phases takes place at the same temperature, one broad peak is revealed Instead of two distinguished peak. Although, at 1250 °C XRD peaks position of YAG crystal was the same as at higher temperature and is matched with different YAG (JCPDS No. 01-082-0575) crystals, YAG is crystallized in the different lattice parameter and coinciding with different JCPDS file. By contrast, after annealing at 1300 °C, YAG became the most dominate phase. After annealing at temperatures above 1350 °C, ZrO_2 (JCPDS No. 79-1769) is additionally precipitated. The phase formed is clearly not monoclinic; however, cubic and tetragonal zirconia are hardly to distinguish, if zirconia occurs in minor concentrations and hence the attributed XRD-peaks are of low intensity.

In the case of glass C which contained both ZrO_2 and TiO_2, annealing at temperatures in the range from 1150 to 1250 °C resulted in glass–ceramics with the crystal phases YAG (JCPDS No. 01-0751853) and Y-$Y_2Si_2O_7$ (JCPDS No. 00-042-0168). In this glass–ceramic, YAG also crystallized in the different JCPDS file and was matched with JCPDS No. 01-0751853. However, this group is also characterized as garnet group in XRD data sources. The intensity of the XRD peak gets stronger than in the other YAG samples that is a result of crystal growth velocities caused by higher nucleation rate in the presence of nucleation agent. In this glass–ceramic, YAG crystallized in a different lattice parameter. Additionally, trace quantities of TiO_2 (rutile JCPDS No. 75-1751) were identified after annealing at 1200 °C. Although, in the DTA curve there was no sign of correspond to TiO_2. At higher temperatures, YAG was the only crystalline phase in the glass–ceramic sample.

In sample D, only TiO_2 was used as nucleation agent. Also in this case, YAG (JCPDS No. 01-088-2047) occurred as the only crystalline phase after annealing at 1400 °C. The shape of the precipitated crystals was significantly different from sample C and polygonal crystals were the only observed morphology in the glass–ceramics. This is in agreement with the XRD-patterns where although after annealing at temperatures in the range from 1150 to 1250 °C, TiO_2 (rutile) was observed, annealing at 1400 °C does not result in the
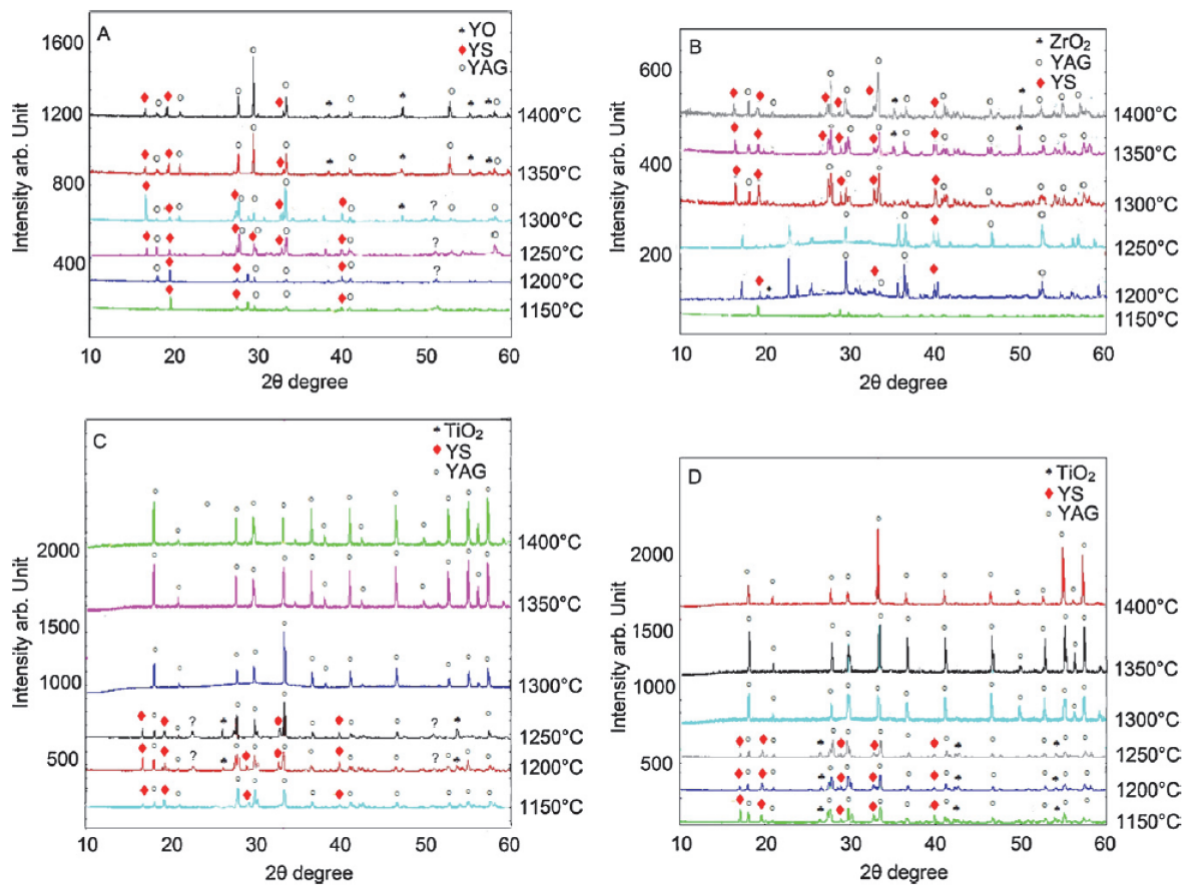
Fig. 1. XRD-patterns of glass–ceramic samples A, B, C and D. YAG: $Y_3Al_5O_{12}$, YS: $Y_2Si_2O_7$, YO: Y_2O_3.

crystallization of rutile. Meanwhile, trace of TiO_2 was not observed in the DTA plot of sample C. In all samples some differences to the JCPDS files were observed.

The shape, size and morphology of the prepared glass–ceramics were studied by SEM. Fig. 3 shows SEM-micrographs of polished samples after thermal annealing at 1400 °C. The morphology of the crystals is significantly affected by the annealing conditions. The
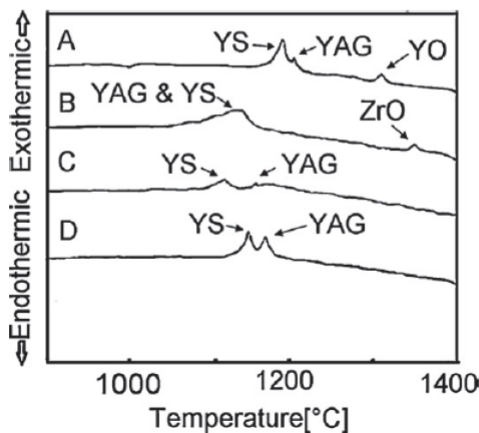
Fig. 2. DTA-profiles of the investigated glasses using a heating rate of 10 K min^{-1}.

SEM micrograph of sample A annealed at 1400 °C shows three main phases. The dark phase is related to the glassy matrix, the grey phase represents YAG crystals (the compounds detected by EDX were yttrium and aluminum), and the white crystals consist of Y_2O_3 (only yttrium was detected by EDX). The YAG crystals possess sizes in the range from 10 to 70 μm. The occurrence of cerium in the crystals was proved by EDX, a quantitative determination was not possible due to the small cerium concentration. The particles sizes of Y_2O_3 were smaller than 10 μm and were all adjacent to YAG crystals.

The YAG crystals of glass–ceramic sample with ZrO_2 as nucleation agent (sample B) annealed at 1400 °C showed approximately the same morphology. However, the phase of light appearance was not Y_2O_3, but ZrO_2 which was crystallized in a dendritic morphology.

In the SEM-micrograph of sample C annealed at 1400 °C, the YAG phase precipitated in different morphologies and both, polygons and dendrites are formed. In this sample, both ZrO_2 and TiO_2 were used as nucleation agents and according to the XRD-pattern, the only crystalline phase formed at this temperature was YAG. It should be noted, however, that the polygon was still the predominant morphology.

In sample D, only TiO_2 was used as nucleation agent. Also in this case, YAG occurred as the only crystalline phase after annealing at 1400 °C. The shape of the precipitated crystals was significantly different from sample C and polygonal crystals were the only observed morphology in the glass–ceramics. This is in agreement with the
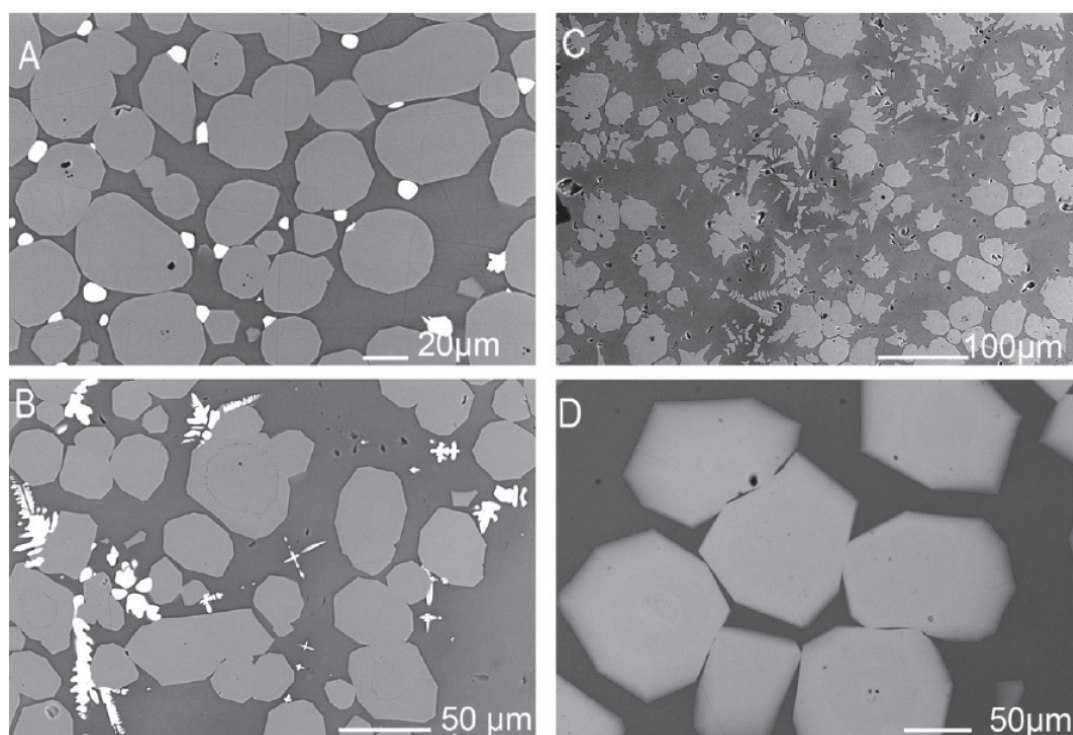
Fig. 3. SEM-micrographs of glass–ceramic samples A, B, C and D annealed at 1400 °C.

XRD-patterns where although after annealing temperatures in the range from 1150 to 1250 °C, TiO_2 (rutile) was observed, annealing at 1400 °C does not result in the crystallization of rutile.

As shown in the SEM-micrographs, the microstructures of the glass–ceramics were considerably different depending on the respective composition. According to some reports in the literature [8–10], ZrO_2 promotes the formation of $Y_2Si_2O_7$ and consequently the crystallization of the YAG phase should be inhibited. Vomacka et al. [11] investigated the effect of ZrO_2 in glasses with the wt% compositions $x\,ZrO_2(100-x)\,[46.9\,Y_2O_3\cdot24.5\,Al_2O_3\cdot28.8\,SiO_2]$ (for $x=0$ and 6). It was reported, that ZrO_2 crystals are observed in annealed samples. These precipitates probably remained from glass melting and served as nucleating centers for the crystallization of $Y_2Si_2O_7$ phase. From these experiments, the conclusion was drawn, that Zr^{4+} acts as nucleating agent in this glass [12,13].

Already a long time ago, the nucleating effect of ZrO_2 and TiO_2 in many glass systems has been reported. It has further been reported that the addition of these components enables the production of very fine grained and homogeneous glass–ceramics. In this context, Maier and Müller studied already in 1987 the formation of $ZrTiO_4$ nanocrystals and their effect of the crystallization of quartz from lithium aluminosilicate glass–ceramic using transmission electron microscopy [14]. Recently, Höche et al. [15,16] showed that in a lithium aluminumsilicate glass, the initial formation of nanocrystalline $ZrTiO_4$ is accompanied by the formation of an aluminum enriched shell around these nano crystals. Using transmission electron microscopy in combination with X-ray absorption near-edge structure spectroscopy (XANES) showed the crystallization of $ZrTiO_4$ is a two-stage process. In the first stage, phase separation occurs and Ti^{4+} is enriched in a droplet phase; in the second stage, the droplets are crystallized. The initially octahedral coordination of the titanium ions in the amorphous liquid-liquid phase separation droplets, transfers into the eight fold coordination occurring in $ZrTiO_4$. The formed $ZrTiO_4$ crystals are only a few

nanometer in diameter after long thermal treatment. Subsequently, crystal growth of nanoparticles is hindered by a diffusion barrier which results from the alumina rich layer, i.e. the formation of the core/shell structure described above [17].

In the case of sample C which contains both ZrO_2 and TiO_2, the XRD-patterns after annealing do not show any evidence of the formation of $ZrTiO_4$. This is in agreement with the micrograph shown in Fig. 3C where only the garnet phase is seen. The phase formation in this sample is approximately the same as in sample A which does neither contain ZrO_2 nor TiO_2.

The morphology of the YAG crystals in sample C differs notably from those of all other samples. The crystals do not show the polygonal shape but appear to be grown as dendrites. In the presence of TiO_2, the main phase formed is YAG and other phases are not observed in the XRD patterns after annealing at temperatures above 1250 °C. In the samples A and B other phases are still present
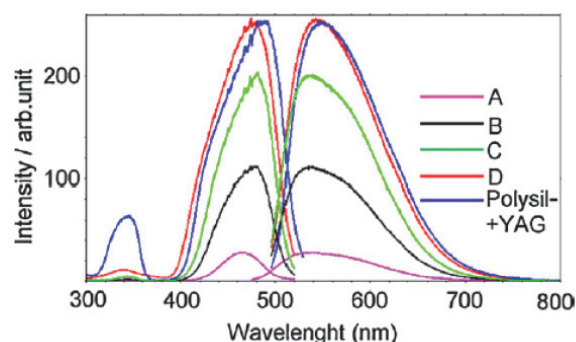

Fig. 4. Photoluminescence excitation emission spectra of YAG:Ce^{3+} of the glass–ceramic samples A, B, C and D, and YAG-polysiloxane (Tridonic Co.) exited at 460 nm.
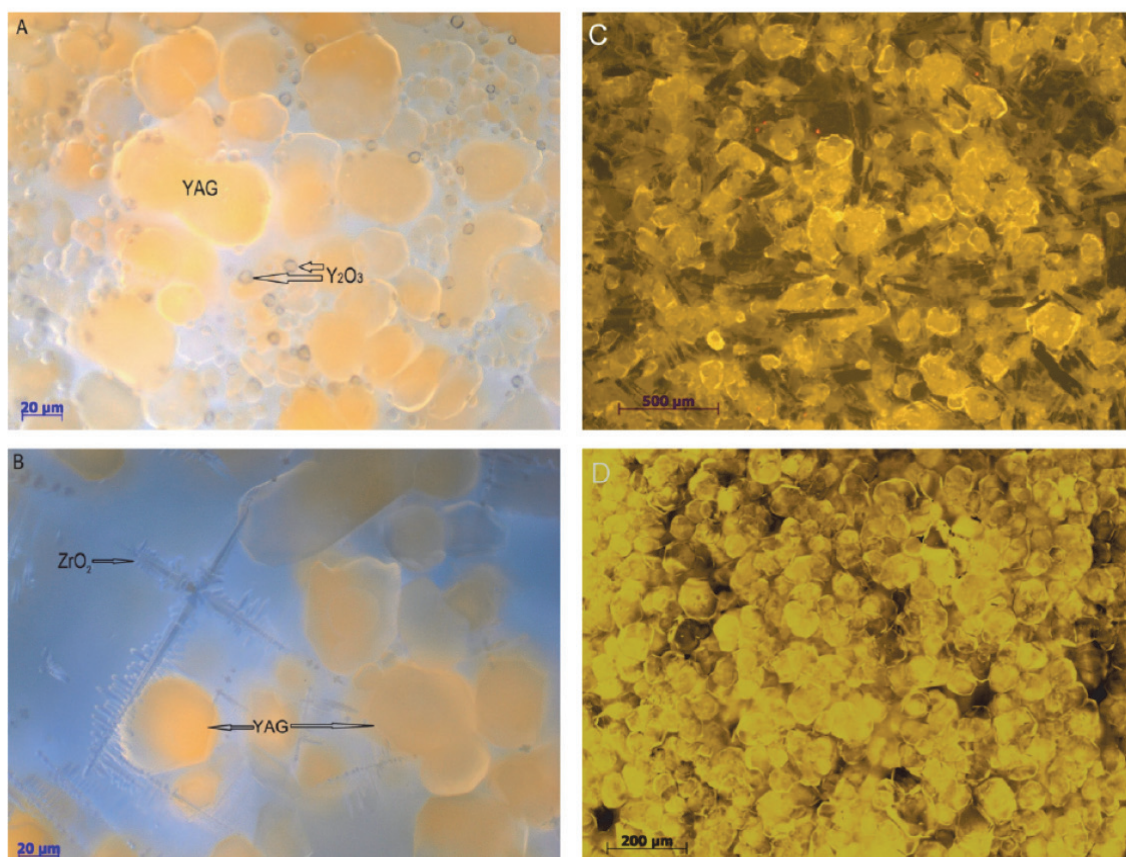
23

Fig. 5. Fluorescence microscopy micrography of the glass–ceramic samples A and B, both thermally annealed at 1400 °C.

after annealing at 1300 °C. It should hence be assumed that TiO_2 acts as nucleating agent for the formation of YAG at temperatures ≤1250 °C. It should be noted, however, that the effect of TiO_2 as nucleating agent strongly depends on its concentration. At temperatures >1250 °C, TiO_2 is no longer formed and hence cannot act as nucleating agent. With increasing temperatures, the oversaturation of TiO_2 in the glass forming liquid decreases and is obviously not high enough to result in a precipitation of titania.

In this work AlF_3 was used as raw material. In the glass network, monovalent F^- is incorporated and partially substitutes O^{2-}. In the literature, it is frequently described that a partial replacement of oxygen by fluorine leads to a decrease in viscosity. In some oxyfluoride glass compositions, the structure of the glasses has been studied by solid state NMR spectroscopy or RAMAN spectroscopy [18,19]. Among the studied glasses are alkali and alkaline earth silicates and aluminosilicates. In the alkali containing aluminosilicate glasses, fluorine occurs as Na–F–Al complex, while in the respective alkaline earth compositions, it is predominantly incorporated as R–F–Al (R = Ca, Ba) complex. Although, rare earth aluminosilicates were up to now scarcely investigated using NMR, in these glasses Al–F or Y–F–Al structures should be formed; Si–F bonds should not occur in these glasses. Furthermore, Muñoz et al. [20] recently reported ^{19}F NMR studies carried out in a glass from the system $Na_2O/Al_2O_3/SiO_2/LaF_3$ and in glass–ceramics derived hereof. They concluded that fluorine is incorporated in the glass as Al–F–Na or La–F structures. Thus, a narrow range order La–F or possibly La–F–Na already exists in the glass after melting.

Since as noted above, the partial replacement of oxygen by fluorine in these glasses leads to a decrease in the viscosity, both the

nucleation rate as well as the crystal growth velocity should be larger than in the corresponding purely oxide glass. Furthermore, the crystallization of alkaline earth fluorides or rare earth fluorides from aluminosilicate glasses has frequently been reported in the literature [21–23]. The solubility of the corresponding fluorides in the glass strongly decreases with increasing fluorine concentration. However, the fluorine concentrations used in this investigation are obviously too small to cause the crystallization of yttrium fluoride. Hence, the partial substitution of oxide by fluoride does not seem to provide nucleation sites which enable the growth of YAG crystals from the glassy matrix [24–27].

Fig. 4 shows excitation and emission spectra of the YAG:Ce^{3+} glass–ceramics A, B, C, and D after annealing at 1400 °C and YAG embedded in polysiloxane from Tridonic company as a commercial reference to compare the potential of the glass–ceramics to replace as a light converter. All samples had a thickness of 0.28 mm. For the fluorescence measurements, the samples were exited using a wavelength of 460 nm. This results in a broad emission band which is attributed to the electron transitions from the lowest crystal-splitting component of 5d level to the ground state of Ce^{3+} ($^2F_{5/2}$, $^2F_{7/2}$) [28,29]. The intensities of the emission spectra are found to depend on the composition of the glass–ceramics. While the maxima in the emission spectra of samples B, C, and D were observed at a wavelength of 540 nm that of the glass–ceramic sample A was shifted to a slightly smaller wavelength of around 525 nm. Fig. 4 also presents an excitation and an emission spectrum recorded from a commercial Ce^{3+} doped YAG sample prepared by mixing the oxides, thermal annealing and subsequent embedding in a polysiloxane sample. The intensity of the commercial sample and sample D are

24

approximately the same but there is a 10 nm difference between the emission spectra. This difference is possibly due to the Ce^{3+} concentration incorporated into the YAG crystals. But in this case, measuring of Ce^{3+} was not successful and we are not able to determine the exact amount of dopant inside the YAG crystals. The intensities of samples A and D differ by approximately the factor 2. This effect should predominantly be due to differences in the light scattering which is also affected by the microstructure formed. Here, a comparably small extend of light scattering should lead to a maximum in the emitted light, because then the path length of the light through the sample is much longer than the length of the sample. If light scattering occurs in a higher extend, then the intensity of the emitted light is smaller again due the much larger path length and the related absorption.

In Fig. 5, optical micrographs of the glass–ceramic samples A and B both annealed at 1400 °C are shown. They were recorded using fluorescence microscopy with an excitation wavelength of 450 nm. In the micrograph of sample A, the large YAG crystals are seen with diameters of around 50 μm, and besides, small Y_2O_3 crystals with diameters in the range from 3 to 7 μm. In sample B, the observed YAG crystals have approximately the same size; additionally, however, ZrO_2 crystals are observed which exhibit a dendritic morphology. The optical micrographs are in agreement with the SEM micrographs and with the XRD-patterns. The light emitted from the YAG crystals is of yellow color, and only the YAG crystals contributed to the light emission. This proves that Ce^{3+} is incorporated into the YAG crystals.

The prepared glass–ceramics should possess much higher chemical durability and thermal conductivity than Ce^{3+} doped YAG particles embedded in a polysiloxane matrix and should therefore be suitable for high power light converters. Furthermore, the glass–ceramics prepared do not contain any alkali and hence should also show much higher chemical durability especially at higher temperatures and higher humidity than glass–ceramics containing high alkali concentrations. The glass–ceramics are translucent and hence the converted light is emitted from the sample.

4. Conclusion

A series of YAG containing glass–ceramics were studied with respect to their crystallization behavior, the microstructure formed and the fluorescence properties. The effect of the nucleating agents ZrO_2 and/or TiO_2 was studied. In all samples, the main formed phase was YAG after annealing at temperatures ≥ 1300 °C. In the case of TiO_2 addition, YAG was the predominant phase formed already after annealing at 1150 °C, and the only formed phase after annealing at temperatures ≥ 1300 °C. The fluorescence spectra show a maximum at 532 nm. Only the YAG crystals contribute to the light emission. This proves that Ce^{3+} is incorporated into the YAG crystals. Due to their much higher thermal conductivity and chemical durability, in comparison to the phosphor embedded in polysiloxane, the prepared glass–ceramics should be suitable for high power light converters.

References

[1] J.D. Furman, G. Gundiah, K. Page, N. Pizarro, A.K. Cheetham, Chem. Phys. Lett. 465 (2008) 67–72.
[2] J.H. Yum, S.S. Kim, Y.E. Sung, Colloids Surf., A 251 (2004) 203–207.
[3] G. Lakshminarayana, H. Yang, J.J. Qiu, Solid State Chem. 182 (2009) 669–676.
[4] A.J. Kenyon, Prog. Quant. Electron. 26 (2002) 225–228.
[5] F. Cansell, C. Aymonier, J. Supercrit. Fluids 47 (2009) 508–516.
[6] A. Tarafder, A.R. Molla, B. Karmakar, J. Am. Ceram. Soc. 93 (2010) 3244–3325.
[7] A. Tarafder, A.R. Molla, B. Karmakar, Solid State Sci. 12 (2010) 1756–1763.
[8] P. Vomacka, J. Eur. Ceram. Soc. 17 (1997) 615–621.
[9] P. Vomacka, B. Babushkin, J. Eur. Ceram. Soc. 15 (1995) 921–928.
[10] P. Vomacka, R. Ramesh, S. Hampshire, J. Eur. Ceram. Soc. 16 (1996) 1253–1262.
[11] P. Vomacka, B. Babushkin, R. Warren, J. Eur. Ceram. Soc. 15 (1995) 1111–1117.
[12] P. Vomacka, D.S. Wilkinsod, J. Eur. Ceram. Soc. 16 (1996) 1245–1251.
[13] D. Hülsenberg, A. Harnisch, A. Bismarck, Microstructuring of Glasses, Springer Series in Materials Science, Berlin, Heidelberg, New York, 2008, pp. 20–27.
[14] V. Maier, G. Müller, J. Am. Ceram. Soc. 70 (1987) C176–C178.
[15] S. Bhattacharyya, T. Höche, Cryst. Growth Des. 10 (2009) 379–385.
[16] T. Höche, M. Mäder, S. Bhattacharyya, G.S. Henderson, T. Gemming, R. Wurth, C. Rüssel, I. Avramov, Cryst. Eng. Commun. 13 (2011) 2550–2556.
[17] L. Cormier, O. Dargaud, N. Menguy, G.S. Henderson, M. Guignard, N. Trcera, B. Watts, Cryst. Growth Des. 11 (2010) 311–319.
[18] C. Bocker, F. Muñoz, A. Durán, C.J. Rüssel, Solid State Chem. 184 (2011) 405–410.
[19] M. Środa, Z. Olejniczak, J. Non-Cryst. Solids 357 (2011) 1696–1700.
[20] F. Muñoz, A. Pablos-Martín, N. Hémono, M.J. Pascual, A. Durán, J. Non-Cryst. Solids 357 (2011) 1463–1468.
[21] C. Liu, J.V. Hong, J. Heo, J. Non-Cryst. Solids 351 (2005) 2317–2323.
[22] C. Rüssel, Chem. Mater. 17 (2005) 5843–5847.
[23] C. Bocker, C. Rüssel, J. Eur. Ceram. Soc. 29 (2009) 1221–1225.
[24] R.P.F. De Almeida, C. Bocker, C. Rüssel, Chem. Mater. 20 (2008) 5916–5921.
[25] J. Zarzycki, Glasses and the Vitreous State, Cambridge University Press, Cambridge, UK, 1991.
[26] J. Lucas, J. Mater. Sci. 24 (1989) 1–13.
[27] G. Lengward, M.H. Lewis, Mater. Sci. Eng. 71 (1985) 101–111.
[28] H. Yang, Y.S. Kim, J. Luminesc. 128 (2008) 1570–1576.
[29] V. Pankratov, L. Grigorjeva, D. Millers, T. Chudoba, Radiat. Meas. 42 (2007) 679–682.

5.2

A. Keshavarzi, W. Wisniewski and C. Rüssel

Dendritic Growth of Yttrium Aluminum Garnet from an Oxide Melt in the System SiO$_2$/Al$_2$O$_3$/Y$_2$O$_3$/CaO

PAPER

Dendritic growth of yttrium aluminum garnet from an oxide melt in the system $SiO_2/Al_2O_3/Y_2O_3/CaO$

Ashkan Keshavarzi, Wolfgang Wisniewski* and Christian Rüssel

Glasses with the compositions x CaO·1CeF$_3$ $(11-0.2x)$ Y$_2$O$_3$·$(49.2-0.8x)$ Al$_2$O$_3$·28.8 SiO$_2$ (with $x =$ 10, 20, 30 and 40) were thermally annealed at 1200 °C for 6 h. This led to the crystallization of yttrium aluminium garnet (YAG) as the only occurring phase. The crystals formed dendrites instead of monolithic bodies with large quantities of glassy phase between the dendrite arms. Large, cube shaped crystals occurred in the samples with the highest and the lowest calcium concentration (10 and 40 mol%). Interpenetrating dendrites were detected in samples with calcium concentrations of 20 and 30 mol% using electron backscatter diffraction (EBSD). The glass-ceramics show intense fluorescence due to Ce^{3+} and might be suitable for lighting technology to convert the blue light of light emitting diodes to white light.

Introduction

The formation of patterns and morphologies during dendritic growth has remained a central topic and source of fascination in solidification research.[1–3] Examples are many, from the casting of aerospace alloys to the growth of transition metal oxide thin films used for solar cells. Dendritic growth is also sometimes observed when glass is crystallized.[4] Here, the microstructure is strongly affected by the glass composition, the conditions supplied during the nucleation process and during crystal growth, meaning it is controlled by the thermal annealing procedure. Dendritic crystal growth inside an amorphous material, *i.e.* inside a glassy matrix, is an attractive research field as growth mechanisms have been investigated in order to understand the kinetics, thermodynamic principles and the (an)isotropy of the respective materials, not only on earth, but even in the low gravity environment (μg) of space.[5,6]

The growth directions of dendrites are closely related to the underlying crystal symmetry.[7] In recent years, it has been found that dendrite growth directions are not limited to a discrete set of crystallographic directions, but within certain limits may vary continuously.[8] Significant progress has been made on the determination of dendritic crystal structures. For example, Haxhimali has demonstrated that the primary dendrite growth directions can vary continuously between different crystallographic directions as a function of the composition-dependent anisotropy parameter.[8–10] Further progress has been made towards understanding the transport mechanisms near the dendrite tips which control the stability of the tip shape and specify the tip radius and initial secondary spacing.[11] In most cases, the formation of dendritic crystals involves two different

processes: the first is the steady-state propagation near the tip region, which can be described by the classical theory of diffusion-limited dendritic growth,[11] and the second is the time-dependence of the secondary and tertiary side branches.[11]

If glass-ceramics are prepared from an isotropic material, *i.e.* an isotropic glass, crystal growth is a result of homogeneous or heterogeneous nucleation and will usually lead to isotropic glass-ceramics if nucleation occurs throughout the entire volume. Hence, an anisotropic structure can only be the result of suitable driving forces.[12–14] Three general routes may be followed in order to prepare oriented glass-ceramics:[12] the mechanical deformation of the melt (*e.g.* extrusion or fiber drawing) and thermodynamic as well as kinetic control. Among these methods, the kinetic control is still the most versatile and most frequently applied method to control the crystallization process during solidification of supercooled materials. Here, nucleation takes place in only a small part of the volume, for example at or near the surface.

Yttrium aluminum garnet (YAG, Y$_3$Al$_5$O$_{12}$) materials have been studied extensively because of their exceptional high-temperature mechanical strength coupled with low creep. Furthermore, its utility as phosphors in solid-state lighting and light emitting diodes (LEDs) has recently gained interest.[15,16] Normally, white LEDs are obtained by combining blue LEDs with yellow-emitting Y$_3$Al$_5$O$_{12}$:Ce^{3+} phosphors. Currently YAG powders embedded in polymers, usually a polysiloxane, are mostly used for that purpose. A serious drawback of this method is the relatively poor thermal conductivity of polymers, which prevents an effective removal of the heat generated in the phosphor and significantly limits the maximum possible light intensity of the LEDs. Especially for high power applications it would hence be highly advantageous if the YAG crystals were directly incorporated into a matrix of higher thermal conductivity

Otto-Schott-Institut, Jena University, Fraunhoferstr. 6, 07743, Jena, Germany. E-mail: wolfgang.w@uni-jena.de

Table 1 Studied glass compositions and glass transition temperatures

Sample Composition	SiO$_2$	Al$_2$O$_3$	Y$_2$O$_3$	CeF$_3$	CaO	T_g in °C
A	28.8	49.2	11	1	10	820
B	28.8	41.2	9	1	20	795
C	28.8	33.2	7	1	30	770
D	28.8	25.2	5	1	40	730

and stability, making the crystallization of YAG from glasses an interesting possibility. Although many studies on YAG have been performed, relatively few reports on the crystallization of doped YAG from glasses have been published.[17–20] Especially the effect of the glass composition and the annealing conditions on the phase formation, crystal morphology and orientation of YAG crystals in glass-ceramics has hardly been investigated so far.

In this paper, four different glass compositions with different Y$_2$O$_3$ and Al$_2$O$_3$ concentrations are prepared and characterized with respect to phase formation and especially concerning the morphology of the prepared crystals. These studies are performed using X-ray diffraction (XRD), scanning electron microscopy (SEM), electron backscatter diffraction (EBSD) and fluorescence microscopy (FM).

Results and discussion

The prepared glasses were visually transparent and did not show any obvious light scattering. Thermally annealed samples were translucent and of a yellow colour. The glass transition temperatures T_g of the compositions range from 730 to 820 °C and decrease with increasing calcium concentrations, see Tab. 1.

Fig. 1 shows XRD-patterns of the glass and of samples annealed at 1200 °C for 6 h. While the glass does not show any distinct lines indicating a crystalline phase, the thermally annealed samples show intense peaks attributable to YAG (JCPDS-file no. 01-082-0575).

The glass-ceramics were characterized by SEM and optical fluorescence microscopy in order to evaluate the growth of the crystals and the resulting morphologies. SEM-micrographs of


Fig. 2 SEM-micrographs of the samples A, B, C, and D.

the studied samples are shown in Fig. 2 where the crystalline phase is brighter, indicating a higher mean atomic weight than the glass matrix. The morphology of these crystals indicates dendritic growth by the regular structures and side arms observed in the micrographs. While all the features are relatively large, the size of the crystalline structures in sample B exceeds the sizes observed in the other samples significantly.

The Fig. 3 to 6 show FM-micrographs providing a three dimensional impression of the microstructure which cannot be obtained by SEM. Fig. 3 presents a stitched overview of sample A where only one dendrite with a size of several mm is observed. The rectangular geometry and the regular crystal structures are similar to the morphologies observed in a fresnoite dendrite cut perpendicular to the c-axis of its unit cell.[4] EBSD-patterns were acquired at the positions 1–5 in Fig. 3 and will be presented in Fig. 7. Nucleation occurred at the centre, followed by crystal growth with approximately the same velocities in the main crystallographic directions. Notable quantities of glassy phase occur between the crystals.

Fig. 4 presents an FM-micrograph of sample B showing very regular structures. The inset illustrates one structure in greater detail and the 120°-angles between side arms observed in this cut plane.

In contrast to the samples A and B, the cut plane through sample C in Fig. 5 a) shows a highly aligned structure already

Fig. 1 XRD-patterns of a casted glass and of crystallized samples.
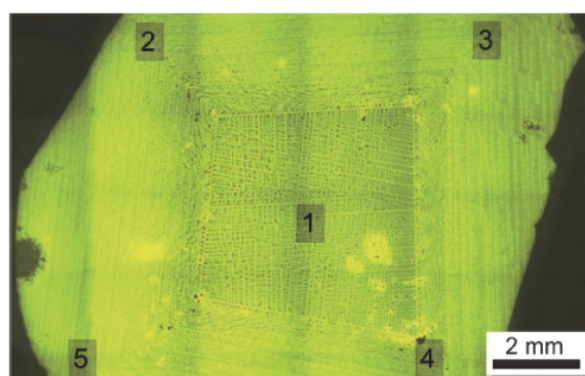
Fig. 3 Fluorescence microscopy micrograph of sample A. EBSD-patterns were obtained at the locations 1–5 and are presented in Fig. 7.
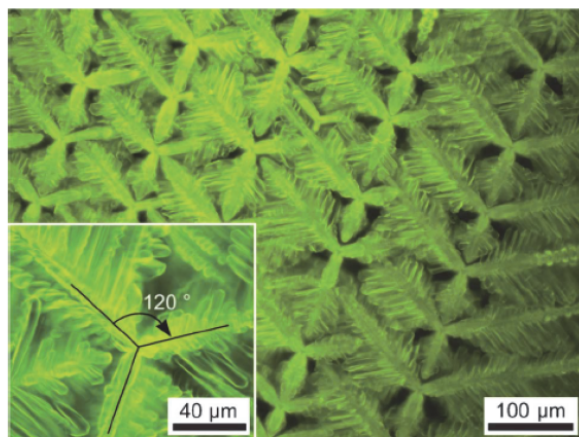
Fig. 4 Fluorescence microscopy micrographs of sample B.

indicated in Fig. 2. While Fig. 5 b) shows the growth structures with a higher magnification, Fig. 5 c) focuses on the tip of a side arm where a 90°-angle frequently observed in dendrite tips of cubic crystals [11] is observed.

Fig. 6 presents one of several independent dendritic crystals grown in sample D which largely remained glassy after annealing. The cubic symmetry of the YAG is mirrored by the shape of the crystal. While the central bright triangle indicates the cut plane which traverses one corner, most of the cube is positioned below the sample surface. The faces of the cube are concave, indicating crystal growth occurs somewhat faster at edges and tips in comparison to the even planes supposedly due to three-dimensional diffusion.

EBSD-analyses were performed in order to determine crystallographic orientations in the samples and search for dendritic fragmentation.[21] A material file was built based on ICSD-file no. 74607 and used for all indexing purposes. Fig. 7 presents a SEM-micrograph of the surface superimposed by the orientation+IQ-map of a detailed EBSD-scan performed on the area. Orientation maps are used to highlight one or more specific crystal orientations with defined tolerances, *e.g.* in order to visualize slight orientation deviations. The combination with the
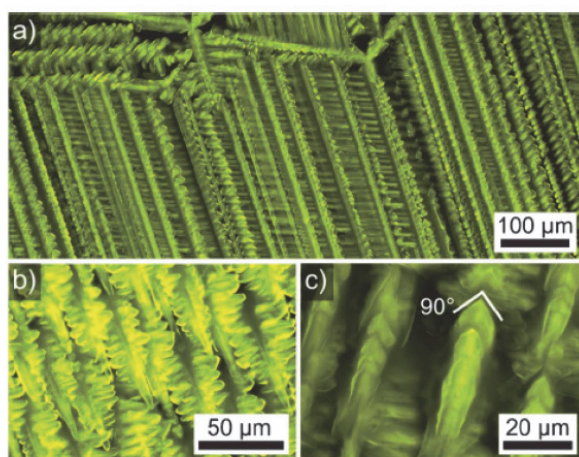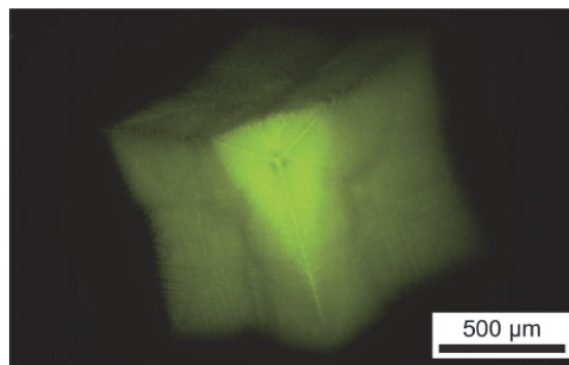

Fig. 6 Fluorescence microscopy micrograph of a YAG cube in sample D. The bright triangle represents the cut plane.

grayscale Image Quality-map (IQ-map) enables to locate areas of reduced EBSD-pattern quality which appear darker, *e.g.* grain boundaries or residual glass. The orientation+IQ-map of a larger scan is also presented along with the EBSD-patterns acquired at the locations marked as 1–5 in Fig. 3 and unit cells visualizing the respective crystal orientations.

While the orientation maps indicate a very homogeneous orientation of the YAG-dendrite, which is oriented with a (100)-plane tilted by 5° from the surface normal (Euler Angle $\Phi = 5°$), the unit cells of the EBSD-patterns acquired at the extremities of the dendrite show that slight orientational changes occur over longer distances of growth. While the (001)-plane of the central pattern 1 is almost parallel to the sample surface, the (001)-planes of the patterns 2–5 are slightly tilted towards the centre of the sample. This indicates that the faster growth velocities at the

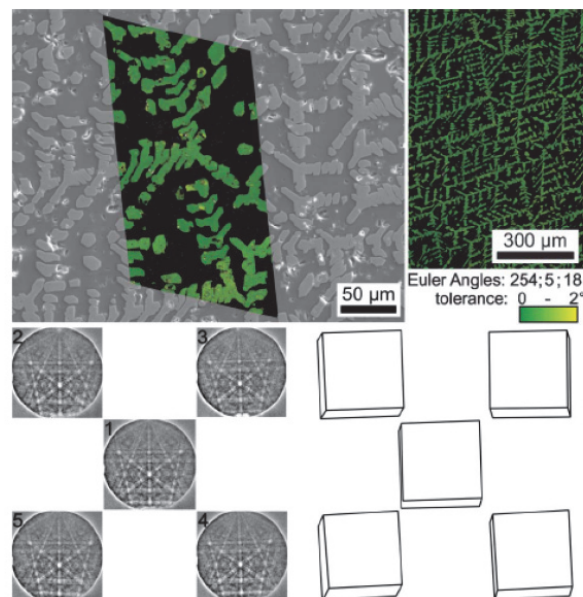Fig. 5 Fluorescence microscopy micrographs of sample C.

Fig. 7 SEM-micrograph of the centre of sample A superimposed by the orientation+IQ-map of an EBSD-scan performed on the area. A larger orientation+IQ-map is also presented along with the EBSD-patterns obtained at the locations 1–5 in Fig. 3. Wireframes illustrate the orientations determined from these patterns.
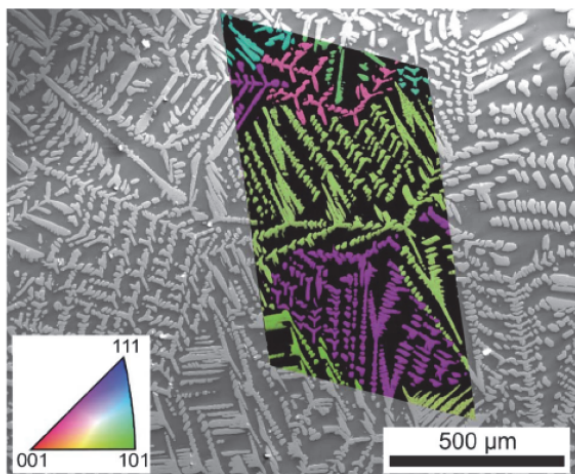
Fig. 8 SEM micrograph superimposed by an IPF+IQ-map of an EBSD-scan performed on sample B.

edges and tips of the growing dendrite indicated in Fig. 6 are probably accompanied by a low degree of orientational change. Dendritic fragmentation is not observed in the EBSD-scans of Fig. 7, nor was it observed in any EBSD-scan performed on the samples presented in this paper.

Fig. 8 presents an SEM-micrograph of sample B superimposed by the Inverse Pole Figure+IQ-map (IPF+IQ-map) of an EBSD-scan, where every crystal orientation is attributed to one colour in the corresponding IPF-legend. In contrast to sample A, numerous dendrites of different orientations are observed in this sample, pointing towards a higher nucleation rate. This is also valid for sample C. In sample D, the independent dendrites also show various orientations, but did not hinder each other during growth as they never collided during the annealing time.

The presented results show that the crystallization of YAG was achieved in every sample, although nucleation rates were very different. Dendritic growth is observed in all the samples, leading to homogeneously oriented areas of crystallization which may fill the entire sample. Dendritic fragmentation is not observed. The 120°-angle observed in the microstructure of Fig. 4 is also found in the macroscopic cube featured in Fig. 6 and is typical for a cubic body with a [111]-direction perpendicular to the cut plane.

The microstructure of sample A shown in Fig. 3 and the corresponding orientation measurements presented in Fig. 7 indicate that a single dendritic structure was formed in this sample. While crystal orientations are extremely homogeneous, growth over large distances, i.e. several mm, leads to the slight changes described by the unit cells in Fig. 7. The rectangular morphology in Fig. 3 roughly matches the expectations towards the unhindered growth of a cubic phase. This sample contained only 10 mol% of CaO and obviously showed a very low nucleation rate compared to the crystal growth velocity.

A CaO concentration of 20 mol% or higher raises the nucleation rate, leading to multiple dendrites of various orientations as observed in the samples B to D and shown in Fig. 8. However, a CaO-concentration of 40 mol% led to the formation of only three independent crystals in the sample, one of which is presented in

Fig. 6, indicating the nucleation rate is reduced by a too high CaO concentration. Additionally, the crystals are comparably small, leaving much of the sample uncrystallized and pointing towards a significantly reduced growth velocity. It must be noted that a single nucleus allowed the crystallization of the entire sample A under the same annealing conditions.

It can be concluded that the influence of the CaO-concentration on the crystal growth velocity is much higher than the lower T_g of the corresponding glass, which should have increased the growth velocity. With an increase of the CaO concentration, the percentage of YAG-forming elements is reduced, leading to long diffusion paths and hence lower growth velocities.

The cubic shape of the dendrite in Fig. 6 indicates comparable growth velocities in all {100}-directions. The {100}-faces of the cube are slightly concave, indicating growth is slightly faster at the edges and indicating a 3D-diffusion problem limiting the growth velocity, i.e. the tips and edges of the cube feed from a larger volume of glass than the planar faces. The growth at the latter is achieved by one dimensional diffusion, while three-dimensional diffusion occurs at the edges. Although these differences seem to be fairly small, they give evidence that crystal growth, at least at the planar faces, is limited by diffusion. These comparatively small differences in the growth velocities may eventually also lead to the slight orientational changes indicated in Fig. 7 via an accumulation of stacking faults during growth because slightly deviating arms are not blocked by neighbours if they are located at the edges of a cube.

By contrast, notably higher nucleation rates have been observed in glasses with the composition 1 CeF$_3$·34.1 Al$_2$O$_3$·4.8 AlF$_3$·20 Y$_2$O$_3$·40 SiO$_2$ [17] and in compositions with 5 mol% of SiO$_2$ replaced by TiO$_2$, ZrO$_2$ or a mixture of both.[17] Crystallization of these glasses mostly led to large YAG-crystals of polygonal shape some 10 μm in size [17] and additionally minor concentrations of other phases such as zirconia, yttria, Y$_2$Si$_2$O$_7$ or rutile.[17] In these CaO-free compositions, dendritic growth was not the main growth mechanism, although it was also observed in some compositions.[17]

In the work presented here, CaO concentrations of 10 to 40 mol% were used. In principle, CaO might be incorporated into the glass as network modifier, i.e. to generate non-bridging oxygens, or it might also be incorporated as a charge compensator for negatively charged AlO$_4$$^-$-tetrahedra. An analysis of the Si–O bond lengths for non-bridging and bridging oxygens[22] showed that modifier cations, such as Ca^{2+} are further coordinated by bridging oxygen-atoms. Furthermore, the bond angle distributions illustrate that the coordination polyhedron for Ca^{2+} is most likely a reasonably regular octahedron. A fairly similar description has also been done by Eckersley et al.[23]

According to the classification of the glass components given by Dietzel,[24] alumina should mainly act as network former in the studied compositions, while Ca^{2+} either acts as a network modifier or is incorporated to compensate the formally negative charge of the AlO$_4$$^-$-tetrahedra. The cationic field strength of Y^{3+} is somewhat larger than that of Ca^{2+}. Nevertheless it should predominantly be incorporated in a similar way as Ca^{2+}, i.e. either generate the formation of non-bridging oxygen, or, however, compensate the charge of AlO$_4$$^-$-tetrahedra.

In the glass with the composition A, 11 mol% Y$_2$O$_3$, 0.5 mol% Ce$_2$O$_3$ (1 mol% CeF$_3$) and 10 mol% CaO may compensate the

charge of 27.25 mol% Al_2O_3 ($(11 \times 3 + 0.5 \times 3 + 10 \times 2)/2$) present. Hence 27.25 mol% Al_2O_3 should be incorporated as AlO_4^--tetrahedra. The excess Al_2O_3 (21.95 mol% Al_2O_3) is then incorporated in octahedral coordination or as triclusters. In the glass composition B, 9 mol% Y_2O_3, 0.5 mol% Ce_2O_3 and 20 mol% CaO may compensate the negative charge of 34.25 mol% Al_2O_3. The remaining 6.95 mol% Al_2O_3 should be incorporated in octahedral coordination or as triclusters. The glass composition C contains 33.2 mol% Al_2O_3; which are incorporated in tetrahedral coordination. The 7 mol% Y_2O_3, 0.5 mol% Ce_2O_3 and 30 mol% CaO additionally give rise to the formation of 16.1 mol% non-bridging oxygen. In the glass composition D, the CaO concentration is as large as 40 mol%. The entire Al_2O_3 is incorporated in tetragonal coordination and the excess Y_2O_3, Al_2O_3 and Ce_2O_3 lead to the formation of 46.1 mol% non-bridging oxygen.

The glasses B and C do not contain large quantities of non-bridging oxygens. By contrast, glass D contains large quantities of non-bridging oxygen which also gives rise to the lowest glass transition temperature of the studied glasses. In this glass only few nuclei were formed, the nucleation rate is hence small and the crystals are very large and show dendritic morphology. In this glass, the applied annealing temperature was 470 °C above T_g, which might result in large crystal growth velocities. In the glasses B and C, T_g was higher than in glass D and hence, the difference of the annealing and the glass transition temperature were not as high (405 and 430 °C, respectively). Nucleation rates usually exhibit a maximum some 10 K above T_g in glass forming liquids while the crystal growth velocities have their maximum some 10 K below the liquidus temperature. This should result in higher nucleation rates in comparison to the crystal growth velocities which easily explain the interpenetrating dendrites observed in these glasses.

Glass A shows a large quantity of alumina which cannot be incorporated as AlO_4^--tetrahedra because compounds which might compensate their charges are not available. Since this glass shows the highest glass transition temperature (820 °C), the excess alumina does not give rise to an increased network mobility. The annealing temperature is 380 K above the glass transition temperature. In analogy to Glass D, alumina does not predominantly occur as AlO_4^--tetraedra, which might be the reason for the low nucleation rate observed. In the YAG crystal, one third of the alumina occurs in tetrahedral and two thirds in octahedral coordination. The coordination in the crystal and in the glass where the crystal is precipitated does not necessarily have to be the same, *i.e.* it may also change during nucleation. In the compositions presented here, the nucleation rate is not higher in the compositions which show similar concentrations of aluminium in tetrahedral and in octahedral concentrations.

The YAG crystals obviously incorporate Ce^{3+}, which gives rise to intense fluorescence as shown in Fig. 3 to 7. Despite of the high concentration of crystalline phase in the glass-ceramics, they are translucent and hence might be suitable as conversion materials in lighting technology to transfer the light of LEDs to white light.

Experimental

Glasses with the compositions x $CaO \cdot 1CeF_3$ $(11-0.2x)$ $Y_2O_3 \cdot (49.2-0.8x)$ $Al_2O_3 \cdot 28.8$ SiO_2 (with $x = 10, 20, 30$ and 40) were melted from the raw materials CeF_3, $Al(OH)_3$, $CaCO_3$, Y_2O_3 and SiO_2 in a platinum–rhodium crucible using an electric furnace heated to 1590 °C for 3 h. The chemical compositions of the samples are summarized in Table 1; the calcium oxide concentration was varied from 10 to 40 mol%, while the CeF_3 and the SiO_2 concentrations were kept constant. After stirring the melt for 2 h, it was cast on a copper block, quenched with a copper stamp and transferred to a furnace preheated to 770 °C. The furnace was subsequently cooled using a rate of 5 K min^{-1}. In order to eliminate any surface effects from the quenching procedure, a few mm of the glass samples were removed followed by manually polishing the surfaces with decreasing grain sizes down to 0.75 μm diamond suspension. To crystallize the glass, polished samples were transferred to a furnace preheated to 770 °C and subsequently heated to 1200 °C using a rate of 10 K min^{-1}. This temperature was kept for 6 h; finally, the furnace was switched off, allowing the samples to cool with a rate of approximately 3 K min^{-1}.

The solid samples were directly analyzed by XRD (Siemens D5000) using $Cu_{K\alpha}$-radiation. Fluorescence optical micrographs (FM) were obtained *via* laser scanning microscopy (LSM) using an Axio Imager Z1M LSM5- Pascal (Carl Zeiss AG, Oberkochen, Germany).

The samples were further characterized using an SEM Jeol JSM-7001F equipped with an analyzing system EDAX Trident. EBSD-scans were recorded and evaluated using a TSL Digiview 1913 EBSD-Camera and the software TSL OIM Data Collection 5.31 and TSL OIM Analysis 5. Samples polished for EBSD-analysis received a final finish of at least 30 min using colloidal silica. In order to achieve a conductive surface, the samples were mounted using an Ag-paste and coated with a thin layer of carbon at about 10^{-3} Pa.

Conclusion

In the studied yttria alumina silicate glasses with CaO-concentrations from 10–40 mol% annealing at 1200 °C led to the crystallization of yttrium aluminum garnet as the only crystalline phase. Crystal growth occurred in the form of large dendrites with significant quantities of residual glass between dendritic arms. Dendritic fragmentation was not observed. While samples with 20 and 30 mol% CaO were composed of many dendrites, samples with 10 and 40 mol% contained only very few dendrites, indicating a significant effect of CaO on the nucleation rate and crystal growth velocity in the glasses. The produced glass-ceramics might be suitable as conversion materials in lighting technology to convert the blue light of LEDs to white light.

Acknowledgements

References

1 W. A. Tiller, *Science*, 1964, **146**, 871–879.
2 L. Granasy, T. Pusztai, T. Borzsonyi, J. A. Warren and J. F. Douglas, *Nat. Mater.*, 2004, 3, 645–650.

3 J. Warren, *Nat. Mater.*, 2006, **5**, 595–596.
4 W. Wisniewski, M. Nagel, G. Völksch and C. Rüssel, *Cryst. Growth Des.*, 2010, **10**, 1939–1945.
5 N. Bergeon, R. Trivedi, B. Billia, B. Echebarria, A. Karma, S. Liu, C. Weiss and N. Mangelinck, *Adv. Space Res.*, 2005, **36**, 80–85.
6 M. E. Glicksman, M. B. Koss, L. T. Bushnell, J. C. LaCombe and E. A. Winsa, *Adv. Space Res.*, 1991, **11**, 53–57.
7 K. A. Jackson in *Kinetic Processes – Crystal Growth, Diffusion, and Phase Transitions in Materials*, Wiley-VCH, 2004.
8 T. Haxhimali, A. Karma, F. Gonzales and M. Rappaz, *Nat. Mater.*, 2006, **5**, 660–664.
9 K. Nagashio and K. Kuribayashi, *Acta Mater.*, 2005, **53**, 3021–3029.
10 E. Ben-Jacob and P. Garik, *Nature*, 1990, **343**, 523–530.
11 G. Müller, J.–J. Métois and P. Rudolph in *Crystal Growth – From Fundamentals to Technology*, Elsevier, 2004.
12 C. Rüssel, *J. Non-Cryst. Solids*, 1997, **219**, 212–218.
13 R. Keding and C. Rüssel, *J. Mater. Sci.*, 2004, **39**, 1433–1435.
14 D. I. H. Atkinson and P. W. McMillan, *J. Mater. Sci.*, 1976, **11**, 443–450.
15 E. Jang, S. Jun, H. Jang, J. Lim, B. Kim and Y. Kim, *Adv. Mater.*, 2010, **22**, 3076–3080.
16 T. S. Troutman, S. J. Leung and M. Romanowski, *Adv. Mater.*, 2009, **21**, 2334–2338.
17 A. Keshavarzi and C. Rüssel, *Mater. Chem. Phys.*, 2012, **132**, 278–283.
18 S. Alahraché, M. Deschamps, J. Lambert, M. R. Suchomel, D. S. Meneses, G. Matzen, D. Massiot, E. Véron and M. J. Allix, *J. Phys. Chem. C*, 2011, **115**, 20499–20506.
19 G. He, L. Mei, L. Wang, J. Liu and J. Li, *Cryst. Growth Des.*, 2011, **11**, 5355–5361.
20 S. Fujita, Y. Umayahara and S. J. Tanabe, *J. Ceram. Soc. Jpn.*, 2010, **118**, 128–131.
21 M. Rettenmayr, *Int. Mater. Rev.*, 2009, **54**, 1–17.
22 A. N. Cormack and J. C. Du, *J. Non-Cryst. Solids*, 2001, **293–295**, 283–289.
23 M. C. Eckersley, P. H. Gaskell, A. C. Barnes and P. Chieux, *Nature*, 1988, **335**, 525–527.
24 H. Scholze in *Glas – Natur, Struktur und Eigenschaften*, Springer, 1988.

5.3

A. Keshavarzi, W. Wisniewski, R. de Kloe and C. Rüssel

Surface Crystallisation of Yttrium Aluminum Garnet from a Silicate Glass

Surface crystallisation of yttrium aluminum garnet from a silicate glass

Ashkan Keshavarzi,[a] Wolfgang Wisniewski,*[a] René de Kloe[b] and Christian Rüssel[a]

Glasses with the mol% composition $17Y_2O_3 \cdot 33Al_2O_3 \cdot 40SiO_2 \cdot 2AlF_3 \cdot 3Na_2O \cdot 2CeF_3 \cdot 3B_2O_3$ were thermally annealed at 1000 °C for different periods of time. This resulted in the surface nucleation and subsequent growth of Ce^{3+}-doped yttrium aluminium garnet (YAG) which shows an intense broadband fluorescence. In the bulk, the nucleation and subsequent growth of an X-ray amorphous star-shaped and alumina enriched phase leads to a depletion of alumina from the glass. The nucleation of monoclinic and orthorhombic $Y_2Si_2O_7$ adjacent to the YAG layer is observed in addition to pore formation. These pores serve as centres for enhanced nucleation near the surface. The nucleation and growth of the orthorhombic phase and a different monoclinic $Y_2Si_2O_7$ are additionally observed in the bulk. The phase identification and localization was performed by X-ray diffraction and electron backscatter diffraction (EBSD).

Introduction

Glasses show a very diverse behaviour with respect to crystallization mechanisms. Some glass compositions solely exhibit surface crystallization[1–3] while other glasses show only bulk crystallization.[4,5] It has been known for decades that the addition of specific components to a glass may switch the mechanism from surface to bulk nucleation. These so called "nucleating agents" lead to the precipitation of a crystalline phase in the bulk which subsequently triggers the crystallization of another crystalline phase. Among the components which were reported to trigger bulk crystallization are *e.g.* noble metals (typically platinum in concentrations <0.1%), titania or zirconia. For example, glasses in the system MgO–Al_2O_3–SiO_2 usually show surface crystallization *e.g.* of cordierite, mullite or quartz. The addition of >4% titania or zirconia to these glasses, however, leads to crystallization in the bulk.[6] It should be noted that certain components may also act as nucleation inhibitors in some glass compositions. For example, adding zirconia to a borosilicate glass has led to a decrease in the nucleation rate.[7,8] Usually, the crystalline phases formed during surface crystallization and during bulk nucleation after adding nucleating agents are the same.

Literature describing glass-ceramics with a structure composed by a surface layer exhibiting one crystalline phase and the bulk showing another crystalline phase is not known to the authors. Such materials may be highly advantageous for many purposes. Multi phase materials could exhibit high strengths due to stresses caused by different coefficients of thermal expansion (CTEs) and show additional functions caused by one of the crystalline phases.

As crystalline phases are usually denser than an amorphous phase of the same composition, stresses frequently arise during crystallization itself. Additionally, materials formed at high temperatures and containing more than one phase usually exhibit different CTEs. This leads to the additional formation of stresses during cooling. In the case of glass-ceramics in the system MgO–Al_2O_3–SiO_2–TiO_2, small inclusions of quartz are formed which show a phase transition from the high temperature to the low temperature modification between 500 and 570 °C. This runs parallel to a volume contraction of 0.7% which leads to stresses that result in a drastic increase in the mechanical strength (*e.g.* from 150 to 400 MPa).[9,10] The mechanical strength may also be notably increased by crystallizing phases with low CTEs such as eucryptite from the surface after an ion exchange treatment.[11] This is caused by compressive stresses in a surface layer with lower CTEs.

Glass-ceramics containing yttrium aluminium garnet (YAG) are interesting materials for lighting technology because Ce^{3+}-doped garnet is advantageous for the conversion of blue light from light emitting diodes (LEDs) to white light.[12] Currently such devices are predominantly produced by embedding doped garnet powders in polymers such as polysiloxanes. High power applications cannot be realized using this concept due to the poor thermal conductivity of the polymers and their low thermal stability. One possibility to overcome this problem is the utilization of glass-ceramics containing garnet crystals. Unfortunately, these glass-ceramics are scarcely described in the literature and difficult to produce. While there are some

[a] Otto-Schott-Institut, Jena University, Fraunhoferstr. 6, 07743 Jena, Germany.
E-mail: wolfgang.w@uni-jena.de
[b] EDAX BV, 5004JC Tilburg, Netherlands

reports in the literature on spontaneous crystallization of yttrium aluminium garnet during the cooling of a melt, the controlled crystallization of yttrium aluminium garnet from glasses has only recently been described in the literature.[12–15] The growth kinetics of the crystals are affected by the diffusion of components from the glassy matrix to the interface crystal–glass and *vice versa*.[16–18] Chemical variations may significantly change the growth mechanisms of YAG in glass[13,14] as well as nucleation rates.[13]

This article features a glass in which a surface layer of YAG is formed during thermal annealing and an Al-rich phase is precipitated throughout the bulk in a first step. Three yttrium silicate phases subsequently crystallize. Electron microscopy and optical microscopy are extensively used to analyze the microstructures formed by nucleation and crystal growth.

Experimental procedure

Glasses with the mol% composition $17Y_2O_3 \cdot 33Al_2O_3 \cdot 40SiO_2 \cdot 2AlF_3 \cdot 3Na_2O \cdot 2CeF_3 \cdot 3B_2O_3$ were prepared from pure reagent grade raw materials. Fluorine was added to the composition to lower the glass viscosity[19] and hence enhance crystallization. They were melted in 100 g batches in a platinum–rhodium crucible using an electric furnace heated to 1590 °C for 3 h. During the melting process, the melt was stirred manually from time to time using a platinum rod to homogenize the melt. The melt was cast on a copper block, quenched with a copper stamp and transferred to a furnace preheated to 850 °C and subsequently cooled using a rate of 4 K min^{-1}.

The glass samples were cut, ground and polished. In order to crystallize the glass, polished samples were transferred to a furnace and subsequently annealed at a temperature of 1000 °C using a heating rate of 10 K min^{-1}. To remove any dust and grinding media and prevent impurity induced surface crystallization, the polished samples were rinsed with ethanol and deionised water before annealing them in covered alumina containers. The annealing temperature was kept for 3, 6, 12 and 24 h before the samples were cooled to 830 °C using a rate of 4 K min^{-1}. The furnace was finally switched off, allowing the samples to cool to room temperature.

Glasses and annealed samples were characterized by X-ray diffraction (Siemens D5000) using Cu Kα radiation in the θ-2-θ-setup. Differential Thermal Analyses (Shimadzu DTA50) was carried out in air using Al_2O_3 powder as a reference standard and heating with a rate of 5 K min^{-1} from room temperature to 1400 °C. Dilatometric measurements (Netzsch DIL 402 PC) were also performed using a heating rate of 5 K min^{-1}. The density of the glass was measured using a helium-pycnometer (AccuPyc 1330).

Fluorescence optical micrographs (FM) were obtained *via* laser scanning microscopy (LSM) using a Carl Zeiss Axio Imager Z1M LSM5-Pascal. Electron microscopy was performed using a Jeol JSM-7001F scanning electron microscope (SEM) equipped with an EDAX Trident analyzing system containing a

TSL Digiview 3 EBSD-camera. Samples were mounted using Ag-paste and coated with a thin layer of carbon at about 10^{-3} Pa to achieve a conductive surface. Degrees of crystallization were calculated from SEM-micrographs using the software AxioVision40x64V4.8.3.0. EBSD-scans were collected and evaluated using the programs TSL OIM Data Collection 5.31 and TSL OIM Analysis 5.31. The scans were performed using a current of about 2.40 nA (measured with a Faraday cup) and a voltage of 20 kV.

Results and discussion

The casted glass was yellow, optically transparent and X-ray amorphous. The glass transition temperature T_g determined by dilatometry was 845 °C and an exothermic crystallization peak in the DTA-profile was obtained at 950 °C. Samples annealed at 1000 °C (155 K above T_g) for 3 h were translucent while annealing for 24 h at the same temperature resulted in opaque samples.

The SEM-micrographs in Fig. 1 show the unpolished surface of a sample annealed for 3 h. Fig. 1a) shows the surface is completely covered by structures of less than 10 μm in diameter and pores (black) are frequently observed. The higher magnification of Fig. 1b) enables to discern two morphologies: large, somewhat square structures implying dendritic growth and smaller, more diffuse structures. EBSD-pattern acquisition could not be achieved from these unpolished surfaces, making local orientation analysis or phase localization impossible. Apart from sample preparation and crystal instability there are two sample based factors that may prevent EBSD-pattern formation: i) a high density of lattice defects proposed as an explanation for the local inability to obtain patterns from diopside pyramids after surface crystallization,[3] and ii) a glass layer due to nucleation beneath the immediate surface as *e.g.* detected on surface crystallized cordierite.[20] As not even very weak patterns could be obtained, a superposition of both effects is thinkable. There are, however, many factors that may prevent EBSD-pattern
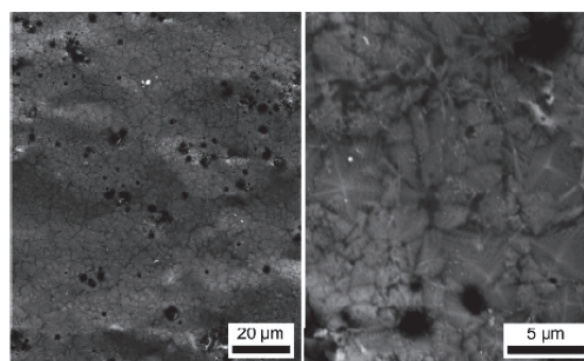

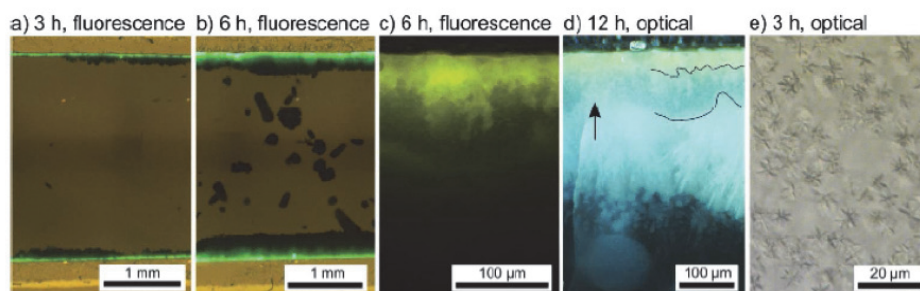**Fig. 1** SEM-micrographs of the crystallized surface.

Fig. 2 Fluorescence microscopy of samples annealed at 1000 °C for different periods of time. a) 3 h, b) 6 h, c) 6 h higher magnification and d) darkfield optical micrograph of the surface crystallization (12 h). e) Optical micrograph of the crystals in the bulk (3 h).

acquisition and it is impossible to draw reliable conclusions from the inability to obtain EBSD-patterns from these samples.

Fig. 2 shows images of the cross-sections of samples annealed for 3 to 12 h recorded using LSM. Fig. 2a)–c) present FM-images obtained by laser excitation using a wavelength of 460 nm. The emitted light with a wavelength of 530 nm (green) is typical for Ce^{3+}-doped YAG crystals,[14] indicating YAG at the sample surface. However, non-fluorescent crystals of dark appearance are observed below the YAG-layer. While these crystals are only observed near the YAG-crystals after annealing for 3 h, most dark structures in the bulk of Fig. 2b) clearly have no connection to the surface layer. Hence a YAG-independent nucleation occurs in the bulk after some time. Fig. 2c) presents the surface near area in a higher magnification, clearly localizing the fluorescence. If the laser is focused only on the darker area, fluorescence is not observed, proving that these crystals only scatter the light of the fluorescent crystals at the surface.

The dark field micrograph in Fig. 2d) actually enables to separate three different layers formed by surface crystallization in a sample annealed for 12 h; their borders are highlighted by superimposed lines. While the thickness of the first layer is relatively constant at about 30 μm, the second layer varies in thickness and may locally be very thin or not existent at all, see arrow. Correlation with Fig. 2c) indicates that the first layer shows luminescence, while the second and third do not. However, the question arises why strong luminescence may locally appear up to twice as far into the bulk than average; one possibility would be that YAG locally grows further into the bulk than expected. Fig. 2e) was obtained from the bulk of a sample annealed for 3 h and shows numerous star-shaped structures with a maximum diameter of about 6 μm. These structures are distributed throughout the sample but not observed in the topmost crystal layer. After 3 h, about 12% of the bulk is attributed to this phase assuming a somewhat homogeneous shape distribution.

These results indicate the presence of up to five crystalline phases in the samples; three of them in the context of surface crystallization and two resulting from bulk nucleation. Surface crystallization leads to three distinct layers: layer 1 is about 30 μm thick, fluorescent and probably Ce^{3+}-YAG. Layer 2 is

probably not continuous but reaches a thickness of up to 100 μm. The third layer probably also nucleates adjacent to layer 1 and possibly also in the bulk.

Fig. 3 presents experimental XRD-patterns a)–d) and the theoretical patterns of the phases used for indexing EBSD-patterns later on for comparison. Fig. 3a) shows an XRD pattern representative for unpowdered samples annealed at 1000 °C for 3–24 h. All high intensity peaks are attributable to YAG (JCPDS file 01-82-0575) and the peak intensities basically
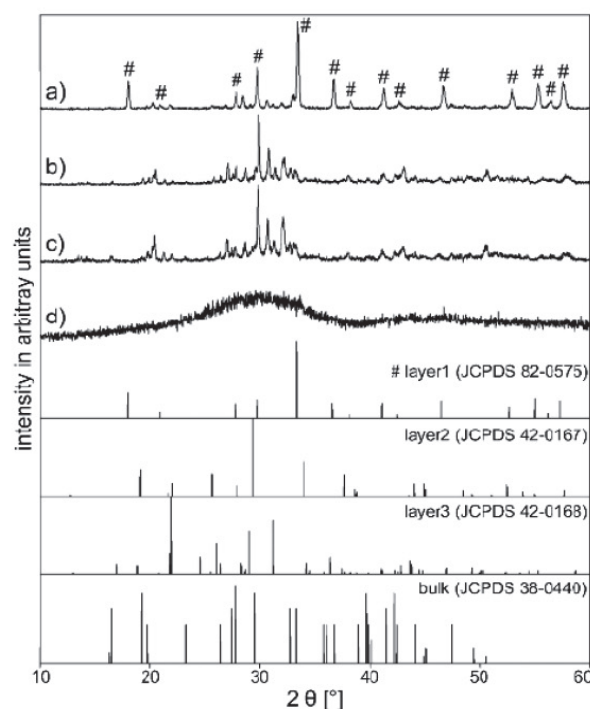

Fig. 3 XRD-patterns of samples annealed at 1000 °C: a) recorded directly from the surface of a sample annealed for 24 h. b) Recorded after the YAG-layer was removed from a sample annealed for 24 h. c) Recorded from a sample annealed for 24 h and powdered after YAG was removed. d) Recorded from a sample annealed for 3 h after YAG was removed. Theoretical patterns of the phases identified in these samples are presented below for comparison.

match those of the theoretical file, indicating a statistical orientation distribution. Pattern b) was obtained from a sample from which the yellow YAG-layer had been removed after annealing for 24 h. While some peaks match YAG-positions, a number of high intensity YAG-peaks including the 100%-peak at $2\theta = 33.26°$ are not observed, allowing the conclusion that YAG was completely removed and the peaks of pattern b) are caused by other phases. While most of the peaks in pattern b) may be attributed to one of the YS-patterns presented below, a clear phase identification is not possible as some relevant peaks are always absent. To check for textures resulting from a possibly incomplete removal of the surface crystallization zone, a comparable YAG-free sample was powdered and analyzed by XRD. The resulting pattern c) is basically the same as pattern b) and, while not contributing to phase identification, does prove that pattern b) is not texture affected. The final pattern d) does not show any diffraction peaks and was obtained after the YAG-layer had been removed from a sample annealed for only 3 h and hence only contains the star-shaped phase. Hence the star-shaped phase is either X-ray amorphous or fills less than about 0.5 ma% of the material. It will be shown below that some kind of crystal lattice is present as electron diffraction is possible. SEM-micrographs show that the star-shaped phase covers about 12% of a cut plane after 3 h and roughly 30% after 6 and 12 h. Of course a star-shaped structure may look much larger in a 2D-cut plane than the 3D-volume it actually occupies, see *e.g.* snowflakes, but the discrepancy to the 0.5 ma% detection threshold of XRD in the given setup is apparent. Hence the multiphase structure of the samples with a top layer of YAG is confirmed, but the XRD-results are very strange and inconclusive concerning the other phases in the system.

Fig. 4 visualizes the crystal development near the surface in greater detail *via* SEM micrographs of cross sections prepared from samples annealed for a) 3 h, b) 6 h and c) 24 h. In contrast to Fig. 2a), only two phases are observed after 3 h, indicating the nucleation adjacent to the YAG layer occurs over some time. The surface layer of YAG-crystals implies dendritic growth and the star-shaped phase is observed in all SEM-micrographs. Their dark appearance indicates a smaller mean
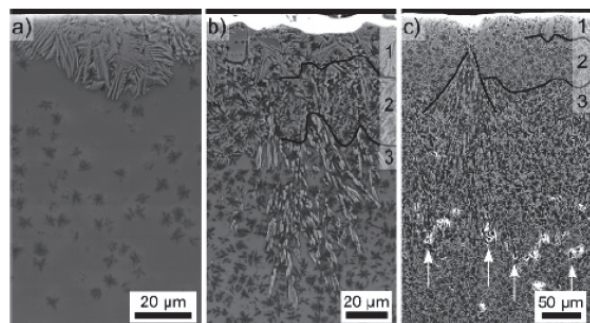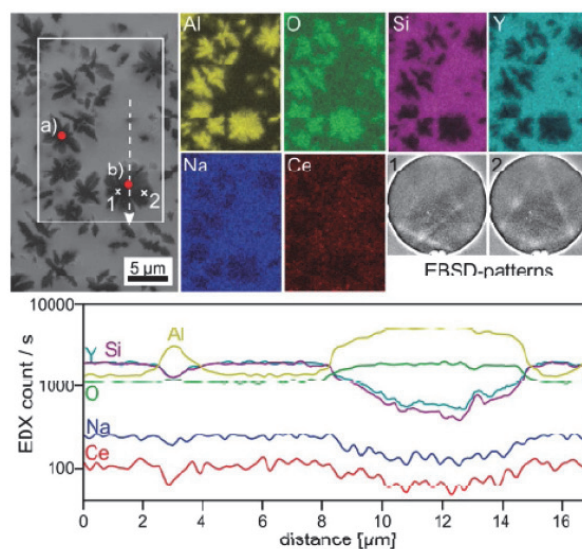

Fig. 5 SEM-micrograph and EDX element maps illustrating chemical differences between the star-shaped crystals and the residual glass matrix. The diffuse EBSD-patterns 1 and 2 are representative for patterns of this phase in these samples. Red spots mark the locations where the chemical compositions crystal 1 and 2 presented in Table 1 were obtained. The EDX-line scan presented below was obtained along the dotted line.

atomic weight. After 6 h, the thickness of the YAG-layer is basically the same as after 3 h. The adjacent layer 2 does not show dendrites and grew around the already existing stars. Additionally, brighter streaks of the third phase (slightly higher material contrast in the SEM-micrograph) are observed, which grew away from the surface with a much larger growth velocity than that observed for layer 2. After 24 h the zone associated to surface crystallization extends to a depth of 250–300 μm below the surface, see arrows in Fig. 4c). The surface crystallized layers 1 to 3 may be discerned by their material contrast and growth morphology which also includes the streaks growing away from the surface. It seems likely that the pore-containing interface in the bulk indicates where the surface crystallization was stopped by the crystals resulting from bulk nucleation already visible in Fig. 2b). Pores without a systematic arrangement are also observed at the immediate surface, see Fig. 1, and throughout the bulk.

Fig. 5 presents EDX studies of the star-shaped phase. The EDX-maps show that they are enriched in aluminium and oxygen but depleted of silicon, yttrium, sodium and cerium. This is in agreement with the dark appearance of the stars in the SEM-micrographs of Fig. 4. Representative spot measure-

Fig. 4 Cross section SEM-micrographs of the surface crystallization in samples annealed at 1000 °C for different periods of time: a) 3 h, b) 6 h and c) 24 h. The surface crystallization layers 1–3 are indicated.

Table 1 Compositions obtained from crystals and residual glass using EDX

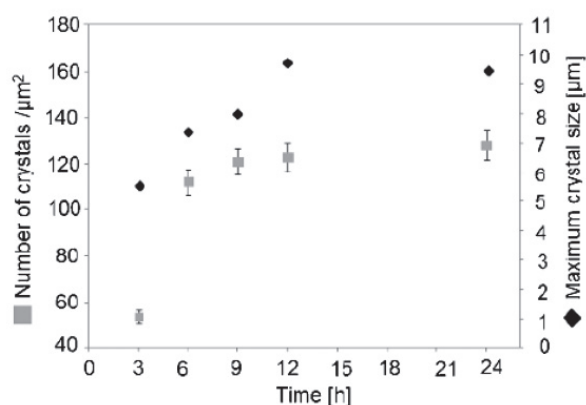| mol%	Y_2O_3	Al_2O_3	SiO_2	Na_2O	Ce_2O_3
Crystal 1	5.78	82.35	10.41	0.91	0.55
Crystal 2	5.20	84.09	9.14	1.02	0.55
Glass	23.02	21.00	51.25	3.52	1.21

Fig. 6 Number of star-shaped crystals over annealing time and maximum size of star-shaped crystals over annealing time.

Fig. 7 EBSD-patterns of the four indexable phases in the system.

ments at the locations a) and b) in Fig. 5 indicate the chemical compositions stated in Table 1. The chemical composition of the star-shaped structures indicates it could be mullite $Si_{2-x} \cdot Al_{4+2x}O_{10-x}$ which may vary in a broad range: $0.19 < x < 0.59$.[21] The Si/(Si + Al)-ratio in the SiO_2 poor limit is 0.136. However, it has been shown that the preparation of mullite with far smaller silicon concentrations is possible under special conditions.[22–26] It should be mentioned that the star shaped crystals are not large enough and to fingered too fully exclude an influence of the surrounding matrix during EDX-analysis.

Two selected EBSD-patterns from the locations 1 and 2 are also presented. They show very diffuse Kikuchi bands and could not be indexed reliably. However, the occurrence of these bands proves that the star-shaped phase is crystalline and the crystal lattice present in the information volume of EBSD is disturbed. Both patterns were obtained from the same structure. They are not identical and hence result from different lattice orientations, proving that the stars are not single crystals but composed of different orientations growing away from a centre where heterogeneous nucleation occurred.

The EDX line scan presented below was recorded along the dotted line in Fig. 5. It confirms the lower alumina concentration between the crystals and an enrichment of the glass matrix in yttrium and silicon. A steep diffusion profile (e.g. in alumina) is not detected near the star-shaped crystals and hence a diffusion barrier should not be formed around the crystals.

The number of star-shaped crystals and their maximum size has been plotted in Fig. 6 as a function of time. Three representative areas of a respectively annealed sample were analyzed. After an induction period, the number of star-shaped crystals in the bulk quickly increases for up to 9 h after which only a slight increase is observed. The size of the largest detectable crystal increases for up to 12 h and remains constant for an annealing time of 24 h within the limits of error. This may be caused by the difficulty of detecting the
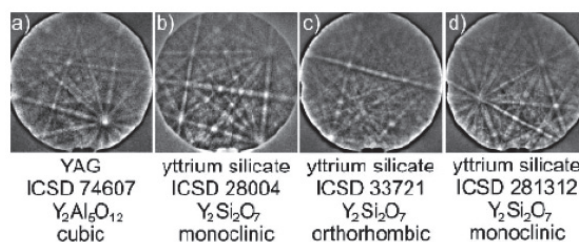
extremes of the size distribution in a fully crystallized sample, see Fig. 4c).

EBSD was applied in order to identify the crystalline phases because the XRD-results were inconclusive, to analyze orientation relationships between them and ratify their location. Fig. 7 shows EBSD-patterns recorded from four phases in the microstructure which allow acceptable pattern acquisition. Relevant indexing parameters are presented in Table 2. Pattern a) was obtained from the dendrites in layer 1 and reliably indexed as YAG (ICSD 74607). Pattern b) originates from the crystals of layer 2 and was reliably indexed as monoclinic $Y_2Si_2O_7$ (ICSD 28004, JCPDS 00-042-0167). The third layer of crystallization yielded the EBSD-pattern c) which may be reliably indexed as orthorhombic $Y_2Si_2O_7$ (ICSD 33721, JCPDS 00-042-0168). According to the JCPDS files, this monoclinic and the orthorhombic $Y_2Si_2O_7$ phase have densities of 4.48 and 4.97 g cm^{-3} respectively. Hence the crystals in layer 3 have a higher density than those in layer 2, which explains the higher material contrast of this layer in the SEM-micrographs of Fig. 4. The fourth pattern d) was obtained from the bulk and can be reliably indexed as another monoclinic $Y_2Si_2O_7$ (ICSD 281312, closest crystallographic relationship to JCPDS 01-038-0440 but no direct attribution) with a different space group than that of pattern b). The phase identification of these

Table 2 EBSD-indexing parameters

| IAT 1		Votes	Fit [°]	CI
Pattern a)	YAG	52	**0.51**	0.223
	ICSD 28004	1	0.84	0.000
	ICSD 33721	10	0.71	0.027
	ICSD 81312	4	0.76	0.000
Pattern b)	YAG	10	1.29	0.000
	ICSD 28004	**111**	**0.50**	**0.342**
	ICSD 33721	11	1.29	0.033
	ICSD 81312	12	1.45	0.042
Pattern c)	YAG	5	0.76	0.005
	ICSD 28004	4	0.76	0.000
	ICSD 33721	**81**	**0.54**	**0.282**
	ICSD 281312	2	0.80	0.005
Pattern d)	YAG	1	0.83	0.000
	ICSD 28004	1	0.81	0.005
	ICSD 33721	1	0.81	0.000
	ICSD 281312	**104**	**0.49**	**0.455**
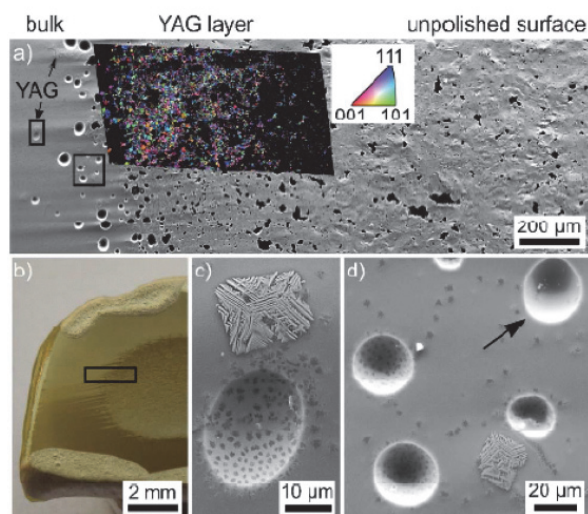
Fig. 8 Cut plane almost parallel to the surface: a) SEM-micrograph super-imposed by the IPF+IQ-map of a performed EBSD-scan, framed areas are presented in greater detail below. b) Location of the area (frame not to scale). c) YAG-dendrite in the bulk enclosing star-shaped crystals and pore with enhanced nucleation at its inner surface. d) Pore without enhanced nucleation at its surface (arrow).

yttrium silicates is purely based on the chemical composition and the crystallography analyzed by EBSD and not backed by XRD, see Fig. 3. However, these results make sense in contrast to the XRD-results which are very strange as outlined above. Hence we assume this phase identification to be correct. EBSD-patterns of the star-shaped crystals were presented in Fig. 5 but could not be indexed due to their low quality.

Despite these drawbacks, the positive identification of the phases by EBSD allowed acceptable scans of the system. Fig. 8 presents results from a cut plane parallel to the original surface of a sample annealed for 3 h. During crystallization, a depression is formed at the centre of the sample, *i.e.* this cut plane transects the YAG-layer at a small angle allowing better analysis of the surface layer. The SEM-micrograph of Fig. 8a) presents an area framed in Fig. 8b): from right to left it shows unpolished surface, then polished YAG crystals and finally the bulk containing the star-shaped phase and a few YAG-dendrites growing ahead of the main crystallization front (arrows). The superimposed IPF+IQ-map of a performed EBSD-scan shows that the grain size increases with an increasing depth beneath the surface. In the IPF+IQ-map, the crystal direction perpendicular to the sample surface is attributed to a colour in the corresponding IPF-legend while the pattern quality is represented by a grayscale value to enhance contrast, *i.e.* data from high quality EBSD-patterns appears bright while low quality patterns *e.g.* obtained from residual glass or the star-shaped phase appear darker. An overall crystallographic texture is not indicated in the scan and the apparent growth selection does not lead to one in the analyzed area of crystallization.

The morphology and occurrence of pores in this cut plane is of greater interest: while comparatively few pores with irregular edges are observed at the unpolished surface, spherical pores are frequently observed adjacent to the growth front. The SEM-micrographs in Fig. 8c) and d) show the areas framed in the image above. Fig. 8c) presents a rectangular YAG dendrite incorporating star-shaped crystals (dark) and hence proving that there is no diffusion barrier preventing YAG growth close to the latter. The depression in Fig. 8c) is a pore with its inner surface completely covered by star-shaped crystals. Fig. 8d) shows further crystal covered pores but also a pore with only three discernible crystals, see arrow.

It may be concluded that most pores at the YAG growth front serve as nucleation centres for the star-shaped crystals. The pores themselves are likely formed due to internal stresses[27,28] arising from the density mismatch between the initial glass (3.42 g cm^{-3}) and YAG (4.55 g cm^{-3}) at the surface. It has been shown for pure SiO_2-glass that the atmosphere in a pore may play an important role for nucleation at its surface.[29] By analogy, a closed pore would be inert concerning crystal nucleation in this system but serve as a nucleation enhancer an soon as it is opened to the furnace atmosphere. Hence the pores grow spherically in the bulk due to the YAG-crystallization and expand towards the surface as more and more glass is transformed to YAG. As the pores are forced to grow between existing YAG-crystals, they assume the irregular shapes seen in Fig. 8a).

The cross section of a sample annealed for 12 h was chosen to analyze further growth during crystallization because these samples contain all formed phases but are not completely crystallized. This enables us to show individual growth structures of different phases clearly separated by areas where only star-shaped crystals and uncrystallised glass are observed.

Fig. 9 presents an SEM-micrograph where crystals grew from the surface (top) into the bulk. The micrograph is superimposed by the phase+IQ-map of an EBSD-scan. The three layers of surface crystallization are clearly discernible. The orthorhombic YS of layer 3 may be detected in the immediate vicinity of YAG (arrow), ratifying the idea that layer 2 is not continuous. It is also clear that YAG may be detected more than twice as far from the surface as the main YAG layer is thick, explaining the far reaching luminescence observed in Fig. 2c) and the YAG-dendrites ahead of the main growth front in Fig. 8a). As the star-shaped crystals are distributed more or less homogeneously in the samples, this again proves that the growth of YAG is not interrupted by the change in chemistry caused by the formation of the star-shaped crystals, but physically by the nucleation of the YS-phases and the pores. The dark spots in the map are caused by the uncrystallised glass, as well as by the star-shaped crystals where the IQ is very low, see Fig. 4.

The phase-specific IPF+IQ-maps below provide an overview of crystal orientations in the respective layers. The dendrites of layer 1 are homogeneously oriented within one grain as expected. It may be shown that these dendrites incorporate orientational changes of about $3°$ during their comparably

■ YAG   (ICSD 74607) cubic
■ Y$_2$Si$_2$O$_7$ (ICSD 28004) monoclinic
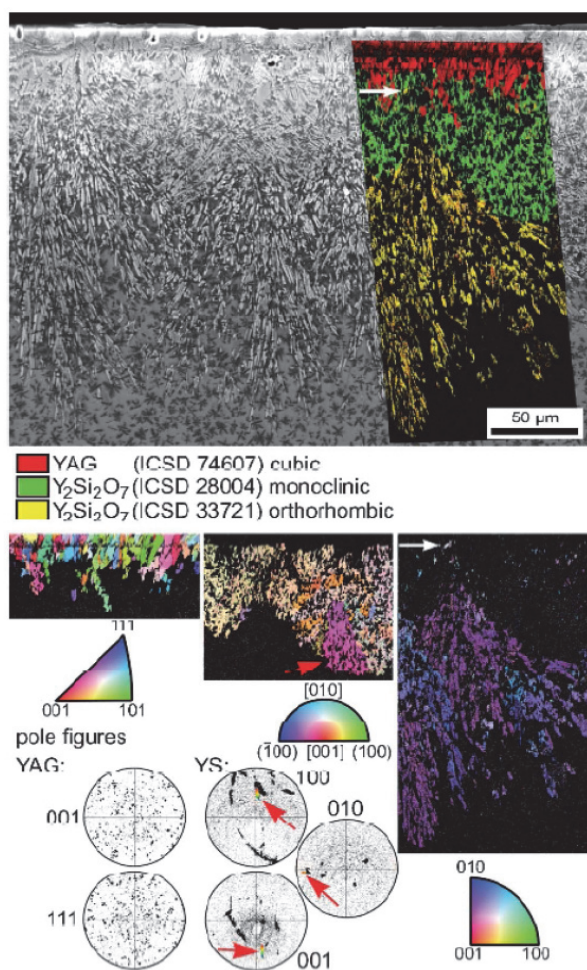■ Y$_2$Si$_2$O$_7$ (ICSD 33721) orthorhombic

Fig. 9 SEM-micrograph of a cross section of the sample annealed for 12 h superimposed by the phase+IQ-map of an EBSD-scan. The phase specific IPF+IQ-maps below provide an overview of the occurring crystal orientations. The 001- and 111-pole figures of YAG indicate a statistical orientation distribution.

Fig. 10 SEM-micrographs of growth structures in the bulk saturated by the star-shaped phase: the orthorhombic YS also observed in layer 3 (left) and the monoclinic YS only detected in the bulk (right).

short growth, which may be interpreted as some kind of stress relaxation or an immediate consequence of growth inhibiting barriers such as pores or star-shaped crystals. Dendrites growing unhindered in a glass melt may show orientation changes of less than 5° for more than 4 mm of growth in glass ceramics.[30] The presented 001- and 111-pole figures of the YAG phase indicate a statistical orientation distribution, matching comparable pole figures of the scan in Fig. 8a) and the XRD-pattern a) in Fig. 3.

The IPF+IQ-map of the monoclinic YS in layer 2 mainly shows orientations attributed to beige colours in the corresponding legend. Indexing this phase in scans is problematic with respect to the confidence index (CI) as it is prone to pseudo symmetry problems (two orientation solutions for an EBSD-pattern receive the same number of votes during the indexing process, see also ref. 31–33). The growth structure
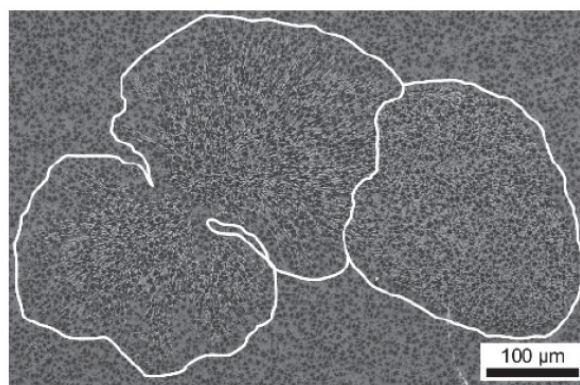
coloured pink in the map (red arrow) provided patterns with high CI-values and a systematic orientation change of 20° may be described from the top to the bottom: the short c-axis shifts from almost perpendicular to the initial surface towards being parallel to the latter. The data points attributed to this growth structure are highlighted in the presented pole figures. While the highlighted points show a strong orientation change in the 001 and 100 pole figures, they form a comparably small disk in the 010-PF. It may be concluded that the crystallographic b-axes are relatively fixed during growth while the a- and c-axes may change their orientation. The 010-PF also shows that the scan basically covers only six crystalline areas of different orientation with no clear commonality between them.

Layer 3 is composed of comparably few but large growth structures of the orthorhombic YS. The IPF+IQ-map of this phase implies that only two main structures are observed: one originating from the first occurrence of this phase near the white arrow, and a second growing into the scanned area from the left. The long a-axes of these crystals are basically aligned parallel to the growth direction implied by the respective crystal morphology.

Crystal structures of the orthorhombic YS of layer 3 may also be found in the bulk as a result of nucleation independent from the surface crystallized layers. Fig. 10 presents an SEM-micrograph showing growth structures resulting from the bulk nucleation of both the orthorhombic YS (left) and the monoclinic YS (right) outlined in white. While growth of the orthorhombic YS is always as fractal as observed in layer 3, the monoclinic YS grows more compact and similar to the YS of layer 2. Both structures imply outward growth from a nucleation centre with varying growth velocities and orientation changes during growth are probable. As the focus of this article is on the surface crystallization of YAG in this system, these structures formed by bulk nucleation are beyond its scope.

The growth model

The presented results show that there are five crystalline phases in these glass-ceramics after the annealing process. While the XRD-results concerning the YAG-layer are in agreement to the EBSD-results, the XRD-results aimed at identifying the other phases in the system are very strange and fail to show the phases indicated by EBSD and the chemical circumstance of the system. The target phase of fluorescent Ce^{3+}-doped YAG only forms a 30 μm thick layer of dendrites at the immediate surface with a few crystals penetrating up to 60 μm into the bulk. A preferred orientation of the YAG dendrites with respect to the surface is not detected. Hence, oriented nucleation[2,3,33−35] or the formation of a texture during subsequent crystal growth[2,3,33−35] is not observed. YAG-crystallization leads to the formation of pores at the growth front. This pore formation might be due to an increase in density or the release of water from the glass, both running parallel to the YAG crystallization. The water release would be caused by the smaller water solubility in the crystal than in the glass.

The surfaces of most of these pores are completely covered by star-shaped crystals, indicating much higher nucleation rates compared to the nucleation rates of this phase in the bulk. This is surprising because YAG is formed at the initial, polished surface instead of the star-shaped phase. This change of the nucleating phase may be due to the already changed composition of the uncrystallized glass at the growth front. Furthermore the surface properties resulting from the polish at room temperature could be quite different compared to those inside a pore at 1000 °C. Alternatively, YAG could simply nucleate and begin growing at lower temperatures than the star-shaped phase. The surfaces of the pores only become nucleation cites at 1000 °C in contrast to the polished surface where nucleation is possible after the sample is heated above T_g (845 °C).

It is noteworthy that the simultaneous surface crystallization of one phase and the bulk crystallization of another phase has not been described in the literature to the best of the authors' knowledge.

As the star-shaped phase crystallizes throughout the bulk, the residual glass is depleted of aluminium. This should be enhanced around the pores by the high density of star-shaped crystals at the pore surface. Either the change in chemistry or the star-shaped crystals themselves trigger the nucleation of three yttrium silicates (YS) of the composition $Y_2Si_2O_7$: one monoclinic YS near the surface, a different monoclinic YS in the bulk, and the orthorhombic YS near the surface as well as in the bulk. While the nucleation rate of the YS is relatively low in the bulk (a countable number in the entire sample after 12 h), it is much higher near the YAG layer, possibly because of the much higher number of star-shaped crystals nucleating on the pore surfaces. The occurrence of the two different monoclinic YS may be due to the growth front nucleation in contact with the YAG or to the larger depletion of alumina near the surface. The orthorhombic YS nucleates later or slower but grows faster than the monoclinic YS. Possibly the formation of

this phase does not depend as strongly on the glass composition and is more a result of heterogeneous nucleation initiated by the star-shaped crystals since it occurs near the surface as well as in the bulk. The star-shaped crystals continue to nucleate and grow in size for more than 12 h.

Yttrium silicates have been studied as they are candidates for laser materials and high energy phosphors if doped with rare earths.[36] Two binary crystalline compositions are reported to occur in the Y_2O_3–SiO_2 system: Y_2SiO_5 and $Y_2Si_2O_7$. $Y_2Si_2O_7$ shows a complex high temperature polymorphism with seven polymorphs denoted as α, β, γ, δ, ε, ζ and the high pressure η-phase described so far.[36] Ref. 37 contains an overview of the crystallographic data of the α- ζ-phases which enables to identify the YS detected in the samples analyzed here as β-, δ- and ε-$Y_2Si_2O_7$ by comparison to the data used to build the material files. ε-$Y_2Si_2O_7$ is found in layer 2, δ-$Y_2Si_2O_7$ in layer 3 and the bulk while β-$Y_2Si_2O_7$ is only found in the bulk.

There seem to be some discrepancies in the YS-nomenclature (or formatting problems), but assuming the ε-$Y_2Si_2O_7$ of ref. 37 is the same as the γ-phase of ref. 36, this phase has been described to be stable in an SiO_2-rich environment from 900–1050 °C and is reported to frequently occur as a metastable or intermittent phase.[38] Small Na-concentrations may stabilize this phase up to 1200 °C.[38] As Na is part of the present glass composition but not incorporated into the star-shaped phase, the high number of nuclei at the inner surface of the pores may lead to a relatively high Na-concentration near the YAG crystals, hence stabilizing ε-$Y_2Si_2O_7$. By contrast, this stabilizing effect is not observed in the bulk, where β-$Y_2Si_2O_7$ is detected.

As the annealing temperature is only 1000 °C, only the ε-$Y_2Si_2O_7$ is thermodynamically stable in these samples: β-$Y_2Si_2O_7$ is stable from 1225–1445 °C and δ-$Y_2Si_2O_7$ above 1535 °C.[39] Although a phase transition from one of the monoclinic phases to the other during cooling seems possible, the vastly different growth morphologies between the monoclinic and orthorhombic phases imply that they already occur as different phases during growth.

Conclusion

YAG crystals nucleated at the surface of the glass and grew into the bulk during annealing. This untextured crystal layer (layer 1) grew up to a thickness of 30 to 60 μm and showed a strong green fluorescence when excited by UV light. This proves the incorporation of Ce^{3+} into the YAG crystals. The nucleation of an unidentified star-shaped phase throughout the bulk occurs parallel to the YAG surface crystallization. A layer of pores is formed at the YAG growth front, enhancing local nucleation of this phase. Subsequent layers of nonfluorescent yttrium silicates of the composition $Y_2Si_2O_7$ (monoclinic and orthorhombic) are formed adjacent to the YAG and grow around the existing star-shaped crystals. Additional bulk nucleation of the orthorhombic YS and a different monoclinic YS is observed.

Acknowledgements

References

1 W. Wisniewski, C. A. Baptista, G. Völksch and C. Rüssel, *Cryst. Growth Des.*, 2011, **11**, 4660–4666.
2 W. Wisniewski, M. Nagel, G. Völksch and C. Rüssel, *Cryst. Growth Des.*, 2010, **10**, 1414–1418.
3 W. Wisniewski, K. Otto and C. Rüssel, *Cryst. Growth Des.*, 2012, **12**, 5035–5041.
4 A. Hunger, G. Carl, A. Gebhardt and C. Rüssel, *J. Non-Cryst. Solids*, 2008, **354**, 5402–5407.
5 S. Baghshahi, M. P. Brungs, C. C. Surrell and H. S. Kim, *J. Non-Cryst. Solids*, 2001, **290**, 208–215.
6 P. Wange, T. Höche, C. Rüssel and J. D. Schnapp, *J. Non-Cryst. Solids*, 2002, **298**, 137–145.
7 M. Dittmer, M. Müller and C. Rüssel, *Mater. Chem. Phys.*, 2010, **124**, 1083–1088.
8 A. Hunger, G. Carl and C. Rüssel, *Solid State Sci.*, 2010, **12**, 1570–1574.
9 A. Hunger, G. Carl, A. Gebhardt and C. Rüssel, *J. Non-Cryst. Solids*, 2008, **354**, 5402–5407.
10 A. Hunger, G. Carl, A. Gebhardt and C. Rüssel, *Mater. Chem. Phys.*, 2010, **122**, 502–506.
11 S. D. Stookey, J. S. Olcott, H. M. Gafinkel and D. L. Rothermel, in *Advances in Glass Technology*, VI. Intern. Confer., Plenum, New York, 1962, pp. 397–411.
12 S. Nishiura, S. Tanabe, S. Fujita and Y. Fujimoto, *Opt. Mater.*, 2011, **33**, 688–691.
13 A. Keshavarzi, W. Wisniewski and C. Rüssel, *CrystEngComm*, 2012, **14**, 6904–6909.
14 A. Keshavarzi and C. Rüssel, *Mater. Chem. Phys.*, 2012, **132**, 278–283.
15 A. Tarafder, A. R. Molla and B. Karmakar, *J. Am. Ceram. Soc.*, 2010, **93**, 3244–3325.
16 R. Müller, E. D. Zanotto and V. M. Fokin, *J. Non-Cryst. Solids*, 2000, **274**, 208–231.
17 J. W. P. Schmelzer, in *Nucleation Theory and Applications*, Wiley-VCH, 2005.
18 E. D. Zanotto, *J. Non-Cryst. Solids*, 1991, **129**, 183–190.
19 R. P. F. de Almeida, C. Bocker and C. Rüssel, *Chem. Mater.*, 2008, **20**, 5916–5921.
20 W. Wisniewski, G. Völksch and C. Rüssel, *Ultramicroscopy*, 2011, **111**, 1712–1719.
21 W. E. Cameron, *Am. Mineral.*, 1977, **62**, 747–755.
22 Y. Chen, B. Chi, Q. Liu, D. C. Mahon and Y. Chen, *Chem. Commun.*, 2006, 2780–2782.
23 R. X. Fischer, H. Schneider and H. M. Schmuecker, *Am. Mineral.*, 1994, **79**, 983–990.
24 R. X. Fischer, H. Schneider and D. Voll, *J. Eur. Ceram. Soc.*, 1996, **16**, 109–113.
25 P. Rehak, G. P. Kunath-Fandrei, P. Losso, B. Hildmann, H. Schneider and C. Jäger, *Am. Mineral.*, 1998, **83**, 1266–1276.
26 H. Schneider, *J. Am. Ceram. Soc.*, 1993, **76**, 1879–1881.
27 V. M. Fokin, S. A. Abyzov, J. W. P. Schmelzer and E. D. Zanotto, *J. Non-Cryst. Solids*, 2010, **356**, 1679–1688.
28 S. A. Abyzov, J. W. P. Schmelzer and V. M. Fokin, *J. Non-Cryst. Solids*, 2011, **357**, 3474–3479.
29 V. K. Leko, in *Nucleation Theory and Applications*, ed. J. W. P. Schmelzer, G. Röpke and V. B. Priezzhev, Joint Institute for Nuclear Research, Dubna, Russia, 2008, pp. 109–165.
30 W. Wisniewski, M. Nagel, G. Völksch and C. Rüssel, *Cryst. Growth Des.*, 2010, **10**, 1939–1945.
31 D. P. Field, *Ultramicroscopy*, 1997, **67**, 1–9.
32 R. de Kloe, M. M. Nowell and S. I. Wright, *A Systematic Study of Pseudo-Symmetry Problems in EBSD*, European Microscopy Congress, Antwerp, Belgium, 2004.
33 W. Wisniewski, T. Zscheckel, G. Völksch and C. Rüssel, *CrystEngComm*, 2010, **12**, 3105–3111.
34 W. Wisniewski, B. Schröter, T. Zscheckel and C. Rüssel, *Cryst. Growth Des.*, 2012, **12**, 1586–1592.
35 W. Wisniewski, M. Patschger and C. Rüssel, *CrystEngComm*, 2012, **14**, 5425–5433.
36 V. Kahlenberg, R. Kaindl and J. Konzett, *Solid State Sci.*, 2007, **9**, 542–550.
37 I. Hartenbach, S. Meier and T. Z. Schleid, *Z. Naturforsch., B*, 2006, **61b**, 1054–1060.
38 J. Ito and H. Johnson, *Am. Mineral.*, 1968, **53**, 1940–1952.
39 V. Kahlenberg, W. Wertl, D. M. Többens, R. Kaindl, P. Schuster and H. Schottenberger, *Z. Anorg. Allg. Chem.*, 2007, **634**, 1166–1172.

5.4

A. Keshavarzi, W. Wisniewski and C. Rüssel

EBSD and EDX Analyses of a Multiphase Glass-Ceramic Obtained by Crystallizing an Yttrium Aluminosilicate Glass

EBSD and EDX Analyses of a Multiphase Glass-Ceramic Obtained by Crystallizing an Yttrium Aluminosilicate Glass

Ashkan Keshavarzi, Wolfgang Wisniewski,* and Christian Rüssel

Otto-Schott-Institut, Jena University, Fraunhoferstrasse 6, 07743 Jena, Germany

ABSTRACT: A glass with the mol % composition 23.82 Y_2O_3·39.82 Al_2O_3·28.50 SiO_2·2.91AlF_3·4.95 ZrO_2 doped with 2 mol % CeF_3 is crystallized at 1250 °C for 20 h. The crystallized samples are studied using X-ray diffraction (XRD), the SEM-based methods EBSD and EDX, as well as fluorescence microscopy. Six crystalline phases are detected in the residual glass including alumina, YAG, Y-stabilized zirconia (YSZ), and three different yttrium silicates of the composition $Y_2Si_2O_7$. Chemistry-assisted indexing (ChI) is successfully applied to separate YAG and YSZ in EBSD-scans. YAG displays polygon as well as dendritic growth. Some crystals show both mechanisms at opposite ends, indicating that the growth mechanism is influenced by the chemistry of the surrounding glass matrix.

KEYWORDS: YAG, glass crystallization, EBSD, phase identification
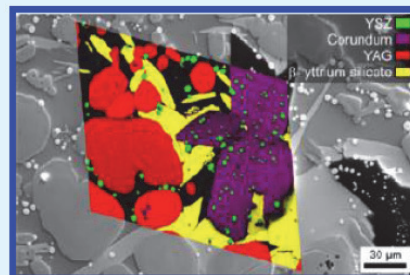
■ INTRODUCTION

In the past few years, the crystallization of yttrium aluminum garnet (YAG) from glasses has been studied because of the potential of these materials in lighting and optic technologies.[1−6] Nowadays, most commercial white light emitting diodes (LEDs) use a GaInN blue emitter with an emission peak at 460 nm in combination with a YAG:Ce^{3+} yellow phosphor.[4] Currently, YAG powders embedded in polymers such as polysiloxanes are generally used despite their poor thermal conductivity which prevents an effective removal of the heat generated in the phosphor. This limits the maximum light intensity of LEDs especially for high power applications. These problems are less significant when using crystallized YAG in an inorganic glass matrix which is furthermore very stable against corrosion. Unfortunately, yttrium alumo silicates do not possess a high tendency towards the crystallization of YAG. High temperatures are usually necessary to crystallize these glasses, which then in turn may lead to the crystallization of other phases such as an Al-rich phase and various yttrium silicates.[6] Unfortunately, the crystallization of YAG from glasses is difficult to achieve and hence scarcely described in the literature. Nevertheless, there are some reports on the spontaneous crystallization of YAG while cooling a melt[7] and the controlled crystallization of YAG from glasses.[2,3,6] The nucleation in the melt and the subsequent crystal growth kinetics are notably affected by the diffusion of components from the glassy matrix to the interface crystal/glass and vice versa. Chemical variations may significantly change the growth mechanisms of YAG in glass as well as nucleation rates.[3] The growth of YAG in glasses has been described to lead to polygon structures[3] as well as to dendrites.[2,6]

The transparency of the glass-ceramics is usually discussed in terms of light scattering by crystals dispersed in a glass matrix. However, good transparency requires low optical scattering and low atomic absorption. The attenuation of light due to scattering depends upon the difference in the refractive indices of the two phases and the size and distribution of crystals in the glass. While the size of the crystals must usually be smaller than the wavelength of light if scattering and diffraction is to be avoided, recently prepared glass-ceramics containing large crystals also show a high transparency due to adapted diffractive indices.[8] Some traditional transparent glass-ceramics contain fairly large volume concentrations of crystals (up to 85%) but do not scatter light due to the small crystal size.[9−11] A possible strategy to avoid light scattering is to prepare a material with crystallite sizes notably smaller than half the wavelength of visible light (usually <50 nm) or only produce a thin surface layer of YAG.[4,6,12] For lighting, the light conversion from blue LEDs to white light does not necessarily require a material without any light scattering.

In this work, we present the crystallization of multiple phases from a glass including Ce^{3+}-doped YAG of both dendritic and polygon morphology. The sensitivity of phase formation and crystal growth with respect to the glass chemistry is illustrated by the contrast between homogeneous glass and a stria of different composition.

■ EXPERIMENTAL APPROACH

A glass of the mol % composition 23.82Y_2O_3·39.82Al_2O_3·28.50SiO_2·2.91AlF_3·4.95ZrO_2 doped with 2 mol % CeF_3 was prepared from reagent grade raw materials. A mixed batch of 100 g of raw oxides was melted for 3 h in a platinum−rhodium crucible using an electric furnace heated to 1590 °C. The melt was stirred manually to homogenize it and finally cast on a copper block, quenched with a copper stamp, and transferred to a furnace preheated to 850 °C, which was subsequently switched off, cooling the glass with a rate of about 5 K/min.

Differential thermal analyses (Shimadzu DTA50) were performed using Al_2O_3 powder as a reference standard and a heating rate of 5 K/min from room temperature to 1300 °C. To study the crystallization behavior, we cut the glass into pieces of about $1 \times 1 \times 1$ cm^3 and transferred them to a furnace preheated to 800 °C, heated them to 1250 °C using a rate of 10 K/min where they were kept for 20 h. Finally, the furnace was switched off and the samples cooled with a rate of approximately 5 K/min.

The glass and annealed samples were characterized by X-ray diffraction in a θ-2-θ-setup (Siemens D5000) using Cu$_{K\alpha}$ radiation. The glass-ceramics were further characterized using a Jeol JSM-7001F scanning electron microscope (SEM) equipped with an EDAX Trident analyzing system containing a TSL Digiview 3 EBSD-camera. Samples were mounted using Ag paste and coated with a thin layer of carbon at about 1×10^{-3} Pa to achieve a conductive surface. EBSD scans were collected and evaluated using the programs TSL OIM Data Collection 5.31 and TSL OIM Analysis 5.31. EBSD data acquisition was performed using a accelerating voltage of 20 kV.

■ RESULTS AND DISCUSSION

The prepared glass was yellowish and optically transparent. The glass transition temperature T_g determined by dilatometry was 860 °C. Figure 1 presents XRD-patterns obtained from the
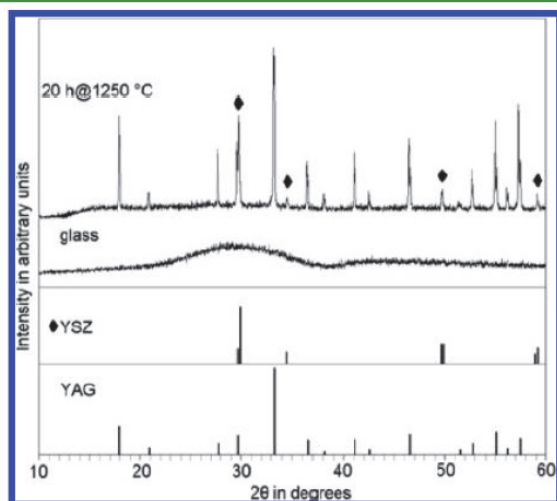

Figure 1. XRD pattern of the glassy sample and the samples crystallized at 1250 °C for 20 h.

solid glass and from a sample annealed at 1250 °C (390 K above T_g) for 20 h and powdered for XRD analysis. While the casted glass is X-ray amorphous; the annealed sample shows distinct XRD-lines which are all attributable to YAG (JCPDS file 82−0575) and yttrium-stabilized zirconia (YSZ, JCPDS file 037−1307). Other phases are not indicated by XRD.

A photograph of the polished surface of a sample annealed for 20 h is presented in Figure 2a. A white stria is discernible near the top of the otherwise yellow sample. The framed area is presented in the SEM micrograph of Figure 2b, which already reveals the presence of more phases than indicated by XRD analysis. The EBSD patterns of six crystalline phases are presented below, most of which may also be discerned by their SEM contrast. Pattern 1 was obtained from the darkest phase in the SEM-micrograph and may be well-indexed as α-Al_2O_3 (corundum). The dark gray phase forming the polygon structures outside the stria and the finer structures inside the stria are both YAG (pattern 2, ICSD-file 74607). The slightly brighter structures in the SEM micrograph provide the EBSD
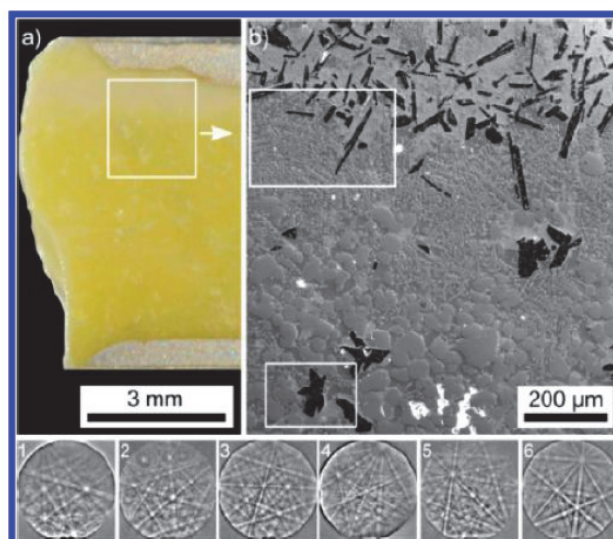

Figure 2. (a) Image of the polished surface of a sample crystallized at 1250 °C for 20 h. (b) SEM micrograph of the area framed in a. The areas framed in b are presented in the Figures 3 and 5 in greater detail. The EBSD patterns 1−6 were obtained from different crystal phases in the sample.

patterns 3−5, which may all be indexed as yttrium silicates (YS) of the composition $Y_2Si_2O_7$ and are not easily separated by their SEM contrast. Pattern 3 indicates monoclinic ε-$Y_2Si_2O_7$ (ε-YS, ICSD-file 28004), whereas pattern 4 indicates orthorhombic δ-$Y_2Si_2O_7$ (δ-YS, ICSD-file 33721). Both of these phases are detected only inside the stria, whereas the third YS indicated by pattern 5 is monoclinic β-$Y_2Si_2O_7$ (β-YS, ICSD-file 281312) and only found outside the stria.

The smallest crystals are very bright but difficult to discern at this magnification and may also be indexed as YAG although they clearly have a different mean atomic number. EDX-analyses were performed and confirmed the chemical compositions of the previously described phases. The bright phase showed a composition of 27.7Zr·11.6Y·59.2O·1.0Ce·0.5 Al (at %), meaning this is the YSZ indicated by XRD where some of the Y has been substituted by Ce and Al was basically expelled from the crystal during its growth. Although YAG and YSZ share the same cubic space group, the a-axis of YAG (ICSD-file 74607, $a = 12.024$ Å) is more than twice as large as that of YSZ (ICSD-file 164864, $a = 5.165$ Å). It is hence possible to distinguish these phases in the EBSD software using the bandwidth ratio matching function. However, activating this function in scans incorporating all occurring phases introduced new indexing problems especially for corundum.

The area inside the lower frame of Figure 2b is presented in a higher magnification in Figure 3 to visualize the crystallization outside the stria. The small, bright YSZ-crystals are now clearly visible. Because of the problem of separating YSZ and YAG based on their crystallography, chemistry-assisted indexing (ChI) was used to distinguish the phases in the EBSD scan performed within the area framed in the SEM-micrograph. In this process, EDX data are collected simultaneously to the EBSD patterns and later used to reindex the scan and distinguish phases based on their chemistry as well as their crystallography.[13] The achieved phase distinction enables to perform phase specific crystal orientation and texture analysis.

The presented phase+IQ map of the scan (left) shows that phase distinction was successful. It also shows that only one of
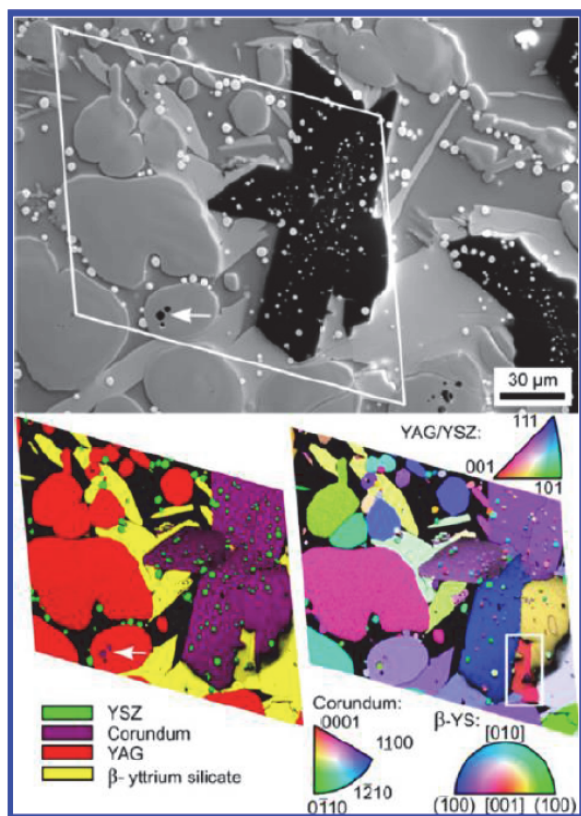
8532

dx.doi.org/10.1021/am401953j | ACS Appl. Mater. Interfaces 2013, 5, 8531−8536

Figure 4. SEM micrograph illustrating the faceting of YSZ crystals. The EBSD pattern was obtained from the YSZ hexagon, and the wire frame of the unit cell is presented to visualize the indexed orientation.

Figure 3. SEM micrograph of the microstructure in the lower frame of Figure 2b. An EBSD scan was performed inside the frame area. The phase+IQ map (left) and the IPF map (right) of the scan are presented below.

Figure 5. SEM micrograph of the microstructure in the upper frame of Figure 2b. An EBSD scan was performed inside the frame area. The phase+IQ map of the entire scan (left) is presented as well as the IPF map of YAG only (right).

the three dark spots inside the YAG crystal (white arrow) is a pore, whereas the other two are corundum crystals with morphologies very different from that of the large corundum crystals observed throughout the sample. The correlation of the phases in this map with the orientation information presented in the IPF+IQ map presented to the right shows that the large corundum structure is in fact composed of multiple crystals of different orientations. None of the phases in this map show orientational commonalities between individual crystals. A larger area of polygon YAG was also scanned to confirm this statement with a representative number of crystals. The framed area in the IPF+IQ map contains two β-YS crystals which share a common (110) plane, i.e., twinning of this phase is observed. As this area of β-YS is almost surrounded by corundum, it seems likely that twinning occurred as a mechanism of stress relaxation either during growth or cooling.

As the YSZ crystals in Figure 3 do not show a discernible texture, it may be concluded that YSZ usually assumes the shape of small spheres. In some cases, crystallographically characteristic shapes (faceting) may be observed as shown in Figure 4. Indexing the EBSD pattern obtained from the YSZ hexagon shows that this crystal has an orientation with a (111) plane almost parallel to the cut plane of the sample as indicated by the wire frame. Hence, this crystal probably formed a cube during its growth. Note that the YSZ crystals are much smaller if embedded in corundum compared to the rest of the sample in Figures 3 and 4.

As stated before, the growth morphology of YAG is very different inside the stria. Figure 5 presents the area in the top
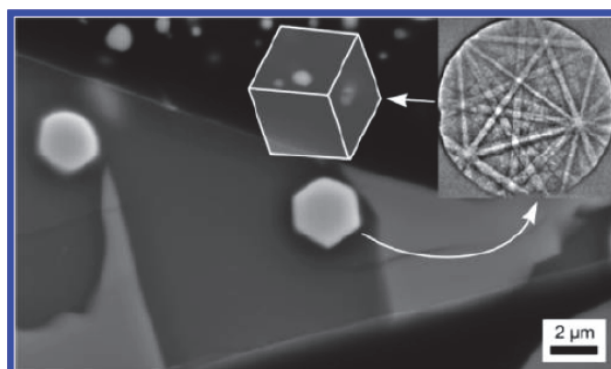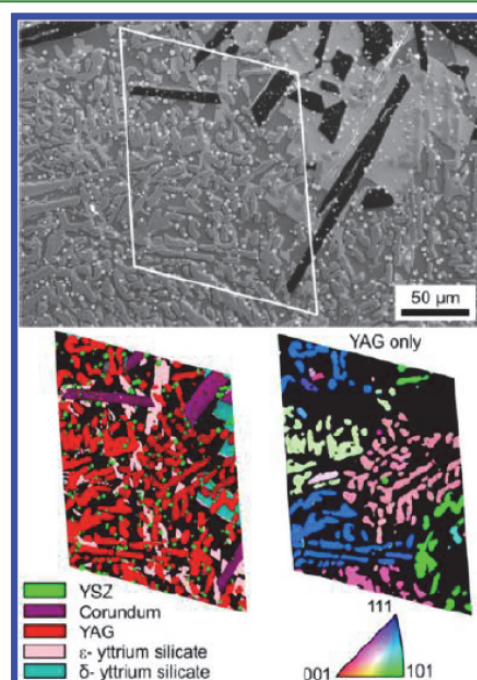
frame of Figure 2b in greater detail to visualize crystal morphologies. An EBSD-scan was performed inside the framed area and reindexed using ChI to provide the phase+IQ map presented below. In addition to visualizing the achieved phase separation, this map also shows that δ-YS occurs in the core of the stria, whereas ε-YS is observed between the YAG crystals. As the morphology of YAG is of interest in this case, the selective IPF+IQ map of YAG is also presented. The observed orientation relationships and growth morphologies clearly show that the figure presents a 2D cut through 3D dendrites of YAG, i.e., a completely different growth mechanism compared to the polygon growth outside the stria. The dendritic structures in Figure 5 incorporate orientation deviations of less than 3° over distances of more than 100 μm. Similar changes in the crystal orientation were observed after the surface crystallization of YAG.[6] By comparison, much larger dendritic structures with

46

orientational changes of less than 5° over distances of more than 4 mm have been grown from glass melts using chemically induced nucleation.[14] Dendritic fragmentation,[15] however, was not detected in these samples.

YAG crystals showing both polygon and dendritic growth may be observed at the bulk/stria interface as shown in Figure 6. An EDX line scan (15 kV) was performed along the arrow
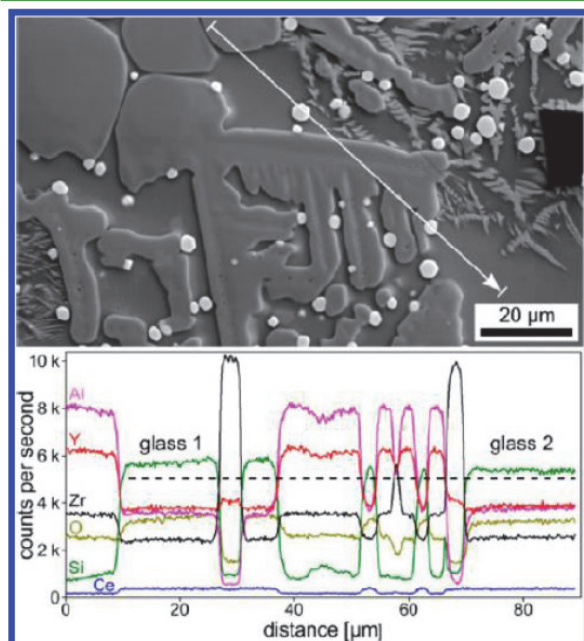

Figure 6. SEM micrograph featuring a YAG crystal showing polygon as well as dendritic growth. The results of an EDX linescan performed along the superimposed line are presented below.

and the results are presented below. Most of the indicated compositions match what would be expected of the respective crystal phase, including the low Al content in YSZ previously mentioned. However, the residual glass 1 near the polygon YAG clearly contains more Si than the residual glass 2 in the area where dendritic YAG is observed. Additionally, the residual glass and the YSZ crystals show higher Ce concentrations than YAG where it should be incorporated to cause the fluorescence expected from the material.

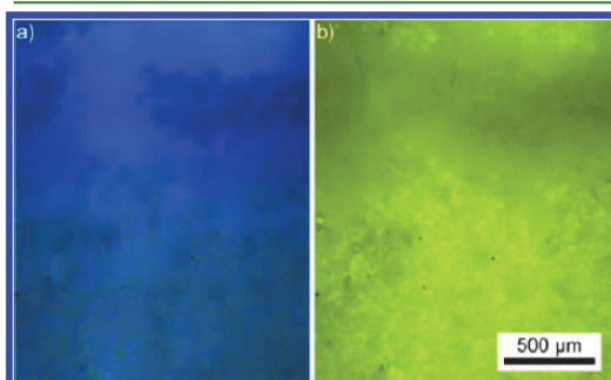Figure 7 presents fluorescence micrographs of the sample exited with two different wavelength ranges: (a) 300−400 nm

Figure 7. Fluorescence micrographs of the sample surface excited by light of the wavelengths (a) 300−400 nm and (b) 450−490 nm.

and (b) 450−490 nm. The strong blue fluorescence inside the stria (top) is cause by the yttrium silicates, whereas the strong yellow fluorescence results from the YAG crystals. Hence enough Ce^{3+} was incorporated into the YAG crystals to achieve the desired fluorescence. Intensity differences between dendritic and polygon YAG were not observed.

Pores are frequently observed between the crystals in the sample as seen in Figure 8, where the surface was tilted by 70°
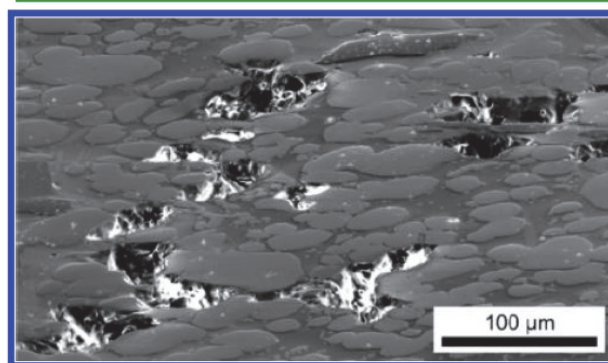

Figure 8. SEM micrograph of the sample surface tilted by 70° featuring large pores in the material.

to enhance the topographical contrast. They may be explained by the volume contraction accompanying crystal growth. Pore formation adjacent to YAG crystallization in glasses was also recently described in a surface crystallizing system.[6]

The occurrence of multiple crystalline phases in the glass-ceramics enables to optimize their properties by controlling the crystallization with respect to grain size and phase percentages.[16] The formation of YSZ and various yttrium silicates next to YAG has also been observed during the crystallization of yttrium oxynitride glasses[17] which are, however more complicated to produce as the glasses must be melted in a nitrogen atmosphere. Additionally the glass analyzed here only contains such small quantities of yttrium silicates and corundum that they fail to be detected by XRD analysis.

A clear crystallization chronology may be formulated based on the data presented above: YSZ is the first phase to crystallize as it is enclosed in all other phases. Corundum is the second phase to crystallize because the YSZ crystals inside the corundum crystals are clearly smaller than those enclosed in YAG and the residual glass, i.e., their growth was stopped earlier. The third phase to crystallize is YAG because it incorporates larger YSZ crystals. In contrast to the preferred (111)-orientation recently reported,[5] the YAG crystals presented here do not show a texture, which is in agreement to the results obtained from surface-crystallized YAG.[6] The corundum inclusions in YAG pointed out in Figure 3 show that YAG may also incorporate small corundum crystals although direct contact between YAG and corundum is otherwise rarely observed. The respective yttrium silicates nucleate on the surfaces of both corundum and YAG, i.e., they were the last phases to crystallize, possibly while the sample is cooled at the end of the annealing process.

All three YS were recently also found to crystallize in specific locations after the crystallization of YAG from a glass surface.[6] Similar to the results presented here where δ-YS formed around the corundum crystals in the stria and ε-YS appears further outside the stria, δ-YS was detected immediately next to the YAG layer where a higher number of star-shaped, Al-enriched

47

crystals were shown to exist[6] followed by a layer of ε-YS. The β-YS detected outside the stria was only found in the bulk of the surface crystallizing glass.[6] The crystal morphologies were very different in ref 6 because of the high number of star-shaped crystals blocking their growth.

YSZ nucleation is clearly not homogeneous in the sample, even outside the stria. Corundum crystals are always observed in an area of elevated YSZ nucleation, hence its growth is probably initiated by the local Al enrichment caused by strong local YSZ growth which does not incorporate Al, see Figure 6. YAG nucleates throughout the sample except for the core of the stria, where the density of corundum crystals is so high that the aluminum concentration in the residual glass was presumably not high enough to allow YAG crystallization.

The YAG growth mechanism in the stria differs from the crystallization outside this region. Furthermore, the EDX line scan in Figure 6 illustrates that the Si concentration is higher near the polygon YAG than near the dendritic YAG. As dendritic YAG is only observed inside the stria, it may be concluded that the SiO_2 concentration should be lower here than outside the stria. Recently, J. Du[18] reported on yttrium aluminosilicate glass with comparably low silica concentrations (5−20 mol %). It was shown that the coordination number of aluminum and yttrium decreases with increasing silica concentrations. Hence the coordination of aluminum shifts from octahedral to tetrahedral. Alumina with tetrahedral coordination enters the Si−O network and acts as network former. Aluminum in octahedral coordination would hence be preferred in the stria and then leads to a smaller local viscosity. This leads to a higher nucleation rate of YSZ, which in turn triggers the growth of corundum.

The higher Si concentration of the residual glass near the polygon YAG indicates aluminum should preferably occur in tetrahedral coordination, which would raise the local viscosity. This difference in the local viscosities could cause the observed growth mechanism change. If this is correct, it could be in agreement with the literature, where simulations showed that the growth mechanism of viscose fingering may be changed to dendritic growth by changing the viscosity of the matrix.[18,19]

The model of viscous fingering was developed for the case of two fluids with different viscosities forming interpenetrating structures. It might also be applied to explain crystal growth morphologies indicating tip splitting and possible fingering, which have been observed in glass-ceramics,[21,22] i.e., the growth mechanisms may be comparable.

It is noteworthy that YSZ is rarely surrounded by YAG but instead mostly occurs at the interface, see Figures 3−6. Hence it seems plausible that YSZ crystals are pushed along by the YAG growth front. A similar behavior has already been described in the literature where growing polymer-dendrites pushed away clay particles suspended in the aqueous polymer solution.[20] As there are much fewer YAG crystals then YSZ crystals in the described areas, it seems unlikely that YSZ acts as a nucleation agent for YAG. Nevertheless, larger nucleation rates should lead to the preferred formation of isolated YAG particles, whereas smaller nucleation rates should preferably lead to dendritic growth. The latter has its reason in a limited transport at the growth front, either in the transport of the crystallization energy from the growth front or in the diffusion of components, during which the respective crystal is formed from the growth front.

CONCLUSIONS

A glass of the composition $23.82Y_2O_3 \cdot 39.82Al_2O_3 \cdot 28.50SiO_2 \cdot 2.91AlF_3 \cdot 4.95ZrO_2$ doped with 2 mol % CeF_3 showed nucleation and subsequent crystal growth in the bulk after thermal annealing for 20 h at 1250 °C. A stria of changed chemical composition led to very different results confined to a local area. The initial and unequally distributed nucleation of YSZ leads to the crystallization of corundum where the YSZ nucleation rate is high. YAG crystals nucleate in a later stage and probably push YSZ crystals along as they grow instead of growing around them, indicating comparably slow growth. In the bulk of the glass, YAG forms polygon crystals without orientational commonalities. Inside the stria, a reduced viscosity of the glass matrix probably changes the mechanism of YAG-growth to dendritic growth. Finally, three different yttrium silicates of the composition $Y_2Si_2O_7$ nucleate preferably in the vicinity of corundum crystals. Both YAG and the yttrium silicates show fluorescence indicating the incorporation of Ce^{3+} into their structure and making this material a candidate for light transforming applications. Pores are formed because of the density increase during crystallization.

AUTHOR INFORMATION

Corresponding Author

*E-mail: wolfgang.w@uni-jena.de. Tel: (0049) 03641 948515. Fax: (0049) 03641 948502.

Notes

The authors declare no competing financial interest.

ACKNOWLEDGMENTS

REFERENCES

(1) Fujita, S.; Tanabe, S. *Opt. Mater.* **2010**, *32*, 886−890.
(2) Keshavarzi, A.; Wisniewski, W.; Rüssel, C. *CrystEngComm.* **2012**, *14*, 6904−6909.
(3) Keshavarzi, A.; Rüssel, C. *Mater. Chem. Phys.* **2012**, *132*, 278−283.
(4) Nishiura, S.; Tanabe, S.; Fujita, S.; Fujimoto, Y. *Opt. Mater.* **2011**, *33*, 688−691.
(5) Yang, J.; Chen, B.; Pun, E. Y. B.; Zhai, B.; Lin, H. *J. Lumin.* **2013**, *134*, 622−628.
(6) Keshavarzi, A.; Wisniewski, W.; de Kloe, R.; Rüssel, C. *CrystEngComm* **2013**, *15*, 5425−5433.
(7) Nishi, M.; Tanabe, S.; Fujita, K.; Hirao, K.; Pezzotti, G. *Solid State Commun.* **2004**, *132*, 19−23.
(8) Berthier, T.; Fokin, V. M.; Zanotto, E. D. *J. Non-Cryst. Solids* **2008**, *354*, 1721−1730.
(9) Höland, W.; Beal, G. H. *Glass Ceramic Technology*; Wiley−The American Ceramic Society: Westerville, OH, 2012.
(10) de Almeida, R. P. F.; Bocker, C.; Rüssel, C. *Chem. Mater.* **2008**, *20*, 5916−5921.
(11) Bocker, C.; Bhattacharya, S.; Höche, T.; Rüssel, C. *Acta Mater.* **2009**, *57*, 5956−5963.
(12) Hendy, S. *Appl. Phys. Lett.* **2002**, *81*, 1171−1173.
(13) Nowell, M. M.; Wright, S. I. *J. Microsc.* **2004**, *213*, 296−305.
(14) Wisniewski, W.; Nagel, M.; Völksch, G.; Rüssel, C. *Cryst. Growth Des.* **2010**, *10*, 1939−1945.

48

(15) Rettenmayr, M. *Int. Mater. Rev.* **2009**, *54*, 1−17.

(16) Wange, P.; Höche, T.; Rüssel, C.; Schnapp, J. D. *J. Non-Cryst. Solids* **2002**, *298*, 137−145.

(17) Vomacka, P. *J. Eur. Ceram. Soc.* **1997**, *17*, 615−621.

(18) Du, J. *J. Am. Ceram. Soc.* **2009**, *92*, 87−95.

(19) Nittmann, J.; Stanley, H. E. *Nature* **1986**, *321*, 663−668.

(20) Gránásy, L.; Pusztai, T.; Warrem, J. A.; Douglas, J. F.; Börzsönyi, T.; Ferreiro, V. *Nat. Mater.* **2003**, *2*, 92−96.

(21) Haas, S.; Hoell, A.; Wurth, R.; Rüssel, C.; Boesecke, P.; Vainio, U. *Phys. Rev. B* **2010**, *81*, 184207.

(22) Wurth, R.; Rüssel, C. *Solid State Sci.* **2011**, *13*, 1132−1136.

8536

dx.doi.org/10.1021/am401953j | *ACS Appl. Mater. Interfaces* 2013, 5, 8531−8536

49

5.5

Ashkan Keshavarzi, Christian Bocker and Christian Rüssel

Nano Lamellae Composed of Yttrium Aluminum Garnet and Yttrium Silicate by Surface Crystallization of Glass

CrystEngComm, 2013, Submitted.

CrystEngComm

Nano Lamellae Composed of Yttrium Aluminum Garnet and Yttrium Silicate by Surface Crystallization of Glass

Nano Lamellae Composed of Yttrium Aluminum Garnet and Yttrium Silicate by Surface Crystallization of Glass

Ashkan Keshavarzi*, Christian Bocker* and Christian Rüssel

Otto-Schott-Institut, Jena University, Fraunhoferstr. 6, 07743 Jena, Germany

*Corresponding authors: Ashkan Keshavarzi, Christian Bocker

Fraunhoferstr. 6, 07743 Jena

Otto-Schott-Institut, Jena University

Tel: (0049) 03641 948522

Fax: (0049) 03641 948502

E-mail: ashkan.keshavarzi@uni-jena.de

1

52

Nano Lamellae Composed of Yttrium Aluminum Garnet and Yttrium Silicate by Surface Crystallization of Glass

Ashkan Keshavarzi, Christian Bocker and Christian Rüssel

Otto-Schott-Institut, Jena University, Fraunhoferstr. 6, 07743 Jena, Germany

Abstract

Glasses with the mol% composition 17 Y_2O_3, 33 Al_2O_3, 40 SiO_2, 2 AlF_3, 3 CaO, 2 CeF_3, 3 B_2O_3 were thermally annealed at 950 and 1000 °C for different periods of the time. The crystallization kinetics as well as the mechanism of surface and bulk crystallization was clarified using X-ray diffraction, optical and electron microscopy as well as fluorescence spectroscopy. The application of advanced techniques in the scanning electron microscope (SEM) using Kikuchi diffraction of transmitted electrons (t-EBSD, TKD) supported the identification of the occurring crystal phases. The surface nucleation led to a coupled growth of eutectic yttrium-aluminum garnet. This surface layer consists of a lamellar structure composed by yttrium aluminum garnet and yttrium silicate. The nano lamellae originated from the surface and grew in an interpenetrating cell structure with an interspace of about 50 nm. Simultaneously, the growth of a seaweed shaped, aluminum enriched crystals, took place in the bulk of the sample. Around seaweed crystals, a diffusion layer depleted in aluminum is observed. The garnet surface layer is doped with Ce^{3+} as seen from the intense broadband fluorescence.

Keywords: YAG, yttrium silicate, Lamellae, glass crystallization

2

Introduction

Yttrium aluminosilicate glass-ceramics have received significant interest because of their unique optical and mechanical properties. [1] During the past few years, fluorescence properties of yttrium aluminum garnet ($Y_3Al_5O_{12}$, YAG) crystals have been widely studied due to its importance for lighting and laser applications. [2-4] Ce^{3+}-doped YAG is an advantageous component for the conversion of the blue light of light emitting diodes (LED) to white light. Such devices, up to now, are predominantly produced by doped garnet powders embedded in polymers, e.g. polysiloxanes. In general, polymers possess weak thermal conductivities in comparison to glasses. Heat generated in the phosphor has to be removed. Hence it should be advantageous if the YAG crystals were directly grown in a glassy matrix. Usually silicate glasses which contain the two required components, Y_2O_3 and Al_2O_3 do not possess a high tendency towards crystallization, and if they crystallize, fairly high temperature are required (>1250° C) or other crystalline phases, such as silicate solid solutions are formed. [5, 6].

Nucleation in glass-forming melts may occur by different mechanisms that are commonly distinguished as homogeneous and heterogeneous nucleation. In many glass compositions crystalline phases are formed near the surface during thermal annealing. [7] To achieve bulk nucleation, the addition of some percent of components such as ZrO_2 or TiO_2 may change the mechanism towards bulk nucleation. [8] These components lead to the bulk precipitation of one phase (e.g. to TiO_2 or $ZrTiO_4$) and subsequently to the crystallization of other phases. However, it should be noted that in certain glasses, these compounds also act as nucleation inhibitor. Such behavior was e.g. reported from borosilicate glass where the addition of zirconia hindered the nucleation in the glass. [9]

3

Ultra-high temperature metallic materials such as superalloys and intermetallics developed as promising materials for many mechanical applications. During the solidification process of these materials, the binary or multi-eutectic phases are simultaneously grown from the melt with a well oriented microstructure and with strong phase interface bonding. In analogy, also inorganic non-metallic materials prepared from eutectic compositions have exceptionally good mechanical properties. [10-13] In the following, the growth of YAG and yttrium silicates from a ternary composition in the system SiO_2 /Al_2O_3 /Y_2O_3 with some additives is described. It is remarkable that an eutectic growth from the surface is observed in such kind of glass systems which was not described before. The development of crystal phases and the kinetics of crystal growth in this glass-ceramics are described.

Experimental procedure

Glass with the mol% composition 17 Y_2O_3, 33 Al_2O_3, 40 SiO_2, 2AlF_3, 3CaO, 2 CeF_3, 3 B_2O_3 was prepared from pure reagent grade raw materials. The glass was melted in a 100 g batch in a platinum–rhodium crucible using an electric furnace heated to 1590 °C kept for 3 h. During the melting process, the melt was stirred from time to time manually using a platinum rod in order to homogenize the melt. Then the melt was cast on a copper block, quenched with a copper stamp and transferred to a furnace preheated to 850 °C and subsequently cooled using a rate of 5 K/min. The glass composition was analyzed by X-ray spectroscopy (EDS) in the scanning electron microscope (SEM) especially to see whether fluoride and boron are released during the melting process. The obtained glass composition after melting was 17.2 Y_2O_3, 33.5 Al_2O_3, 40.6 SiO_2, 1.5 AlF_3, 3.0 CaO, 2.0 CeF_3, 2.2 B_2O_3 (error: ±0.1) showing a slight deviation from the as melted batch due to the unavoidable evaporation of light elements during melting, e.g. boron and fluoride.

4

The glass samples were cut, ground and finally polished using diamond suspension with grain size 0.3-1μm. In order to crystallize the glass, polished and unpolished samples were transferred to a furnace and subsequently annealed at temperatures up to 1000 °C using a rate of 10 K/min. To remove any dust and grinding media in order to prevent surface crystallization induced by impurities, the polished samples were rinsed with ethanol and deionized water before annealing. Then, the samples were transferred to alumina containers covered by an alumina plate during subsequent annealing. The annealing temperature of 1000 °C was kept for 12, 24, 48 and 72 h. Another set of experiments was performed at 950 °C for 24, 48, 54, 60 and 80 h in order to investigate the effect of temperature on nucleation and crystal growth. Then the samples were cooled to 830 °C using a rate of 4 K/min. Finally, the furnace was switched off to achieve further cooling to room temperature.

Glasses and annealed samples were characterized by X-ray diffraction (Siemens D5000) using $Cu_{K\alpha}$ radiation. Here, some samples were characterized as bulk material, i.e. without powdering the sample. Differential Thermal Analyses (Shimadzu DTA50) were carried out in air using Al_2O_3 powder reference standard and a heating rate of 5 K/min (from room temperature to 1400 °C). For the dilatometer cylinders with a diameter of 8 mm and a length of 15 mm were drilled out. The heating rate of the dilatometer was 5 K/min until the dilatometric softening point was reached.

Fluorescence optical micrographs (FM) were obtained via laser scanning microscopy (LSM) using an Axio Imager Z1M LSM5-Pascal (Carl Zeiss Microscopy GmbH, Jena, Germany). The microstructures of several glass-ceramics were studied using a Schottky field-emission scanning electron microscope Jeol-JSM 7001F equipped with EDAX Trident system (EDS, WDS and EBSD detector). The sample annealed at 1000 °C for 24 h was studied by transmission electron microscope (TEM) using the HITACHI H8100 at 200 kV. The crystallized surface layer of this sample was studied by grinding the sample from the back. This

led to a sample of 120 µm thickness which contains the surface crystallized layer. The sample was mechanically dimpled and finished by ion beam milling (6°, 3 kV, 1.5 mA). The TEM-sample was also investigated in the SEM. With the attached EBSD system Kikuchi pattern could be obtained from the transmitted electrons. This technique is denoted as t-EBSD, t-EFSD or transmission Kikuchi diffraction (TKD). [14] For this purpose, a self-made sample holder was used. The stage was tilted by 70° which results in a 20° angle of the sample with respect to the EBSD-screen. This maximizes the area of irradiation of the fluorescent screen of the EBSD system (see Figure 1).

Results

The as-casted glasses appear yellowish but optically transparent. The XRD of the as-casted glasses showed no distinct peaks. The glass transition temperature determined by dilatometer was 845 °C. The samples annealed at 950 °C (105 K above T_g) for 48 h were also transparent. However, after annealing at a temperature of 950 °C for 48 h, trace quantities of crystals were detected by both XRD and SEM. A noticeable difference was not observed between the samples which were polished or not polished prior to the annealing process.

Figure 2 shows several images recorded by a laser scanning microscope (LSM) from the cross-section of the sample annealed at 1000 °C for 24 h. In Figure 2a, at least three different crystal morphologies are observed at the surface and in the bulk of the sample. Near the surface, a clearly visible crystalline layer occurs, supposedly formed by surface crystallization. The elongated shape of the surface crystals suggests that the crystals are nucleated near the surface and are grown subsequently into the bulk. In Figure 2b the crystalline layer at the surface with a thickness of around 200 µm is excited using laser light with a wavelength of 460 nm. This gives rise to the emission of light with a wavelength of 540 nm (green-yellowish color) which is

6

typical for Ce^{3+}-doped YAG crystals. Additionally, two further types of crystals are observed in the bulk of the sample. One type appears as larger spheres (several hundreds of micrometers) supposedly with spherulitic morphology and the other is much smaller (a few micrometers) and possesses a seaweed morphology (see Figure 2a). [15-18] It should be noted, if the laser is focused on the crystals in the bulk of the sample, fluorescence is not observed. Hence, cerium doped YAG crystals are not present in the bulk.

Figure 3 presents experimental XRD-patterns obtained directly from the surface of the samples annealed at 950 °C for 24, 48, 60 and 80 h. Characteristic peaks can be attributed to YAG (JCPDS 01-82-0575), y-$Y_2Si_2O_7$ (JCPDS 00-038-0440) and α-$Y_2Si_2O_7$ (JCPDS 00-038-0223). It should be noted that several intense peaks occurred that could not be attributed to a known phase. The sample annealed for 24 h is still amorphous without any hint of peaks. After annealing the glass for 48 or 60 h, peaks due to the formation of crystalline phases are observed. Since the manifold peaks of the yttrium silicate phases, the attribution to the crystalline phases is uncertain. The peak at $2\theta = 33.2°$ is most intense in the sample annealed for 48 h and might be attributed to the (420) lattice plane of YAG. By contrast, the sample annealed for 80 h shows intense XRD peaks that may be attributed to α-$Y_2Si_2O_7$ as the major crystalline phase. Besides YAG, minor quantities of y-$Y_2Si_2O_7$ are proved using simulated pattern by fundamental parameter analysis and Rietveld-refinement.

Figure 4 shows XRD patterns from the bulk of the samples annealed at 1000 °C for 48 and 72 h. Again the peaks can be attributed to YAG, y-$Y_2Si_2O_7$ and α-$Y_2Si_2O_7$ accordingly. The patterns of the samples annealed at 48 and 72 h are fairly similar and show a distinct peak at $2\theta = 29.6°$ which corresponds to the most intense peak of α-$Y_2Si_2O_7$ in the (120) lattice plane. In analogy to the sample annealed at 950 °C for 80 h, minor quantities of YAG and y-$Y_2Si_2O_7$ are most likely. From the samples annealed at 1000 °C, the surface layer was removed by grinding. Then XRD-patterns were recorded from the remaining bulk material as shown in Figure 4. In

7

the case of the sample annealed for 72 h, the patterns of the whole sample and without the surface layers are fairly similar. By contrast, in the sample annealed for 48 h, barely notable broadened peaks (see the mark in Figure 4) were observed in the bulk which indicates a minor concentration of crystal phase in the studied volume by X-ray diffraction. This experiment shows that predominantly α-$Y_2Si_2O_7$ is formed at the surface at shorter annealing times. While longer annealing times result in the formation of α-$Y_2Si_2O_7$ in the bulk as well.

In Figure 5 and 6, SEM-micrographs of polished cross-sections of samples annealed at 950 °C and 1000 °C for various periods of time up to 72 h are respectively shown. By analogy to the optical micrographs, a surface crystallized layer is observed. It is growing with time from the surface into the bulk of the glass. The crystallization front is emphasized by drawing a white line alongside in Figure 5 and 6. Underneath the surface, crystals are observed which possess different size, structure and morphology. In the micrographs these crystals appear as dark, seaweed structures. The materials contrast indicates a phase with smaller mean atomic number. The seaweed structures also grow in both series with increasing annealing time. If they are near the surface, the surface crystallized layer grows around them until they are fully surrounded by the crystals that have grown from the surface. Furthermore it can be seen that the seaweed crystals are fairly small near the surface and get increasingly large in the bulk.

In order to investigate the surface crystallized layer, a slope-cut was prepared from the sample which was annealed at 1000 °C for 24 h and is illustrated in Figure 7. At the right side, a micrograph recorded from a cross-section with a higher magnification is shown. It reveals an interpenetration structure of a dark and bright appearing phase in the SEM. It seems that both phases grew simultaneously from the surface.

Figure 8 presents EDS-maps recorded in an SEM from the cross section near the seaweed structure. The microanalysis of the seaweed crystals in the sample annealed at 950 °C for 80 h showed that it predominantly consists of aluminum as shown in the EDS-map. Around the

8

crystal, the residual glassy phase is depleted in aluminum. Because the structure is only 2 μm in diameter, the acceleration voltage was decreased to 6 kV which results in an excitation volume around 0.3 μm in diameter and depth (simulated by EDAX Flight software) and an enhanced spatial resolution. However, due to the lower excitation energy for the X-rays, energies above 3 keV (e.g. Ca K$_\alpha$) are hardly detected (due to the decreased overvoltage ratio). Therefore, the result is not quantitative and the scale shows only netto intensities.

As stated above, the seaweed structures seem to be subsequently overgrown by the surface crystallized layer. However, the materials contrast around the crystals in Figure 6 indicates a third phase (brighter). The EDS-mapping of the sample that was annealed at 1000 °C for 24 h revealed a silicon and yttrium enriched crystalline phase around the aluminum enriched seaweed crystals as shown in the overlay of the EDS-map with the SEM-micrograph presented in Figure 8b. Studies by point analyses using EBSD proved that the dark appearing seaweed structure is also crystalline (Kikuchi pattern could be obtained but not indexed) while the matrix did not generate Kikuchi patterns (not shown). In principle, the latter can be explained by an amorphous phase or a disturbance of the crystal lattice leading to a non-constructive wave interference. However, a glassy residual phase in the bulk of the partly crystalline material is most probable.

As the surface crystallized layer is composed by an interpenetrating structure which is too small to be resolved in the SEM, TEM samples were prepared. In Figure 9a, bright-field TEM micrographs of the sample annealed at 1000 °C for 24 h are shown. In the overview, it is seen that two phases (bright and dark due to scattering contrast) occur that interpenetrate each other. This is in good agreement with the SEM micrographs shown in Figure 7. It should be noted that the contrast is inverted in the TEM in comparison with the SEM micrographs. The dark phase in the bright-field TEM possesses the larger mean atomic number.

9

Figure 9b shows a high resolution TEM micrograph of the area that is marked by a white rectangle in Figure 9a. Here, two areas of dark appearance with distinct diagonal lines occur, one of them in the left and the other one in the right of the micrograph. In between, crystalline structures were not observed and hence for a better visibility of the dark area the middle was cropped. In both dark areas the parallel lines are due to the crystal lattice. It is remarkable that the lines in both areas have the same orientation; they are oriented diagonal from lower right to upper left. The lattice spacing is measured to approximately (3.3 ± 0.1) Å which corresponds to the (321) plane of the YAG lattice. Convergent beam electron diffraction (CBED) confirmed the crystalline nature of the dark appearing YAG phase. Furthermore, weak Kikuchi diffraction bands could be observed originating from the bright phase (not shown) proving its crystallinity. Point analysis EDS (approximately 20 nm probe size) in the TEM confirmed an enrichment of yttrium in the dark phase. In should be noted that cerium is detected in the YAG phase with minor quantity while an enrichment in the other (bright) phase is observed.

If a thinned ion-milled TEM-sample is placed in the SEM in the way shown in Figure 1, diffraction can be obtained by the conventional EBSD equipment of EDAX (TSL). Also the software (TSL OIM Data Collection) provides the possibility to change the setup to transmission (TEM) mode. [19] Additionally the changed geometry, i.e. distance and angle of the detector screen with respect to the sample (pattern center), has to be taken into account (set up is possible in the software) for reliable indexing of crystal phases. Figure 10 shows a micrograph recorded by the forward scatter detector (FSD) positioned underneath the EBSD screen. The contrast is mainly due to materials contrast, i.e. bright appearing phases have scattered electrons in high angle that reach the sideways FSD (one can assume an analogy to the high-angle annular dark field detector (HAADF) in the scanning TEM). Therefore the hole (generated by ion milling) of the sample on the left side appears black. The sample was placed at a working distance (distance pole piece to sample) of 6 mm. The electron beam is accelerated by 30 kV

with a probe current of ca. 10 nA. A mapping of the sample was not possible because of pronounced drift effects due to charging of the sample in dependence of the step size. However, single point analysis of the bright appearing phase resulted in Kikuchi diffraction patterns that could be indexed reliably (confidence index CI = 0.3) as YAG (ICSD 74607) as shown in the right side of Figure 10. The dark phase gave also weak Kikuchi patterns, however, due to the poor quality, they could not unambiguously be attributed to a known crystal phase.

The thickness of the surface layer is shown in Figure 11 as a function of the annealing time. Within the studied time scale, the thickness increases linearly with time. For both temperatures, a kind of induction time occurs when a fitted line is extrapolated to the intersection with the abscissa. As expected, the higher annealing temperature results in a shorter induction time period. From the slopes of the curves, the crystal growth velocities were calculated. They are $(1.5 \pm 0.1) \times 10^{-9}$ m/s and $(1.7 \pm 0.2) \times 10^{-9}$ m/s for 950 and 1000 °C, respectively. The crystal growth velocity seems hence to be slightly smaller at 950 °C; this variation is, however, within the limits of error.

Figure 12 presents the effect of the annealing time on the size of the seaweed structures. It seems that after approximately 35 h annealing at a temperature of 950 °C and 15 h for 1000 °C, the crystals first grow rapidly with time and then approach smaller and constant crystal growth velocities.

Discussion

The controlled annealing of glasses led to both surface and bulk crystallization. Different crystal phases are observed in the XRD patterns as well as in the micrographs (OM and SEM). The micrographs show that some crystals grow from the surface and another crystal phase with

11

seaweed morphology is formed in the bulk. At an annealing time of 24 h, a third crystal phase with spherulitic shape is identified in the bulk which has a morphology notably different than that of the surface layer (see Figure 2a and b).

In the TEM micrographs as well as in the SEM micrographs an interpenetrating structure is observed at the surface. The EDS-analyses in the TEM as well as the Kikuchi diffraction patterns in the SEM (TKD method) proved the occurrence of YAG as well as of another crystalline phase. For this second crystalline phase, the microanalysis indicates yttrium, silicon as well as cerium. Since XRD clearly shows the formation of α-$Y_2Si_2O_7$, the crystallized surface layer should hence consist of both YAG and α-$Y_2Si_2O_7$. It should be noted that the Kikuchi pattern in Figure 10 could not reliably be indexed with α-$Y_2Si_2O_7$. The first reason is the poor quality of the pattern which contains also artifacts typical for charging. The second reason might be a disturbed crystal lattice with displacement that is different from the ideal α-$Y_2Si_2O_7$. This is in agreement with observation of the poor Kikuchi diffraction in the diffraction pattern obtained by TEM. These two phases form a lamellar structure which is typical for eutectic crystal growth as described in the literature in binary and ternary YAG-systems. [10-12] This eutectic growth is observed in cooled (non-glass forming) liquids with compositions close to the eutectic ones. They might be prepared by complex technical methods providing steep temperature gradients and fast crystal growth. [10] The interspace between the crystal phases should be as small as possible (0.2-10 μm in the systems YAG/ Al_2O_3 and YAG/ yttrium stabilized zirconia) in order to provide advantageous mechanical properties, such as mechanical strengths in the > 1GPa range. [10] In the present study an interspace in the range of 50 nm is obtained after annealing the cast glasses. Furthermore the coupled growth originates from the surface into the bulk leading to a cell structure, i.e. grains with the same orientation as proved in the HRTEM micrograph in Figure 9b.

12

From the cross-section of the samples the growth velocity of the surface crystallization front into the volume was determined. A linear growth of the crystallization front from the surface into the bulk is observed. The independence of the growth velocity from the applied annealing temperature suggests that the growth mechanism is controlled predominantly by the removal of latent heat of crystallization by heat conduction. [21] The seaweed structures in the bulk also grew in diameter with time but go into saturation at a certain point and do not grow with time anymore (see Figure 11and 12). This is characteristic for diffusion controlled growth. The growth of the seaweed crystals also denoted as dense branching is explained in literature by isotropic conditions and large undercoolings. [15-18]

The deceleration in growth velocity with time of this crystals can be explained by a diffusion barrier that is formed around the crystal hindering further growth. The growth velocities of the aluminum enriched crystals decrease with time due to a decrease in the diffusion gradient which is caused by an increasing depth of the diffusion layer. It should be noted that in the past few years in many multi component glasses the formation of a diffusion layer around bulk nucleated crystals has been shown experimentally. In some cases, as in that of the nano crystallization of fluoride crystals from silicate glasses, [20, 22-24] the diffusion layer leads to a nearly total deceleration of crystal growth. [25, 26] The depletion in aluminum around the seaweed crystals goes in parallel with an enrichment in yttrium and silica. This leads to a region which is advantageous for the crystallization of yttrium silicate in the late stage of crystallization. In the same stage, the crystallization of garnet is no longer possible because most of the aluminum is already incorporated into the seaweed crystals. Accordingly, this yttrium silicate phase is observed in the XRD-patterns and additionally proved in the EDS-mapping (see Figure 2 and 8b). In agreement with the EDS-analysis, in the SEM micrographs in Figure 6, bright halos are observed around the seaweed structures. This effect is due to the materials contrast.

13

On the crystallization of the studied system the following conclusions can be drawn: The nucleation of the garnet phase takes place near the surface. A coupled growth with the yttrium silicate phase, mainly α-$Y_2Si_2O_7$, leads to the observed eutectic structure. Most probably the incorporation of Ce^{3+} in YAG gives rise to an intense green fluorescence as shown in Figure 2a while the enrichment of Ce^{3+} in the yttrium silicate phase might lead to quenching effects which are decreasing strongly the fluorescence intensity. [27] The thickness of the crystallized layer is a linear function of time (see Figure 6). At the same time, seaweed crystals are nucleated in the bulk and start to grow. At a distance of 220 μm, the garnet phase is no longer detectable as seen in the fluorescence optical micrographs (Figure 2) and in the SEM-micrographs (Figure 5). Most probably, in that distance from the surface, the seaweed star-shaped crystals are large enough, i.e. the quantity of aluminum removed from the glass composition is high enough, that the crystallization of garnet is no longer preferred due to the lack of appropriate alumina concentrations. If the surface crystallized layer reaches to the aluminum enriched crystals, the crystallization front grows around them until the latter are fully embedded. Then the seaweed crystals cannot continue to grow but relax to an equilibrium form. [28] This easily explains why these crystals are larger at a greater distance from the surface. In the late stage of crystallization the formation of yttrium silicate around the alumina enriched seaweed crystals takes place as observed at an annealing time of 80 h at 950 °C (see Figure 8b).

We are convinced that the further study of eutectic growth of YAG and yttrium silicate at the surface of glass ceramics might lead to new tough materials. In principle, glass-ceramics with a structure composed by a surface layer exhibiting one crystalline phase and a bulk showing another crystalline phase, might also be of interest with respect to the resulting mechanical properties. Such multi component materials might exhibit high strength due to stresses caused by different CTEs and may show a crystalline phase in the bulk which is decisive for the function. Only recently glasses which during annealing give rise to the formation of one

14

crystalline phase at the surface and another one in the bulk have been described in the literature.[29-31] Aditionally the prepared materials may provide advantageous optical properties, e.g. converter materials that convert light of blue light emitting diodes to white light.

Conclusion

Thermal annealing of glasses with the mol% composition 17 Y_2O_3, 33 Al_2O_3, 40 SiO_2, 2 AlF_3, 3 CaO, 2 CeF_3, 3 B_2O_3 at 950 and 1000 °C led to surface nucleation. A surface layer consisting of a lamellar structure composed by yttrium aluminum garnet and α-$Y_2Si_2O_7$ was formed. The thickness of the lamellae was about 50 nm and they were oriented perpendicular to the surface. Simultaneously aluminum seaweed crystals grew in the bulk. The glassy phase around these crystals was depleted in aluminum. In a certain distance from the surface (220 nm at 1000 °C), the crystallization of YAG was no longer observed due to the lack of aluminum. Then only yttrium silicate is formed and is growing into the bulk. The garnet in the surface layer is doped with Ce^{3+} as seen from the intense broadband green-yellow fluorescence.

ACKNOWLEDGMENTS

15

References

[1]   A. Keshavarzi, W. Wisniewski, C. Rüssel,..*ACS Appl. Mater., Interfaces.* 2013, **5**, 8531-8536.

[2]   S. Fujita, S. Tanabe, *Opt. Mater.*, 2010, **32**, *886–890.*

[3]   S. Nishiura, S. Tanabe, S. Fujita, Y. Fujimoto. *Opt. Mater.* 2011, **33**, 688–691.

[4]   A. Tarafder, A. R. Molla, B. Karmakar. *J. Am. Ceram. Soc.* 2010, **93**, 3244–3325.

[5]   A. Keshavarzi, C. Rüssel. *Mater. Chem. Phys.* 2012, **132**, 278-283.

[6]   A. Keshavarzi, W. Wisniewski, C. Rüssel. *CrystEngComm.* 2012, **14**, 6904–6909.

[7]   J. W. P. Schmelzer. In *Nucleation Theory and Applications.* Wiley-VCH, 2005.

[8]   A. Hunger, G. Carl, C. Rüssel. *Solid State Sci.* 2010, **12**, 1570-1574

[9]   M. J. Pascual, L. Pascual, A. Duran, P. Wange, C. Rüssel. *Glastech. Ber. Glass. Sci. Technol.* 2002, **75**,69-74.

[10]   T. A. Parthasarathy, Tai-Il. Mah, L.E. Matson. *J. Am. Ceram. Soc.*1993,**76**, 29-33.

[11]   B. P. Bewlay, K. Dovidenko. *Microsc. Microanal.*2004, **10**,706-707.

[12]   J. LLorca, V. M. Orera. *Progress Mater. Sci.*2006, **51**, 711–809.

[13]   V. M. Fokin, E. D. Zanotto, N. S. Yuritsyn, J. W. P. Schmelzer. *Non-Cryst. Solids.* 2006, **352**, 2681-2714.

[14]   P. Trimby. W.Ultramicroscopy. 2012, **120**,16-24.

[15]   B. Utter, E. Bodenschatz. Phys. Rev.E. 2005 , **72**, 11601-116016

[16]   I. Stalder, H. J. Bilgram. Europhys. Lett. 2001, **56**, 829–835.

[17]   T. Ihle, H. Müller-Krumbhaar. *Phys. Rev. Lett.*1993, **70**, 3083-3086

[18]   E. Ben-Jacob, P. Garik. *Nature*, 1990, **343**, 523–530.

[19]   R. A. Schwarzer. Ultramicroscopy. 1997, **67**, 19-24

[20]   V. S. Raghuwanshi, A. Hoell, C. Bocker, C. Rüssel. *CrystEngComm*. 2012, **14**, 5215–5223.

[21]   A. Marotta, A. Buri, F. Branda, S. Saiello. Nucleation and Crystallization of Li_2O. $2SiO_2$-a DTA Study. In *Advances in Ceramics, Nucleation and Crystallization in Glasses;* J. H. Simmons, D. R. Uhlmann, G. H. Beall. Eds.; American Ceramic Society: Westerville, OH, 1982; pp 146-152.

[22]   S. Bhattacharyya, C. Bocker, T. Heil, J. R. Jinschek, T. Höche, C. Rüssel, H. Kohl. *Nano Lett.* 2009, **9**, 2493-2496.

[23]   R. P. F. de Almeida, C. Bocker, C. Rüssel. *Chem. Mater.* 2008, **20**, 5916–5921.

[24]   C. Bocker, I. Avramov, C. Rüssel. *J. Eur. Ceram. Soc.* 2011, **31**, 2861-2866.

[25]   C. Bocker, S. Bhattacharya, T. Höche, C. Rüssel. *Acta. Mater.* 2009, **57**, 5956-5963.

[26]   P. Argyrakis, I. Avramov, C. Bocker, C. Rüssel. *Europhys. Lett.* 2010, **89**, 18004.

[27]   L. G. Vanuiter, L. F. Johnson. *J. Chem. Phys.*, 1966, 44, 3514-3522.

[28]   Y. Saito. Pattern formation of a crystal growing in a diffustion field. In *Advances in the Understanding of Crystal Growth Mechanisms;* T. Nishinaga, K. Nishioka, J. Harada, A. Sasaki, H. Takei, Eds, Elsevier: Amsterdam, 1999; pp 47-60.

[29]   A. Keshavarzi, W. Wisniewski, R. de Kloe, C. Rüssel. *CrystEngComm*. 2013, **15**, 5425–5433

[30]   W. Wisniewski, B. Schröter, T. Zscheckel, C. Rüssel. *Cryst. Growth Des.* 2012, **12**, 1586-1592.

[31]   R. Müller, E. D. Zanotto, V. M. Fokin. *J. Non-Cryst. Solids.* 2000, **274**, 208-231.

17

[32]   E. D. Zanotto. *J. Non-Cryst. Solids.* 1991, **129**, 183-190.

Figure Captions

Figure 1   Scetch of the setup in the SEM-chamber for obtaining transmission Kikuchi diffraction pattern and inserted the photo of the sample holder.

Figure 2.   (A) Laser scanning microscopy of sample annealed at 1000 °C for 24 h. (B) fluoresent optical image of sample. The yellowish layers are Ce^{3+}-doped YAG crystals.

Figure 3.   XRD-patterns of samples annealed at 950 °C for different periods of time.

Figure 4.   XRD-patterns of samples annealed at 1000 °C for 48 or 72 h. From both samples, the surface layer has been removed and further XRD-patterns were recorded.

Figure 5   SEM micrographs of samples annealed at 950 °C for 24, 48, 60 and 80 h.

Figure 6.   SEM micrographs of samples annealed at 1000 °C for 24 (image b), 48 (images c) and 72 h (image d). Image (a) has a higher sample magnification than image (b) and is recorded near the border of the surface crystallized YAG layer and the residual inner glass matrix.

Figure 7   SEM micrographs from a slope-cut prepared from the sample which was annealed at 1000 °C for 24 h. The image (b) shows a micrograph with a higher magnification, recorded from the cross-section.

Figure 8   a) EDS-maps around a seaweed structure in sample annealed at 950 °C for 80 h. The scale (right) gives the relative aluminum concentration. The map was recorded using an acceleration voltage of 6 kV.
b) EDS-Map shows around a seaweed structure annealed at 1000 °C for 24 h silicon, and aluminum mapping.

19

Figure 9   a) the bright-field TEM micrographs of the sample annealed at 1000 °C for 24 h. b)
            TEM micrograph in a higher magnification.

Figure 10   Left: SEM-micrograph recorded by the forward scatter detector (FSD) positioned
            underneath the EBSD screen. Right: Kikuchi patterns recorded from the phase of
            dark appearance (top) and of the phase with bright appearance (bottom).

Figure 11   The thickness of the surface crystallized YAG layer of samples annealed at 950 °C
            and 1000 °C for different periods of time.

Figure 12   The crystal size of the aluminum enriched phase as a function of annealing time.
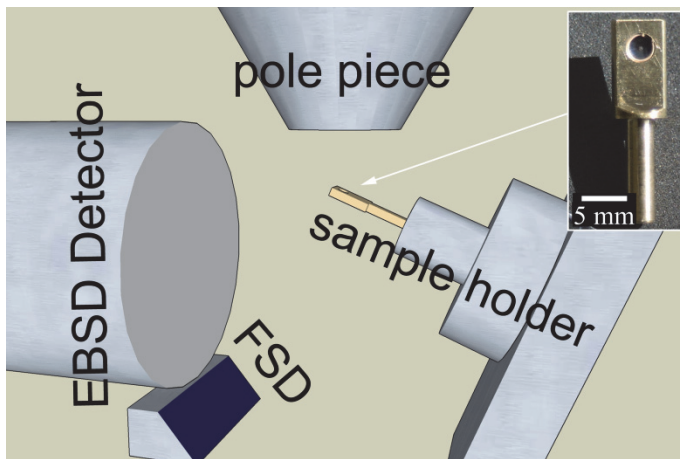
Figure 1.
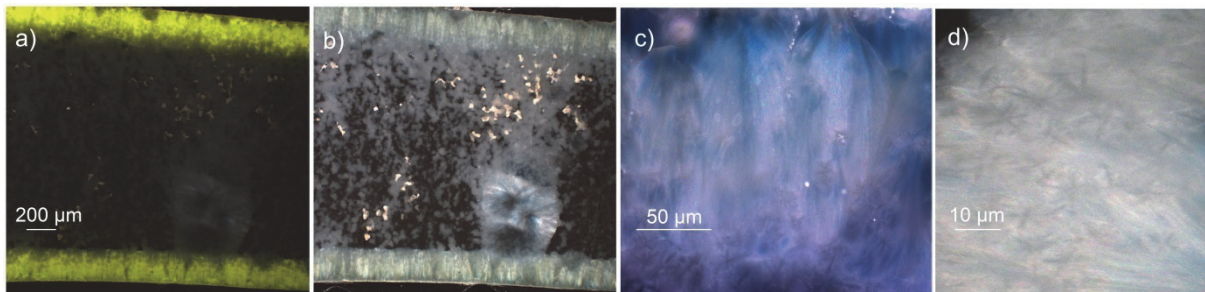
Figure 2.
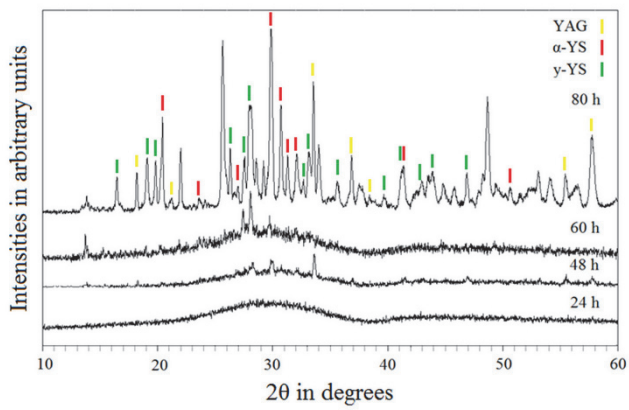
Figure 3.
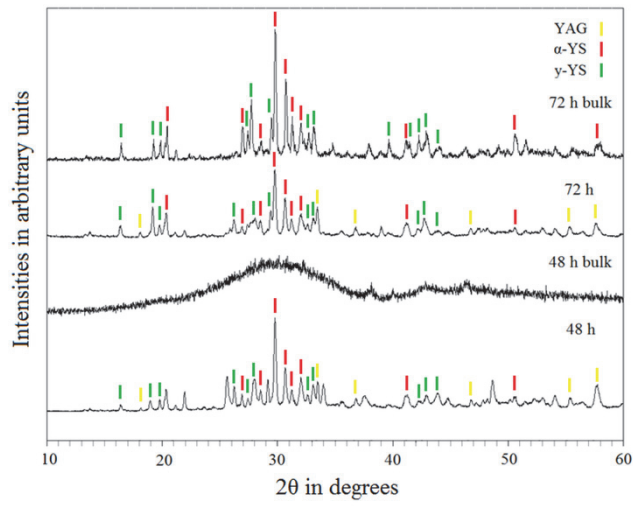
Figure 4.
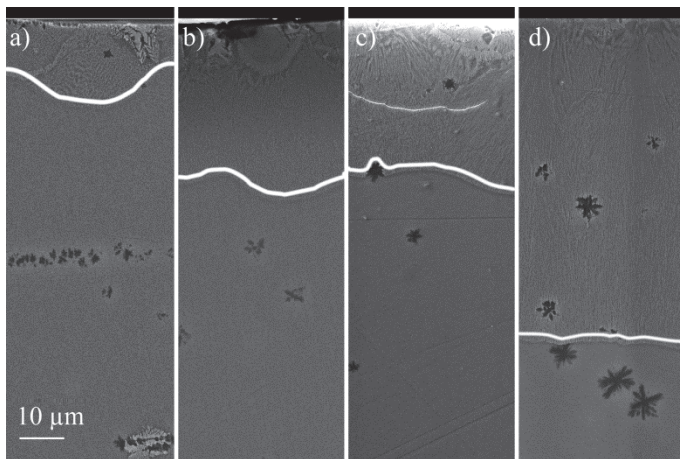
Figure 5.
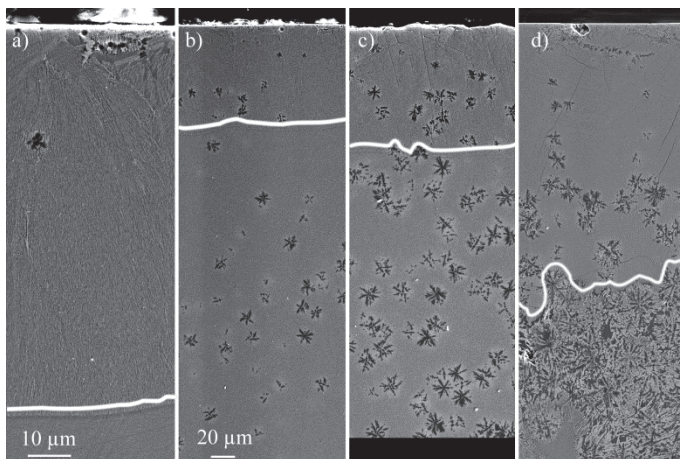
Figure 6.
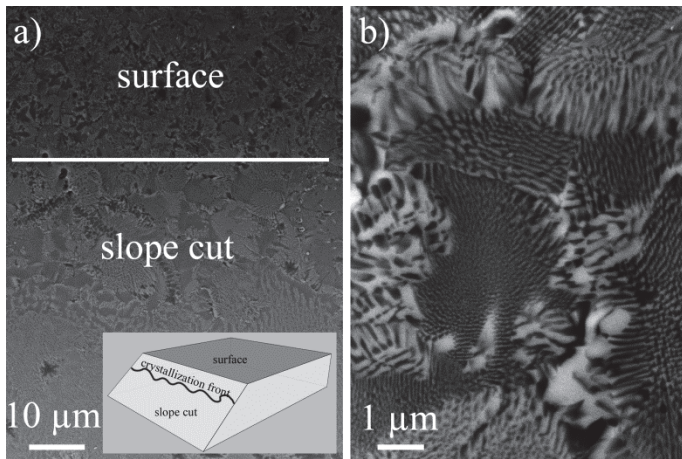
Figure 7.
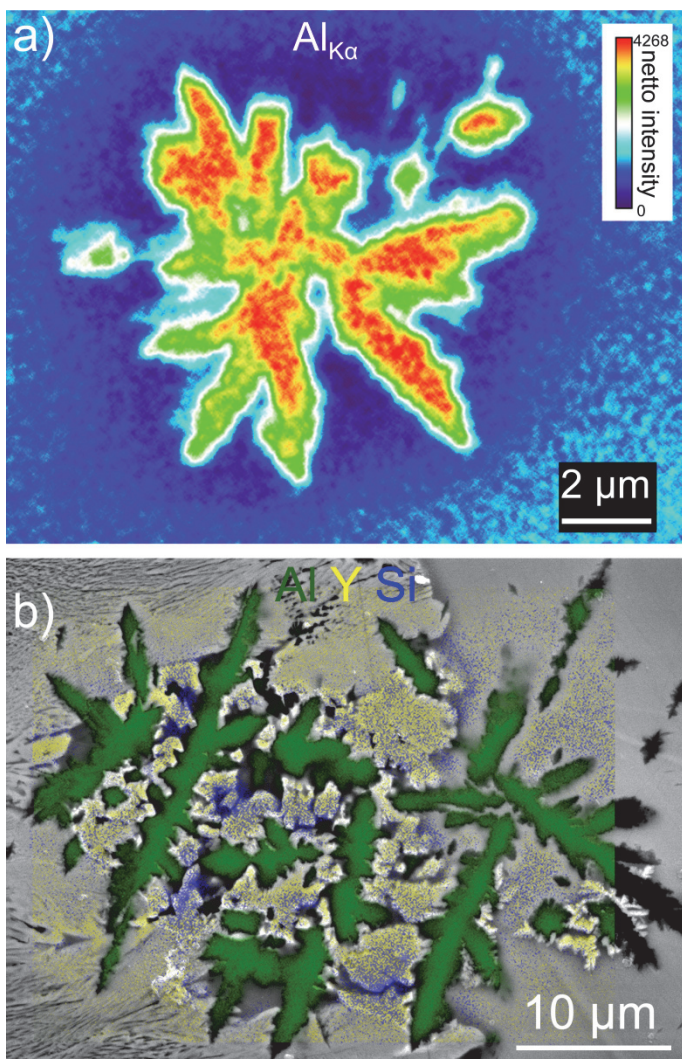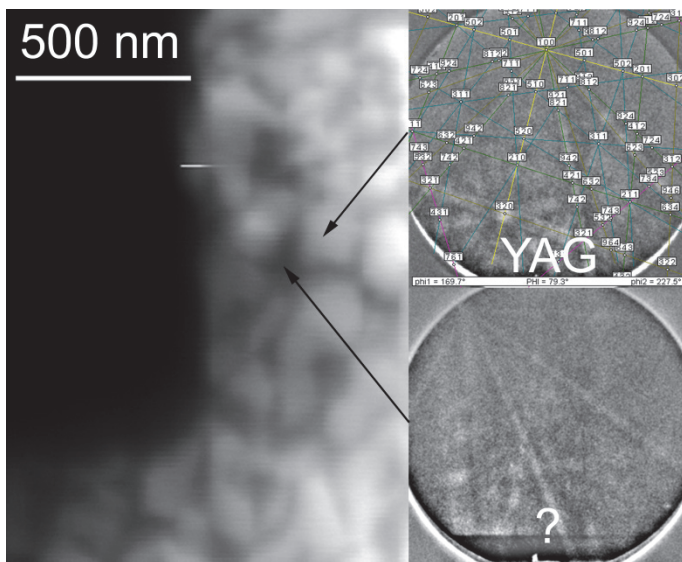

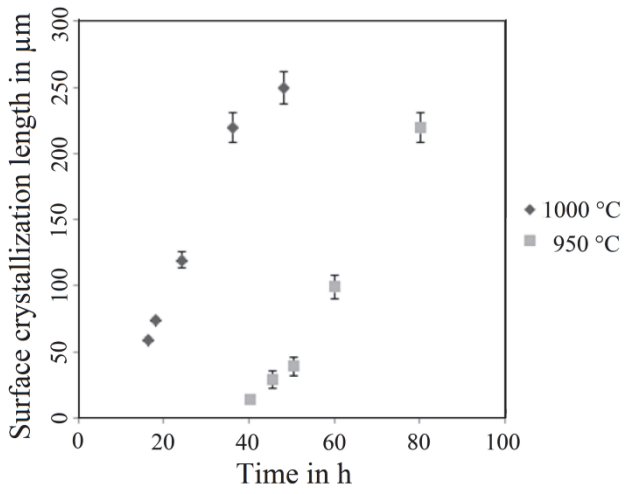**Figure 8.**
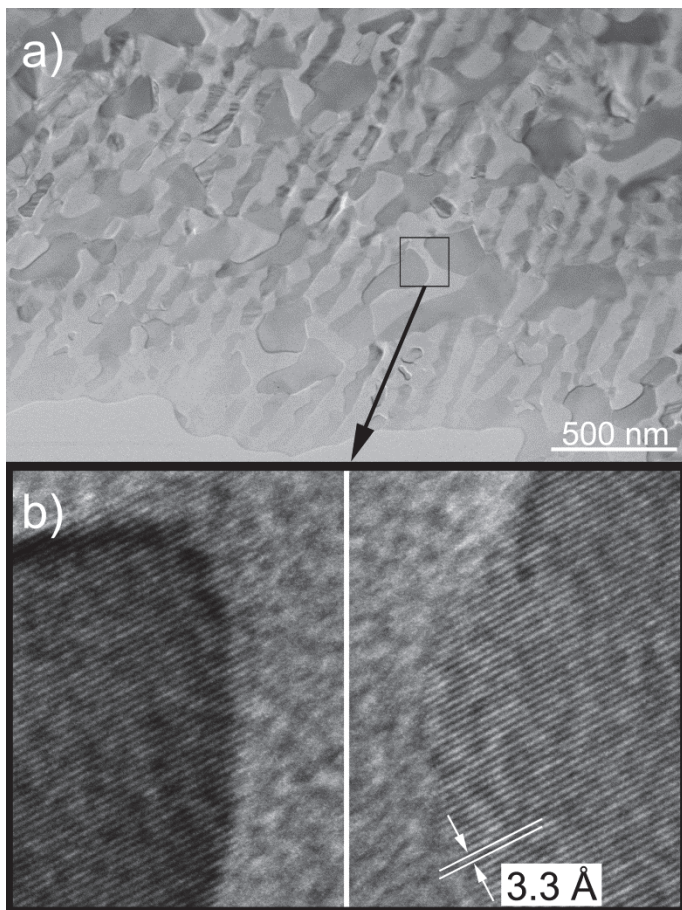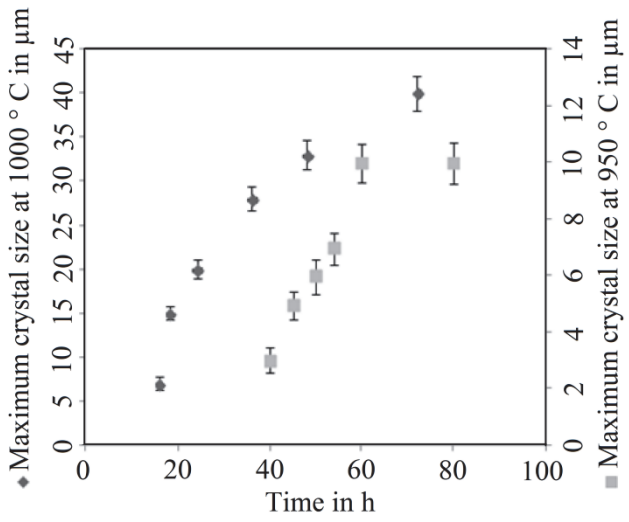
Figure 9.

Figure 10.

Figure 11.

Figure 12.

6. Conclusion

The interest in yttrium aluminosilicate glass and glass-ceramics was stimulated because they are promising candidates for the development of translucent YAG glass-ceramics suitable for converting blue light of LEDs to white light. The properties of these glass-ceramics may be widely modified by adding additives. In analogy the phases formed during the crystallization process may strongly be affected by the chemical composition of the glass, including minor components. One promising glass composition is the system $Y_2O_3/Al_2O_3/SiO_2$ which thermal treatment resulted in the crystallization of YAG. Here, for the crystallization process, comparably high temperatures are required, which lead to comparably large crystals. Lower crystallization temperatures can be verified by optimizing the glass compositions. This may be achieved by tailored proportions of Y_2O_3, Al_2O_3 and SiO_2 or by components which decrease the viscosity as well as the glass transition temperature.

In the present work, B_2O_3, AlF_3, Na_2O or CaO were used to reduce the viscosity, while ZrO_2 and TiO_2 were chosen for inducing the nucleation and subsequently the crystal growth velocity. Adding of these substances, however, also led to changes in the crystallization mechanism. For example 5 mol% of ZrO_2 and TiO_2 induce volume crystallization of the glass, while the addition of small amounts of CaO and Na_2O led to nucleation and subsequent crystal growth at the surface as well as in the bulk.

Bulk crystallization

The addition of ZrO_2 and TiO_2 to the $Y_2O_3/Al_2O_3/SiO_2$ glass and subsequent thermal treatment at temperatures above T_g led to the formation of crystalline phases among them YAG. Other phases might also be formed in minor concentrations. For instance, the addition of 5 mol% ZrO_2 and subsequent heat treatment at 1250 °C results in the formation of YSZ as the first phase to crystallize which triggers the crystallization of YAG. This is proved by the observation that the ZrO_2 crystals are enclosed in the YAG phases. In some compositions, α-Al_2O_3 is formed as the second crystalline phase because the YSZ crystals inside the alumina crystals are obviously smaller than those enclosed in the YAG crystals and the residual glass. The YAG crystallized as the third phase because it incorporates larger YSZ crystals and finally, the yttrium silicates nucleate on the surfaces of both α-Al_2O_3 and YAG. They were the last phases to crystallize, possibly during cooling the sample at the end of the annealing process. If ZrO_2 and TiO_2 were incorporated in a glass both at the same time, the YAG and

the yttrium silicate crystallized simultaneously at a temperature $\geq$ 1150 °C for 20 h; YSZ appeared as third phase.

If only CaO with concentrations in the range from 10 to 40 mol% was added to the $Y_2O_3/Al_2O_3/SiO_2$ system, YAG crystallized in the bulk as a dendritic phase with different morphologies when the glass was thermally treated at 1200 °C for 6 h. While the samples with 20 and 30 mol% CaO were composed of many dendrites, samples with 10 and 40 mol% contained only very few, but very large dendrites, indicating a significant effect of CaO on the nucleation rate and crystal growth velocity in the glasses.

Surface Crystallization

Samples containing some fluorid, some boron oxide as well as 3 mol% CaO or Na_2O, however, showed surface crystallization. Although the chemical compositions of the samples were fairly similar, two different mechanisms controlled the crystallization process. While in CaO containing samples, glass-ceramic with lamellar structures composed of eutectic YAG and yttrium silicate ocurred, in glass containing Na_2O, the YAG crystals nucleated at the surface of the glass and grew into the bulk during thermal treatment. Simultaneously, star-shape crystals composed of alumina were formed in the bulk. Subsequent layers of yttrium silicates with the composition $Y_2Si_2O_7$ (monoclinic and orthorhombic) were formed adjacent to the YAG and grew around the existing star-shaped crystals. Additionally bulk nucleation of the orthorhombic YS and different monoclinic YS phases was observed.

In the literature glass-ceramics with a structure composed by a surface layer exhibiting one crystalline phase and the bulk showing another crystalline phase have up to now not been reported in the literature.

7. Reference

1. G. Blasse, A. Brill: A new phosphor for flying-spot cathode-ray tubes for colour television: Yellow-emitting, $Y_3Al_5O_{12}$: Ce^{3+}, *App. Phys. Lett.* **1967**, *11*, 53–55.

2. R.C. Ropp: The Chemistry of Artificial Lighting Devices, Amsterdam, London, New York: Elsevier Science Puishing, 1993.

3. R.C. Ropp: Luminescence and the Solid State, Amsterdam, New York: Elsevier Science Publishing, 1991.

4. C.W. Wessner: Partnership for solid-state lighting, Washington, National Academy Press, 2002.

5. M. Fadhali: Advanced Photonic Sciences, InTech, online book 2012.

6. J. E. Geusic, H. M. Marcos, V. U. L. G: Laser oscillations in Nd-doped yttrium aluminum, yttrium gallium, and gadolinium garnets. *App. Phys. Lett*. **1964**, *4*, 182–184.

7. D. J. Krebs, A-M. Novo-Gradac, S. X. Li, S. J. Lindauer, R. S. Afzal, A. W. Yu: Compact, passively Q-switched Nd:YAG laser for the MESSENGER mission to Mercury. *Appl. Opt*. **2005**, *44*, 1715-1718.

8. Y.H. Zhou, J. Lin, S.B. Wang, H.J. Zhang: Preparation of $Y_3Al_5O_{12}$: Eu^{3+} phosphors by citric–gel method and their luminescent properties. *Opt. Mater*. **2002**, *20*, 13–20.

9. J. F. Shackelford, R. H. Doremus: Ceramic and Glass Materials, Structure, Properties and Processing, Springer, New York, 2008.

10. Lei. Chen, C-C. Lin, C-W. Yeh, R-S. Liu: Light Converting Inorganic Phosphors for White Light-Emitting Diodes. *Materials*, **2010**, *3,* 2172-2195.

11. P. W. Brittenham, M. P. Vittitow: BASIC RESEARCH NEEDS FOR SOLID-STATE LIGHTING. Report of the Basic Energy Sciences Workshop on Solid-State Lighting, 2006.

12. D. Lu, C.P. Wong: Materials for Advanced Packaging, Springer, New York, 2009**.**

13. F. M. Steranka, J. Bhat, D. Collins, L. Cook, M. G. Craford, R. Fletcher, N. Gardner, P. Grillot, W. Goetz, M. Keuper, R. Khare, A. Kim, M. Krames, G. Harbers, M. Ludowise, P. S. Martin, M. Misra, G. Mueller, R. Mueller-Mach, S. Rudaz, Y. C. Shen, D. Steigerwald, S. Stockman, S. Subramanya, T. Trottier, J. J. Wierer: High power LEDs – Technology status and market applications, *Physica Status Solidi* (A), **2002**, *194*, 380–388.

14. S. Fujita, Y. Umayhara, S. Tanabe: Influence of light scattering on luminous efficacy in Ce:YAG glass-ceramic phosphor. *J CERAMIC SOC JPN*. **2010** ,*118*, 128-131.

15. I. A. Bondar, F. Y. Galakhov: PHASE EQUILIBRIA IN THE SYSTEM Y_2O_3–Al_2O_3–SiO_2. Izv. Akad. Nauk SSSR, Ser. Khim. **1964**, *7*, 1325-1326.

16. D. R. Messier: Preparation and Crystallization of Si-Y-A1-O-N Glasses. *Ceram. Eng. Sci. Proc.* **1982**, *3,* 565-576.

17. R. E. Loehmm: Preparation and Properties of Yttrium-Silicon-Aluminum Oxynitride Glasses, *J. Am. Ceram. Soc.* **1979**, *62,* 491-94.

18. G. Thomas, C. Ahn, J. Weiss: Characterization and Crystallization of Y-Si-Al-O-N Glass. *J. Am. Ceram. Soc.* **1982**, *65*, 185-188.

19. R. E. Loehman: Preparation and Properties of Yttrium-Silicon-Aluminum Oxynitride Glasses, *J.Am.Ceram.Soc.* **1979**, *62,* 491-494.

20. R. E. Loehman, D. J. Rowcliffe: Sintering of Si_3N_4-Y_2O_3-Al_2O_3, *J, Am.Ceram.Soc.* **1980**, *63*, 144-48.

21. R. E. Loehman: Oxinitride Glasses, *J. Non-Crys.Solids*, **1980**, *42*, 433-446

22. C. C. Ahn, G. Thomas: Microstructure and Grain-Boundary Composition of Hot-Pressed Silicon Nitride With Yttria and Alumina, *J. Am. Ceram .Soc.* **1983**, *66,* 14-17.

23. S. Hampshire, R. A. L. Drew, K. H. Jack: Viscosities, Glass Transition Temperatures, and Microhardness of Y-Si-Al-O-N Glasses, *J. Am. Ceram. Soc.* **1984**, *67*, 46-47.

24. G. Leng-Ward, M. H. Lewis: Crystallization in Y-Al-O-N Glasses, *Mater. Sci. Eng,***1985**, *71*, 101-111.

25. C. O'Meara, G. L. Dunlop, R. Pompe: Phase Relationships in the System SiO_2-Y_2O_3-Al_2O_3, High Tech Ceramics, ed. P.Vincenzini, Elsevier Science Publishers B.V., Amsterdam, 1987.

26. C. O'Meara, G. L. Dunlop, R. Pompe: Formation, crystallisation and oxidation of selected glasses in the Y-Si-Al-O-N system, *J. Eur. Ceram. Soc.* **1991**, *8,* 161-170.

27. I. H. Arita, D. S. Wilkinson, G. R. Purdy: Crystallisation of Yttria-Alumina-Silica Glasses, *J. Am. Ceram. Soc.* **1992**, *75*, 3315-3320.

28. M. M. Chadwick, D. S. Wilkinson: Microstructural Evolution in Annealed and Crept Silicon Nitride, *J. Am. Ceram. Soc.* **1990**, *76*, 376–384.

29. T. R. Dinger, R. S. Rai, G. Thomas: Crystallisation behaviour of a glass in the Y_2O_3-SiO_2-AlN-system, *J. Am. Ceram. Soc.* **1988**, *71*, 236-244.

30. J. L. Besson, H. Lemercier, T. Rouxell, G. Trolliard: Yttrium sialon glasses: Nucleation and crystallisation of $Y_{35}Si_{45}Al_{20}O_{38}N_{17}$. *J. Non-Cryst.Solids.* **1997**, *211*, 1-21.

31. Z. Jin, Q. Chen: An assessment of the $AlO_{1.5}$-$YO_{1.5}$ system, *CALPHAD,* **1995**, *19*, 69-79.

32. J. Gröbner, Konstitutionsberechnungen im System Y-Al-Si-C-O. Dissertation, Universität Stuttgart (1994).

33. S. Hampshire: Oxynitride glasses and glass ceramics. *Mater. Res. Soc. Symp. Proc*. **1993**, *287,* 93-103.

34. S. Hampshire, R. A. L. Drew, K. H. Jack: Viscosities, Glass Transition Temperatures, and Microhardness of Y-Si-Al-O-N Glasses, *J* . *Am. Ceram. Soc*, **1984**, *67*, 46-47.

35. M. J. Hyatt, D. E. Day: Glass properties in yttria-alumina-silica system. *J. Am. Ceram. Soc.* **1987**, *70*, 283-287.

36. T, Höche, M. Mäder, S. Bhattacharyya, G. S. Henderson, T. Gemming, R. Wurth, C. Rüssel, I. Avramov: $ZrTiO_4$ crystallization in nanosized liquid–liquid phase-separation droplets on glass—a quantitative XANES study. *CrystEngComm*. **2011**, *13*, 2550-2556.

37. T. Höche, C. Patzig, T. Gemming, R. Wurth, C. Rüssel, I. Avramov: Temporal Evolution of Diffusion Barriers Surrounding $ZrTiO_4$ Nuclei in Lithia Aluminosilicate Glass-Ceramics. *Crystal Growth & Design*, **2012**, *12*, 1556–1563.

38. P. Wange, T. Höche, C. Rüssel, J. D. Schnapp: Microstructure-property relationship in high-strength MgO–Al_2O_3–SiO_2–TiO_2 glass-ceramics. *J. Non-Crys. Solids*, **2002***, 298*, 137-145.

39. A. Hunger, G. Carl, A. Gebhardt, C. Rüssel: Ultra-high thermal expansion glass–ceramics in the system MgO/Al_2O_3/TiO_2/ZrO_2/SiO_2 by volume crystallization of cristobalite. *J. Non-Crys. Solids*, **2008**, *354*, 5402-5407.

40. A. Hunger, G. Carl, A. Gebhardt, C. Rüssel: Young's moduli and microhardness of glass–ceramics in the system MgO/Al_2O_3/TiO_2/ZrO_2/SiO_2 containing quartz nanocrystals, **2010**, *122*, 502-506.

41. W. Braue, G.Wotting, G. Zeigler: Devitrification effect of grain boundary phases on high temperature strength of sintered S&N, materials. In *Ceramic Materiafs and Components for Engines,* eds W. Bunk & H. Hausner. Verlag Deutsche Keramische Gesellschaft, Bad Honnef, 1986.

42. Y. Cheng, D. P. Thompson: Nitrogen containing tetragonal zirconia. J. *Am. Ceram. Soc.* **1991***, 74,* 1135-1138.

43. D. A. Bonell, T. Y. Tien, M. Ruhle: Controlled crystallization of the amorphous phase in silicon nitride ceramics. *J. Am. Ceram. Soc.* **1987***, 70,* 460-465.

44. H. Hohnke, T. Y. Tien: Solid-liquid reactions in part of the system Si, Al, Y/ N, O: Progress in Nitrogen Ceramics Process. F. L. Riley. Martinus Nijhoff, The Hague, 1983.

45. L. D. Bentsen, D. P. H. Hasselman, T. Y. Tien: Effect of crystallization of the grain boundary phase on the thermal diffusivity of a sialon ceramic. *J. Am. Ceram. Soc.* **1984**, *67*, 85-86.

46. J. Zhao, L. Wang, G. Peng, J. G. Wu: Effect of zirconia on the crystallization of grain boundary. In Proceedings of the 4th International Symposium on Ceramic Materials and Components for Engines, Gothenburg, Sweden, 1990.

47. C. H. Drummond: Glass formation and crystallization in high-temperature glass-ceramics and Si_3N_4. *J. Non-Crys. Solids*. **1990**, *123*, 114-128.

48. P. Vomacka, O. Babushkin: Yttria-Alumina-Silica Glasses with Addition of Zirconia, *J. Europ. Ceram. Soc.* **1995**, *15*, 921-928.

49. P. Vomacka, O. Babushkin, R. Warren: Zirconia as a nucleating agent in an yttria-alumina-silica glass. *J. Eur. Ceram. Soc.* **1995**, *15*, 1111-1117.

50. P. Vomacka, R. Ramesh, S. Hampshire: Influence of Zirconia Addition on the Crystallization Kinetics of a Y-Si-Al-O-N Glass. *J. Eur. Ceram. Soc.* **1996**, *16*, 1253-1262.

51. P. Vomacka, D. S. Wilkinson: Influence of ZrOz Addition on Melting Kinetics of a YSiAlO Glass-Ceramic.*J. Eur. Ceram. Soc.* **1996**, *16*, 1245-1251.

52. U. Kolitsch, H.J. Seifert, F. Aldinger: Phase relationships in the systems RE_2O_3-Al_2O_3-SiO_2 (RE = Rare earth elements, Y, and Sc). *J. Phase Equilibria*. **1998**, *19*, 426-433.

53. U. Kolitsch, H. J. Seifert, T. Ludwig, F. Aldinger; Phase equilibria and crystal chemistry in the Y_2O_3-Al_2O_3-SiO_2 system, *J. Mater. Res.* **1999**, *14*, 447-455.

54. L. Matsubara, M. Paranthaman, S. W. Allison, M. R. Cates, D. L. Beshears, D. E. Holcomb: Preparation of Cr-Doped $Y_3Al_5O_{12}$ Phosphors by Heterogeneous Precipitation Methods and Their Luminescent Properties. *Mater. Res. Bull.* **2000**, *35*, 217-224.

55. S. Kochawattana: Phase Formation and Sintering of YAG Ceramics, Doctral dissertation, College of Earth and Mineral Sciences, The Pennsylvania State University, 2007.

56. T. Noguchi, M. Mizuno: Liqudius curve measurments in the system yttrium oxide-aluminum oxide, *Kogyo Kagaku Zasshi*, **1967**, *70*, 834-839.

57. M. Aparicio, R. Moreno, A. Duran: Colloidal Stability and Sintering of Yttria-Silica and Yttria-Silica-Alumina Aqueous Suspensions. *J. Eur. Ceram. Soc.* **1999**, *19*, 1717-1724.

58. A. I. Becerro, M. Naranjo, M. D. Alba, J. M. Trillo: Structure-directing effect of phyllosilicates on the synthesis of y-$Y_2Si_2O_7$. Phase transitions in $Y_2Si_2O_7$. *J. Mater. Chem*. **2003**, *13*, 1835–1842.

59. J. Iro, H. Johnson: Synthesis and study of yttrialite. *Am. Mineral*. **1968**, *53*,1940-1952.

60. A. I. Becerro, M. Naranjo, M. D. Alba, J. M. Trillo: Structuredirecting effect of phyllosilicates on the synthesis of y-$Y_2Si_2O_7$. Phase transitions in $Y_2Si_2O_7$. *J. Mater. Chem.* **2003**, *13***,** 1835- 1842.

61. S. Kumar and C. H. Drummond: Crystallization of various compositions in the Y_2O_3-SiO_2 system. *J. Mater. Res*. **1992**, *7***,** 997-1003.

62. I. MacLaren, G. Richter. The structure and possible origins of stacking faults in gamayttrium disilicate. *Philos. Mag*. **2009**, *82*, 168-181.

63. K. Liddell, D. P. Thompson: Preparation of new oxynitride glass-ceramics by controlled heat-treatment schedules. *Brit. Ceram. Trans*. **1998**, *97*, 155-161.

64. N. I. Leonyuk, E. L. Belokoneva, G. Bocelli, L. Righi, E. V. Shvanskii, R. V. Henrykhson, N. V. Kulman, D. E. Kozhbakhteeva: High-temperature crystallization and X-ray characterization of Y_2SiO_5, $Y_2Si_2O_7$ and $LaBSiO_5$. *J. Cryst. Growth*. **1999**, *205*, 361-367.

65. J.Felsche: The Crystal Chemistry of the Rare Earth Silicates. *Struct. Bond*. **1973**, *13*, 99-197.

66. N. A. Toropov: Some rare earth silicates. Int. Ceram. Congr., 7th, London, United Kingdom. 1960, 435-442.

67. K. Kunze, S. Wright, B. Adams, D. Dingley, Advances in automatic EBSP single orientation measurements. *Textures and Microstructures*, **1993**, *20*, 41–54.

68. C.D. Barrie, A. P. Boyle, N. J. Cook, D. J. Prior: Pyrite deformation textures in the massive sulfide ore deposits of the Norwegian Caledonides, *Tectonophysics*, **2010**, *483*, 269-286.

69. R. Keding, C. Rüssel: Oriented Crystallisation of Fresnoite in an Electric Field, *Ber. Bunsenges. Phys. Chem.* **1997**, *100,* 1515-1518.

70. G. von der Gönna, R. Keding, C. Rüssel: Oriented growth of mullite from a glass melt using electrochemical nucleation *J. Non-Cryst. Solids,* **1999**, *243*, 109-115.

71. W. Wisniewski, M. Nagel, G. Völksch and C. Rüssel: Electron Backscatter Diffraction of Fresnoite Crystals Grown from the Surface of a 2 BaO · TiO2 · 2.75 SiO$_2$ Glass. *Cryst. Growth Des.*, **2010**, *10*, 1414- 1418.

72. W. Wisniewski, M. Nagel, G. Völksch and C. Rüssel: New Insights into the Microstructure of Oriented Fresnoite Dendrites in the System Ba$_2$TiSi$_2$O$_8$-SiO$_2$ Through Electron Backscatter Diffraction (EBSD). *Cryst. Growth Des.***2010**, *10*, 1939-1945.

73. W. Wisniewski, T. Zscheckel, G. Völksch, C. Rüssel: Electron Backscatter Diffraction of BaAl$_2$B$_2$O$_7$ Crystals Grown from the Surface of a BaO · Al$_2$O$_3$ · B$_2$O$_3$ Glass. *CrystEngComm.* **2010**, *12*, 3105-3111.

74. W. Wisniewski, G. Völksch, C. Rüssel: The Degradation of EBSD-Patterns as a Tool to Investigate Surface Crystallized Glasses and to Identify Glassy Surface Layers. *Ultramicroscopy,* **2011**, *111*, 1712-1719.

75. A. J. Wilkinson, P. B. Hirsch: Electron diffraction based techniques in scanning electron microscopy of bulk materials. *Micron,* **1997**, *28*, 279–308.

76. V. Randle: Electron backscatter diffraction: Strategies for reliable data acquisition and processing, *Mater. Charact.* **2009**, *60*, 913-922.

8. Abbreviations

μg	micro gravity
d_{hkl}	lattice plane spacing
DTA	differential thermal analysis
EBSD	electron backscatter diffraction
EBSP	electron backscattering pattern
EDX	energy dispersive X-ray spectroscopy
FM	fluorescence optical microscope
HAADF	high-angle annular dark detector field
ICSD	Inorganic Crystal Structure Database
IPF	inverse pole figure
IQ	image quality
JCPDS	Joint Committee on Powder Diffraction Standard
LED	light emitting diode
LSM	laser scanning microscope
n	diffraction order
OIM	orientation image mapping
PF	pole figure
SEM	scanning electron microscope
TEM	transmition electron microscop
XANES	X-ray absorption nearedge structure spectroscopy
XRD	X-ray diffraction
YAG	yttrium aluminum garnet
YS	ytrrium silicate
λ	wavelength

9. Presentations

9.1 "Effects of nucleation agents on crystallization of yttrium aluminosilicate glass"

Otto Schott Institut, Jena University (2011)

9.2 "Effects of CaO on microstructure of glass-ceramics from an Oxide Melt in the System $SiO_2/Al_2O_3/Y_2O_3/CaO$"

Otto Schott Institut, Jena University (2011)

9.3 "Surface crystallization of yttrium aluminum garnet from a glass melt in the system $SiO_2/Al_2O_3/Y_2O_3/CaO/B_2O_3/AlF_3$"

Otto Schott Institut, Jena University (2012)

9.4 "Microcharacterization of multiphase glass-ceramic from yttrium aluminosilicate glass"

Otto Schott Institut, Jena University (2013)

9.5 "Crystallization and microcharacterization of yttrium aluminosilicate Glasses"

Otto Schott Institut, Jena University (2013)

10. Posters

10.1 A. Keshavarzi , C. Rüssel, Crystallization of Yttrium Aluminum Garnet (YAG) in Oxyfluoride Glasses of the System SiO_2 /Al_2O_3/Y_2O_3/ZrO_2/AlF_3, in *Crystallization 2012* Conference, Goslar, Germany.

10.2 A. Keshavarzi, C. Bocker, M. Müller and C. Rüssel, Experimental Evidence of a Diffusion Zone Around Crystals in YAG Glass-Ceramics by EDS Microanalysis, in EMAS(*European Microbeam Analysis Society*) 2013 Conference, Porto, Portugal.

11. Acknowledgements

12. Statement

I hereby state that this thesis has not been previously submitted to any university to initiate the conferral of a doctorate. All content obtained from references is marked and the references have been denoted.

Jena, the 26.th of May 2014

Ashkan Keshavarzi

Erklärung

Ich erkläre, dass ich die vorliegende Arbeit selbständig und unter Verwendung der angegebenen Hilfsmittel, persönlichen Mitteilungen und Quellen angefertigt habe.

Jena, den 26. Mai 2014

Ashkan Keshavarzi

13. Curiculum Vitae

Personal data

Name: Ashkan keshavarzi

Birth date: 22.09.1976

Adresse: Fritz-Ritter 8, 07747 Jena

Telefon: 036415510608

E-Mail: ashkan.keshavarzi@uni-jena.de

School

1982-1987	Weysi Elementary School, Shiraz
1987-1990	Taheri High School, Mashhad
1990-1994	Farrazi High School, Mashhad

University

1995-2000   Bachelor of Applied Chemistry, Ferdowsi University of Mashhad

2000-2007   Expert of Laboratory in Part Lastic Group.

2007-2009   Master of Science in Materials Chemistry

2010-present   PhD candidate in Otto-Schott-Institut

Awards

2011   Landesgraduiertenstipendien Ph.D Fellowship

2007   M.Sc. Graduate Research Fellowship (GRF) from Malaysia Ministry of science.

Publications

A. Keshavarzi, C. Bocker and C. Rüssel. Nano Lamellae Composed of Yttrium Aluminum Garnet and Yttrium Silicate by Surface Crystallization of Glass. *CrystEngComm*. (Submitted)

A. Keshavarzi, W. Wisniewski, C. Rüssel. EBSD and EDX Analyses of a Glass-Ceramic Multi Phase Obtained by Crystallizing an Yttrium Aluminosilicate Glass. *ACS Appl. Mater. Interfaces*. **DOI:** 10.1021/am401953j

A. Keshavarzi, W. Wisniewski, R. D. Kloe, C. Rüssel. Surface Crystallization of Yttrium Aluminum Garnet from a Silicate Glass. *CrystEngComm*. **15**, 2013, 5425-5433. **DOI:** 10.1039/C3CE40439K

A. Keshavarzi, W. Wisniewski and C. Rüssel. Dendritic Growth of Yttrium Aluminium Garnet from an Oxide Melt in the System $SiO_2/Al_2O_3/Y_2O_3/CaO$. *CrystEngComm*. **14** (2012) 6904-6909. **DOI:** 10.1039/C2CE25961C

A. Keshavarzi, C. Rüssel. The Effect of TiO_2 and ZrO_2 Addition on the Crystallization of Ce^{3+} Doped Yttrium Aluminium Garnet from Glasses in the System $Y_2O_3/Al_2O_3/SiO_2/AlF_3$. *Mater. Chem. Phys.* **132** (2012) 278-283.

Y. Abdollahi, A Zakaria, M Abbasiyannejad, H. R. Fard Masoumi, M. Ghaffari Moghaddam, K. A. Matori, H. Jahangirian and **A. Keshavarzi**. Artificial neural network modeling of *p*-cresol photodegradation. Chem. Cent. J. **DOI**:10.1186/1752-153X-7-96

A.Keshavarzi, A. H. Abdullah, Z. Zainala. Low-Temperature Synthesis of ZnO by Wet Chemical Method. *International Journal of Material Science,* **4** (2009)163-168.

M.H. Entezari, **A. Keshavvarzi**. Phase Transfer Catalysis and Ultrasonic Waves II: Saponification of Vegetable oil. *Ultrason. Sonochem*. **8** (2001) 213-216.